Max-Planck Institut für Kolloid- und Grenzflächenforschung
Abteilung Kolloidchemie

Über neue Allotrope und Nanostrukturen von Karbonitriden

On new allotropes and nanostructures of carbon nitrides

Dissertation
zur Erlangung des akademischen Grades
"doctor rerum naturalium"
(Dr. rer. nat.)
in der Wissenschaftsdisziplin "Physikalische Chemie"

eingereicht an der
Mathematisch-Naturwissenschaftlichen Fakultät
der Universität Potsdam

von
Michael Janus Bojdys
aus Grudziądz, Polen

Potsdam, den 05 Januar 2009

Published online at the
Institutional Repository of the University of Potsdam:
URL http://opus.kobv.de/ubp/volltexte/2010/4123/
URN urn:nbn:de:kobv:517-opus-41236
http://nbn-resolving.org/urn:nbn:de:kobv:517-opus-41236

Contents

“I learned from my Arabian masters under the leading of reason, you, however, captivated by the appearance of authority, follow your halter. Since what else should authority be called than a halter?”

- Adelardus Bathensis, Bath, England, 1122

1 Introduction and motivation

The desire to transmute one form of a material into another, to find a new form of an element, an allotrope (Gr. *allos*, other, and *tropos*, manner) predates any modern concept of chemistry or science. Alchemists and wizards in the medieval Arabic Orient and later in Europe had a very optimistic approach to their experiments with transmutation, and their observations on the progress of science offered solid ground for their hopes: if grains of opaque sand could be transformed into clear glass, as the alchemists in Córdoba had shown, then it seemed reasonable to expect mercury could be transformed into silver or gold which appeared outwardly much more similar.[1]

In modern days, the quest for new allotropes became more prestigious beyond the prospect of mere gold. In 1996 the Nobel Prize in Chemistry was awarded to Robert F. Curl, Harold W. Kroto and Richard E. Smalley for their discovery of new forms of the element carbon – called fullerenes – in which atoms are arranged in closed shells in morphology not unlike footballs.[2-4] Formerly, six crystalline forms of the element carbon were known, namely two kinds of graphite, two kinds of diamond, chaoit and carbon(VI). The latter two were discovered in 1968 and 1972. The discovery of buckminsterfullerene (C_{60}, aka bucky ball) and its production in macroscopic quantities[5] has stimulated great interest in carbon in general leaving the field highly embattled and thoroughly ploughed with over 8000 publications a year since the early 90s dealing exclusively with carbon structures, components and compounds. The focus of the work at hand shifts to a far smaller subspace of carbon chemistry: the carbon nitrides.

The career of carbon nitrides in terms of our modern concept of science dates back to 1834 and a publication by Justus von Liebig entitled “About some nitrogen compounds”.[6] Carbon and nitrogen containing molecules, however, have been used – if not consciously known – before Bibilical times; think of enzymes, aromatic heterocycles, gaseous cyanogen[7] or even the infamous history of cyanide for that matter. Liebig described in his work several amorphous C/N materials which he obtained via thermolysis of mercury(II) thiocyanate and which he arbitrarily named melamine, melam, melem and melon with increasing temperature of formation (c.f. Figure 1).

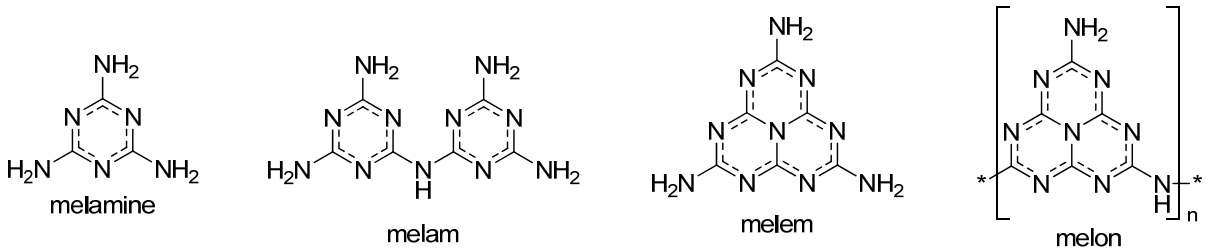

Figure 1. Carbon and nitrogen containing materials obtained from the thermolysis of mercury(II) thiocyanate as described by Liebig.[6]

It was exactly 150 years later that the interest in these compounds blossomed out with a force. In 1984 Sung allegedly predicted in an unpublished patent disclosure letter at the Diamond Technology Center of Norton Company that the carbon(IV) nitride, C_3N_4, "may be harder than diamond", the hardest material known. According to this disclosure, C_3N_4 may exist with two phases (α and β) that are isostructural to corresponding phases of Si_3N_4.[8] A similar theoretical study was published by Cohen et al. in 1989 – a collaborator of Sung in the early 80s and, as a matter of trivia, without Sung's consent. Although the terms "harder than diamond" stage no appearance in any of the publications of Cohen and his co-workers, and the only statement that was made was that these materials are likely to be extremely incompressible, it appears that many researchers had already been infected by the "*harder-than-diamond fever*" which led to a large number of experimental attempts to prepare the postulated phase, but also gave motivation for further theoretical studies on carbon(IV) nitrides. In many of these experiments the condensation pathway of cyanamide to dicyandiamide and later to melamine and all of the other C/N materials described by Liebig was seen as a good synthetic strategy. Naively, one would indeed assume that the formal deamination of melam or of melon as seen above must finally yield a compound free of hydrogen composed exclusively from carbon and nitrogen (c.f. Figure 2). Most of the published experiments, however, yielded non-stoichiometric, amorphous solids with hydrogen values and C/N ratios out of the range of the desired, and we shall see in chapter 3 and 4 to why these attempts failed.

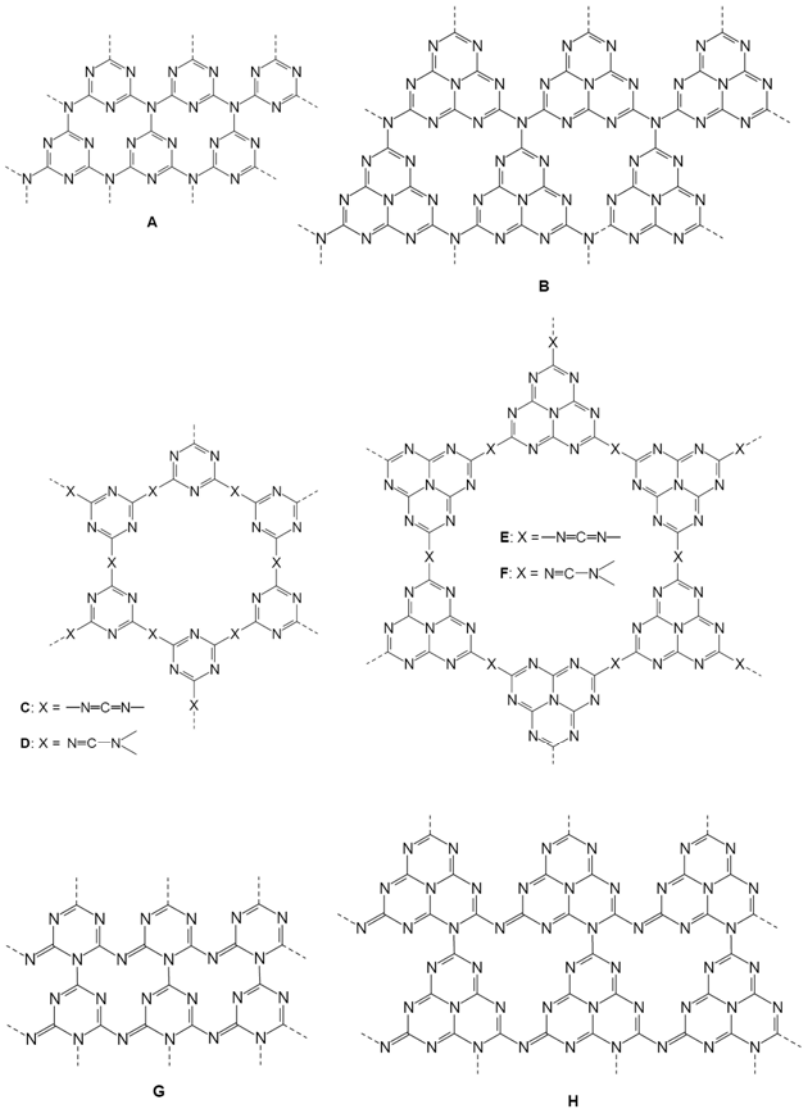

Figure 2. Simple examples for (graphitic) carbon(IV) nitride networks with relatively high symmetry, which are based on the s-triazin unit and the s-heptazine (tri-s-triazine) unit. Originally, it was found by theoretical studies that structure **A** should be the thermodynamically most stable C_3N_4-modification. Recently, it was shown that **B** is significantly more stable than **A**. Due to the lack of aromaticity within the heterocyclic rings the structures **G** and **H** are expected to be non-planar and destabilized.[9]

Figure 2, C though F, reveal an interesting twist in carbon nitride chemistry – the option to control the size of the cavity spanned by its constituents. According to Greiner, connecting s-triazine rings via carbodiimide groups provides a C_3N_4-structure with alternating C–N-atom arrangement (Figure 2, C).[10] These unsaturated C_3N_4-networks may form layered (graphitic) structures. Nevertheless, due to the flexibility and large size of cabities, a number of interpenetrating phases could exist. An isomeric cyanamide form was postulated by Kroll and Hoffmann (Figure 2 ,D).[11] In addition, Kroke *et al.* propsed heptazine

containing carbon(IV) nitrides which are analogous to the above mentioned carbodiimide-bridged triazine networks.[12, 13] These structures are not only gracious to the eye due to their interesting symmetries, they are also reminiscent of zeolities, a class of open-framework inorganic materials. Applications of open-framework materials are dominated by the aluminosilicate zeolites, which are noted for their stability and which find utility in catalysis, separations, and ion-exchange.[14] In chapter 6 we will elaborate on the concept of heptazine based frameworks and see whether carbon nitride chemistry holds a pathway to organic zeolites.

2 Theoretical background

2.1 X-ray diffraction

Structure determination by diffraction may be likened to forming an image of a diffraction grating, as shown below for two, three and five slit diffraction.

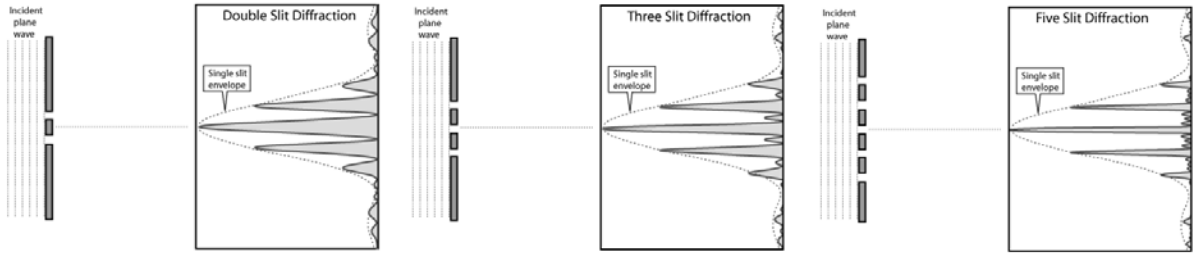

Figure 3. Diffraction of waves and expected images of the diffraction grating in a double, three and five slit experiment.

If we illuminate a crystal structure with radiation having a wavelength, λ, of the order of magnitude of the inter-atomic spacing, such as X-rays or neutrons, diffraction will occur in exactly the same manner, as the crystal consists of a group of atoms repeated in a regular fashion, just like the lines of a diffraction grating. This concept is analogous to light microscopy, however, the problem in this case is that, as yet, we have no lens for X-rays of this wavelength, and so we cannot form an image, although the diffracted beams can be detected and their intensity measured.

However, the ultimate goal of any X-ray diffraction experiment cannot be the sheer measurement of a set of diffracted beam intensities, but the distribution of electron density in real space and hence the structure which causes that diffraction. The electron density, $\rho(\boldsymbol{r})$, is related to the diffracted amplitude, $F(\boldsymbol{S})$, by the inverse Fourier transform relationship:

$$\rho(\boldsymbol{r}) = FT^{-1}\left[\left|F(\boldsymbol{S})\right|\exp \boldsymbol{i}\Phi(\boldsymbol{S})\right] = \int \left|F(\boldsymbol{S})\right|\exp \boldsymbol{i}\Phi(\boldsymbol{S})\exp\left(-2\pi \boldsymbol{i}\boldsymbol{r}\cdot\boldsymbol{S}\right)dV_S$$

In a diffraction experiment, we do not normally measure the diffracted amplitude, $F(\boldsymbol{S})$, but instead we record the diffracted intensity, $I(\boldsymbol{S}) = |F(\boldsymbol{S})|^2$. The amplitude, $F(\boldsymbol{S})$, however, is a vector and should more correctly be written in modulus-argument, e.g. $F(\boldsymbol{S}) = |F(\boldsymbol{S})| \exp \boldsymbol{i}\Phi(\boldsymbol{S})$, where $|F(\boldsymbol{S})|$ is the length of the vector on the Argand diagram and $\Phi(\boldsymbol{S})$ is the phase angle this vector makes with the horizontal (real) axis within the structure. Now, taking the modulus of the amplitude, we lose the angular information, as we find that $|F(-\boldsymbol{S})| = |F(\boldsymbol{S})|$ and $\Phi(-\boldsymbol{S}) = -\Phi(\boldsymbol{S})$. This is commonly known as the "phase problem" which, at first sight, might have no possible solution if we cannot measure the $\Phi(\boldsymbol{S})$ terms. However, we can relate the diffracted intensity and the electron density via a mathematical construct called the **Patterson Function**, viz.

$$P(\boldsymbol{r}) = FT^{-1}\left[|F(\boldsymbol{S})|^2\right] = FT^{-1}[F(\boldsymbol{S})] * FT^{-1}[Complex\ Conj.] = \rho(\boldsymbol{r}) * \rho(-\boldsymbol{r})$$

This function always represents the first step in structure determination. In many cases we use it to find the positions of some of the atoms; from these atomic positions we can calculate approximate values of the phases, $\Phi(\boldsymbol{S})$, and then use this information to get an even better approximation to the true structure, and so on. In order to operate such a cumbersome equation, however, we need to be able to relate real space coordinates, $\boldsymbol{r}$, to the scattering vector, $\boldsymbol{S}$, in reciprocal space.

2.1.1 Laue, Ewald, Miller and Bragg relationships

For diffraction to occur in a perfect crystal, the value of the scattering vector, $\boldsymbol{S}$, must obey the condition:

$$\boldsymbol{S} = (1/\lambda)(\boldsymbol{s}_0 - \boldsymbol{s}) = h\boldsymbol{a}^* + k\boldsymbol{b}^* + l\boldsymbol{c}^*$$

If we form scalar products of both sides with $\boldsymbol{a}$, $\boldsymbol{b}$ and $\boldsymbol{c}$ in turn, we produce the three **Laue equations** viz.

$$(1/\lambda)(\boldsymbol{s}_0 - \boldsymbol{s}) \cdot \boldsymbol{a} = h$$

$$(1/\lambda)(\boldsymbol{s}_0 - \boldsymbol{s}) \cdot \boldsymbol{b} = k$$

$$(1/\lambda)(\boldsymbol{s}_0 - \boldsymbol{s}) \cdot \boldsymbol{c} = l$$

where h, k and l are restricted to integral values. In reciprocal space, $\boldsymbol{s}_0$ is a unit vector parallel to the incident beam, while $\boldsymbol{s}$ is a unit vector parallel to the diffracted beam. This implies that the end of the vector $\boldsymbol{S}$ lies on the surface of a sphere, with the incident beam forming a diameter of this sphere and the origin being at a point on its surface. This sphere is known as the **Ewald sphere**. Furthermore, the scattering vector $\boldsymbol{S}$ is perpendicular to the plane which contains the three vectors $(|\boldsymbol{a}|/h - |\boldsymbol{b}|/k)$, $(|\boldsymbol{a}|/h - |\boldsymbol{c}|/l)$ and $(|\boldsymbol{b}|/k - |\boldsymbol{c}|/l)$. Both finds are shown below.

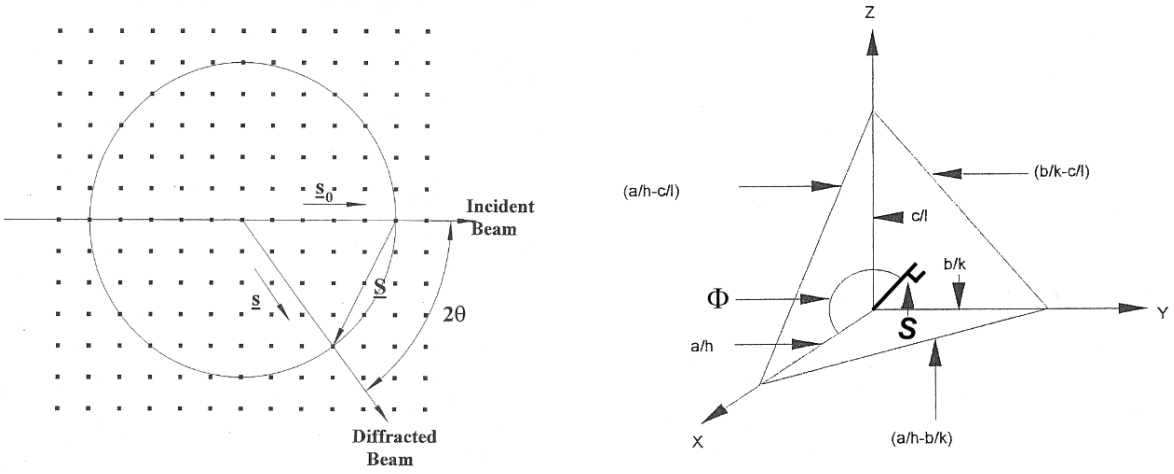

Figure 4. Expression of the scattering vector $\boldsymbol{S}$ in terms of the Ewald sphere (left) and in vector notation with respect to a plane with the Miller indices h, k and l (right).

The intercepts of this plane on the x, y and z axes are then given by $|\boldsymbol{a}|/h$, $|\boldsymbol{b}|/k$ and $|\boldsymbol{c}|/l$, where h, k and l are the **Miller indices** of the plane. The spacing of this plane, designated $d_{(hkl)}$ is given by the projection of the vectors $|\boldsymbol{a}|/h$, $|\boldsymbol{b}|/k$ and $|\boldsymbol{c}|/l$ on $\boldsymbol{S}$, e.g. $(|\boldsymbol{a}|/h)\cos\Phi$.

In vector notation, therefore, we can say that:

$$d_{(hkl)} = (\boldsymbol{a}/h)(\boldsymbol{S}/|\boldsymbol{S}|)$$

where $(\boldsymbol{S}/|\boldsymbol{S}|)$ is a unit vector parallel to $\boldsymbol{S}$. However, from the first of the Laue equations and from the definition of $\boldsymbol{S}$ we have that $\boldsymbol{S} \cdot \boldsymbol{a} = h$ and $|\boldsymbol{S}| = 2\sin\theta/\lambda$, hence:

$$\lambda = 2d_{(hkl)} \sin\theta,$$

which is **Bragg's law**.

2.2 Principles of powder diffraction

In powder diffraction methods a polycrystalline specimen is used rather than a single crystal. The number of crystallites irradiated by the incident beam at any instant is extremely large, and ideally, every possible orientation is present. Consequently the reciprocal lattice becomes a set of concentric spheres, centred on the origin of reciprocal space, as shown below for a 4 Å cubic I-lattice:

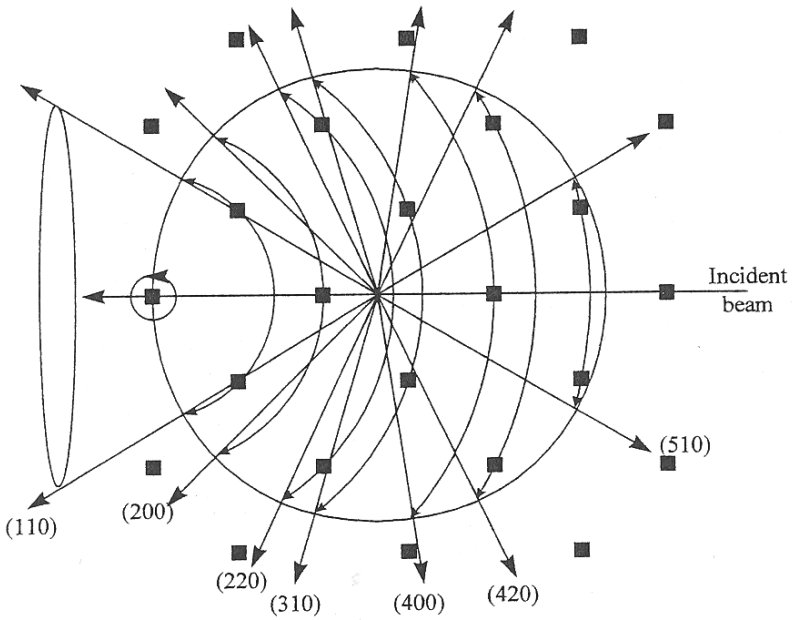

Figure 5. Construction of reciprocal space for a polycrystalline sample as a set of concentric spheres centred on the origin.

As all possible orientations are present, there is no need to rotate the specimen, and the reciprocal lattice spheres will intersect the Ewald sphere in a circle, giving rise to a cone of diffracted radiation, as shown above for (110) diffraction. The powder diffraction pattern can then be recorded simply by measuring the intensities of the diffraction "cones" with a moving detector, in what is called the Debye-Scherrer arrangement, as shown below.

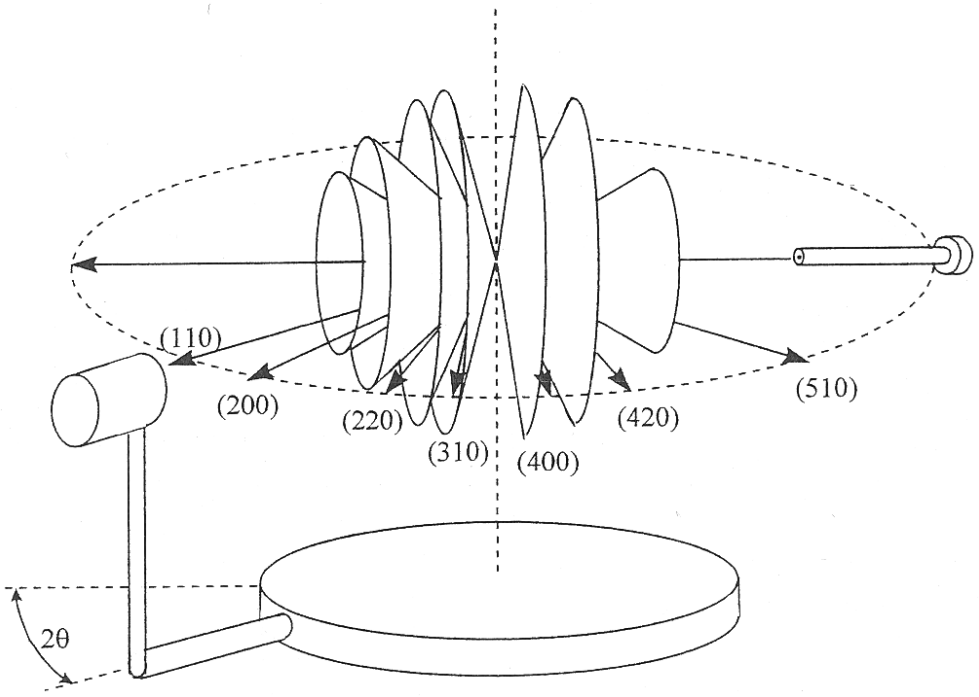

Figure 6. Concept of a powder diffraction experiment in Debye-Scherrer geometry. The powder diffraction pattern is recorded by measuring the intensities of the diffraction "cones" with a moving detector.

The result is a plot of intensity as a function of the scattering angle 2θ, as shown below. The intensities of the peaks obtained are easily measured and correspond to the intensity of diffraction within each cone.

2.3 Structure refinement using powder diffraction data

2.3.1 The method of least squares

Least squares lies at heart of most refinement techniques including Rietveld refinement. The method is used to model numerical data obtained from observations by adjusting the parameters of a model so as to get an optimal fit of the data. The method was first described by Carl Friedrich Gauss around 1794.

Suppose that we have a data series that we wish to fit to the linear relationship $y = m \cdot x + c$. We need therefore to calculate values of m and c which give a best fit to the observed data. Let these be m_0 and c_0. Let us assume also that the errors in the y-values are known to be much greater than those in the x-values. If the measured values of any y-value is y_i the discrepancy between this and its calculated values is:

$$y_i - y = y_i - m_0 \cdot x_i - c_0 ,$$

Equation 1

where x_i is the corresponding x-value. There will be an equation of this form for each measurement we make.

The best fit (i.e. the best values of m_0 and c_0 to the experimental data) is then obtained if we minimise the sum of the squared residuals between the observed value and the value given by the model. The summation may be written as:

$$\begin{aligned} R &= \sum_i (y_i - y)^2 = \sum_i (y_i - m_0 \cdot x_i - c_0)^2 \\ &= \sum_i (y_i)^2 - 2m_0 \sum_i x_i y_i - 2c_0 \sum_i y_i + {m_0}^2 \sum_i (x_i)^2 + 2m_0 c_0 \sum_i x_i + N(c_0)^2 , \end{aligned}$$

Equation 2

where there are *N* terms in the summation This expression will be a minimum when the partial derivatives of R with respect to m_0 and c_0 are zero, namely:

$$\partial R / \partial m_0 = -\sum_i x_i y_i + m_0 \sum_i (x_i)^2 + c_0 \sum_i x_i = 0$$
$$\partial R / \partial c_0 = -\sum_i y_i + m_0 \sum_i x_i + N c_0 = 0$$

Equation 3

Solving these for m_0 and c_0 then yields:

$$m_0 = \frac{N\sum_i x_i y_i - \sum_i x_i \sum_i y_i}{N\sum_i x_i^{\,2} - \left(\sum_i x_i\right)^2} \text{ and } c_0 = \sum_i y_i - m_0 \sum_i x_i$$

Equation 4

2.3.2 Application of least squares refinement to structures

In a structure refinement the quantities equivalent to the y_i-values above are the $|F(hkl)_{obs}|$ values. These are undoubtedly subject to large random errors of measurement, particularly for the weaker beams. The equivalent quantities to the x_i-values are the $|F(hkl)_{calc}|$ values. These in turn depend on the atomic scattering factors, temperature factors, site occupancy factors and the atomic coordinates x_n, y_n and z_n. For simplicity, let us initially omit any considerations of temperature and site occupancy factors, and assume that the scattering factors are known exactly. Hence the structure factor $F(hkl)$ will depend solely on the contents of the unit cell, given by:

$$F(hkl)_{calc} = \sum_n f_n(\boldsymbol{S}) \times \exp 2\pi \boldsymbol{i}(hx_n + ky_n + lz_n)$$

Equation 5

It is assumed that the peaks have been indexed correctly and h, k and l values are known precisely. What we therefore need is a series of coordinates x_n, y_n and z_n which

minimise the differences between $|F(hkl)_{obs}|$ and $|F(hkl)_{calc}|$. The quantity which we have to minimise is therefore:

$$R = \sum_{hkl} w_{hkl} \left\{ |F(hkl)_{obs}| - |F(hkl)_{calc}| \right\}^2 ,$$

Equation 6

where w_{hkl} is a weighting factor which takes account of the accuracy of measurement of the quantity $|F(hkl)_{obs}|$.

To simplify the maths, let us consider only a structure in one dimension (i.e. k and l are zero), which furthermore has a centre of symmetry (i.e. "$\exp \boldsymbol{i}$" replaced by "$\cos$", taking the summation over only one half of the atoms). The above equation reduces to:

$$\sum_h w_h \left\{ F(h)_{obs} - F(h)_{calc} \right\}^2 = \sum_h w_h \left\{ F(h)_{obs} - 2\sum_n f_n(\boldsymbol{S}) \times \cos 2\pi (hx_n) \right\}^2$$

Equation 7

The problem now is that the equations are non-linear, but we can overcome this difficulty in the following way. Suppose we write x_n as $x_n^0 + \delta x_n$, where x_n^0 is the value of x_n in the "trial" structure which we wish to refine and δx_n is the atom shift necessary to effect this refinement. If δx_n is small, we can expand this expression as follows:

$$\begin{aligned} \sum_h w_h \left\{ F(h)_{obs} - F(h)_{calc} \right\}^2 &= \sum_h w_h \left\{ F(h)_{obs} - 2\sum_n f_n(\boldsymbol{S}) \times \cos\left[2\pi h x_n^0\right] \cdot \left(1 - \frac{\left[2\pi h \delta x_n\right]^2}{2} \right) \right\}^2 \\ &= \sum_h w_h \left\{ F(h)_{obs} - F'(h)_{calc} + 2\sum_n f_n(\boldsymbol{S}) \times \cos\left[2\pi h x_n^0\right] \Delta x_n \right\}^2 , \end{aligned}$$

Equation 8

where $F'(h)_{calc} = 2\sum_n f_n(\boldsymbol{S}) \times \cos\left[2\pi h x_n^0\right]$ and $\Delta x_n = \left[2\pi \delta x_n\right]^2 / 2$. Now we have obtained an equation which is linear with respect to Δx_n, where $F'(h)_{calc}$ can be evaluated from the x_n^0 values in the trial structure, and $F(h)_{obs}$ is measured. In other words we have obtained an

equation which can be readily differentiated with respect to each of the Δx_n variables in turn. This will yield:

$$\partial R / \partial(\Delta x_{n1}) = \sum_h \left\{ A(h) - B(h)_{n1} + 4 \sum_{n(n \neq n1)} B(h)_n B(h)_{n1} \Delta x_n + 8\left(B(h)_{n1}\right)^2 \Delta x_{n1} \right\}$$

Equation 9

If there are N atoms, the result will be a $N \times N$ matrix of linear equations, which can be solved quite readily for the Δx_n values. Once these have been obtained, the actual atomic shifts δx_n can be determined from the original definition of Δx_n.

Now let us try to appreciate the important difference from the original least squares, in that we have to use the x_n^0 values (which are known to be incorrect) in order to calculate the required δx_n terms, i.e. we have to guess the positions of individual atoms *a priori*. When these shifts are applied, they in turn will give new x_n^0 values and the whole process can be repeated. Continuous reiteration may be carried out until the δx_n values produced are no longer significant. Note however, that an educated *a priori* guess is required. Suppose the initial guess, x_n^0, produces a large necessary shift in atom position, δx_n, then the expansion used to produce Equation 8 would not hold and the refinement would produce no meaningful results.

Luckily this simple principle as demonstrated here on paper for a one dimensional, centrosymmetric array of “atoms on a string” has the advantage that it can be made completely automatic including site occupancies and temperature factors in the refinement process.

2.4 Inelastic scattering of electrons and compositional analysis

Because electrons interact strongly with matter, many different processes occur at the specimen, as shown in the accompanying diagram. In the following, we will focus on only a few selected techniques, which were used to give chemical and/or structural information about the specimen, namely:

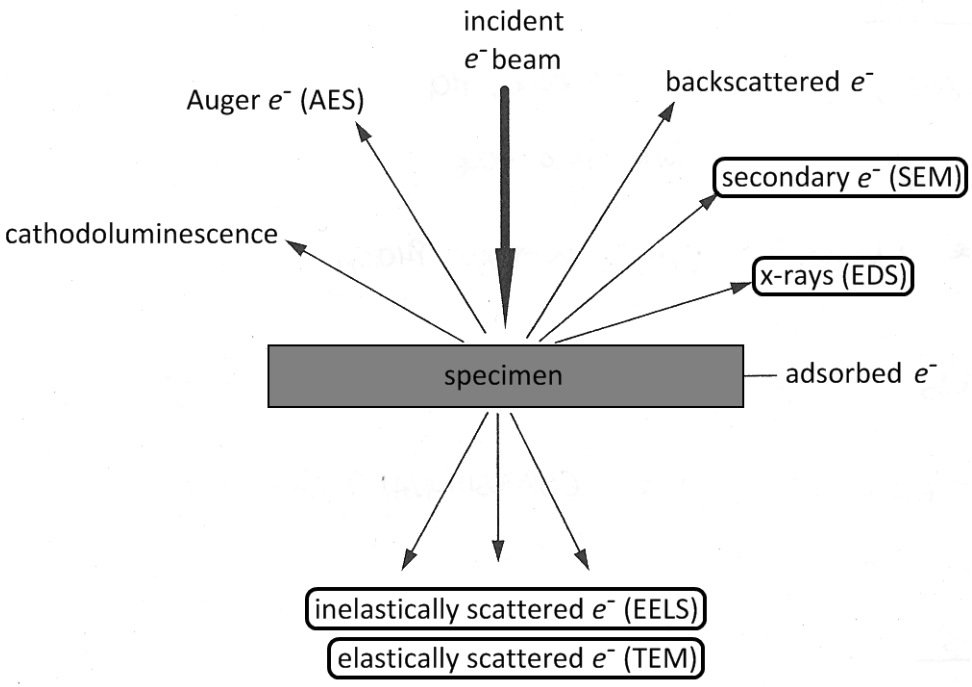

Figure 7. Schematic overview of electron-specimen interactions used in compositional and morphological analysis.

Secondary electrons are backscattered electrons which have undergone significant energy loss in the specimen. As their energy is much lower than the incident beam, they can only escape from the specimen at surfaces, edges or other discontinuities. Consequently their intensity will be higher at these regions, and they can be used to show the topography of the specimen. This is normally done as shown below, by focusing the electron beam into a very fine probe and scanning it over the specimen. The secondary electron signal is then used as the source for a TV input which is scanned at the same rate, and an image of the specimen surface generated. This is the principal of **scanning electron microscopy (SEM)**. Very high magnification (> 100,000 X) is possible, and unlike the case of optical microscopy, the depth of the field is large because the divergence of the electron beam is very small.

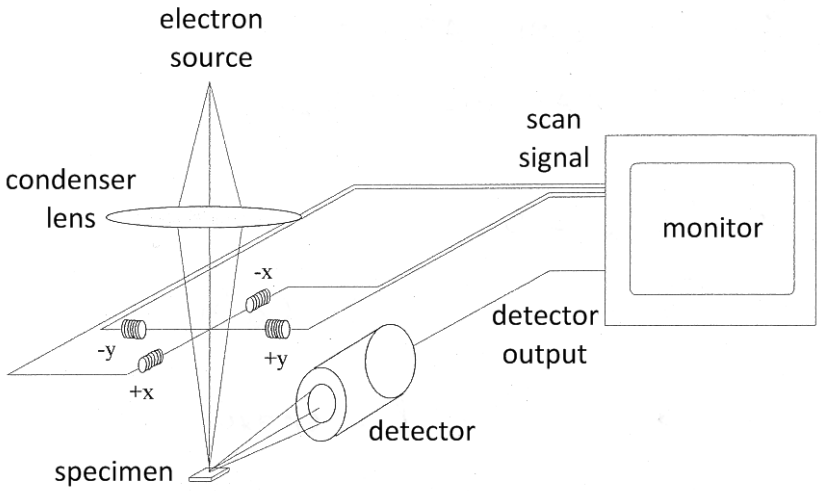

Figure 8. Schematic illustration of the principles of scanning electron microscopy.

Characteristic x-rays are generated when the incident beam ionises an atom, creating an electron vacancy in an inner level (e.g. the K level). This vacancy is filled immediately by another electron from a higher energy level or in a level close to it (e.g. $L_{1,2,3}$), and the atom loses its excess energy by emitting an x-ray photon. According to energy conservation laws this quantum of emitted radiation will have a discrete energy corresponding to the difference in energy between the K and the L level, namely $h\nu = E_K - E_L$. The vacancy in the K shell may also be filled by an electron directly from the M shell, resulting in a quantum of radiation with a higher energy, $h\nu = E_K - E_M$. The radiation corresponding to the transition between the L and K levels is designated K_α radiation, and that corresponding to the M to K transition is designated K_β. The vacancy in the L shell will also be reoccupied by an electron from a shell with a higher energy level, such as the M shell, giving a spectrum of radiation L_α, L_α, etc. A series of characteristic x-rays are therefore emitted from the solid with the energies being dependent on the atomic numbers of the elements emitting it, so the x-ray emission spectrum can be used to give compositional information about the specimen. This process is analogous to the generation of Auger electrons. However, one important advantage, from the analytical point of view, is that x-ray photons are not so readily absorbed by the specimen as the Auger electrons, and therefore may be used to give the composition of the bulk specimen. X-ray emission of this type is extremely important in solid-state chemistry, and is the principle behind **energy**

dispersive x-ray spectroscopy (EDS). The illustration below shows an actual EDS spectrum of strontium. Note the shoulder in the L line, which is the consequence of five sub shells in the M level and three in the L level. Similarly, because of the three sub-levels in the L level both the K_α and K_β lines are broadened. The energy difference between two shells and between sub-shells in the same shell increases with the atomic number, and consequently more emission lines are observed in the EDS spectrum.

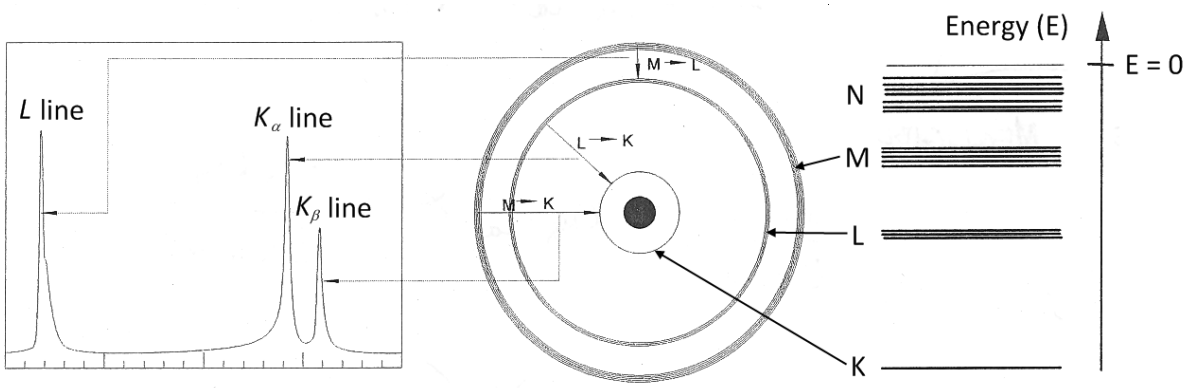

Figure 9. Transitions between energy shells corresponding to the K_α, K_β and L x-ray emission lines of a strontium atom.

Inelastically scattered electrons are those electrons which are transmitted through the specimen after having suffered an energy loss. This loss in energy can arise from general interactions with valence electrons within the specimen, or from core-shell excitations producing Auger electrons and x-ray photons. The energy distribution of all electrons passing through the specimen may be studied using **electron energy loss spectroscopy (EELS)**, which again provides compositional information about the specimen. Along with EDS, EELS is one of the most important analytical tools available to the synthetic solid-state chemist. EELS is also a sensitive probe of the valence state and local environment of the atoms within the specimen, and the inelastically scattered electrons may also be used to form an image.

2.5 Electron diffraction and imaging

Because electrons have properties of waves, they can be diffracted just like X-rays. The wavelength of an accelerated electron is given by the De Broglie equation for the relativistic case:

$$\lambda = \frac{h}{mv} \Rightarrow \lambda = \frac{h}{\sqrt{2m_e eV\left(1+\frac{eV}{2m_e c^2}\right)}},$$

hence, when the accelerating voltage is $V = 200\,\mathrm{kV}$, the wavelength will be - $\lambda = 0.0251\,\text{Å}$. This exceedingly small wavelength gives rise to a much larger Ewald sphere, with a radius $1/\lambda$ of some $40\,\text{Å}^{-1}$ for $V = 200\,\mathrm{kV}$ .This means that many reciprocal lattice points will intersect the sphere at any one time, and consequently many diffracted beams will be obtained simultaneously. This makes it possible to record an undistorted picture of reciprocal space. Both transmitted and diffracted beams are brought to a focus by the objective lens in the back focal plane. Below this plane, two modes of operation (imaging and diffraction) are possible, as shown below.

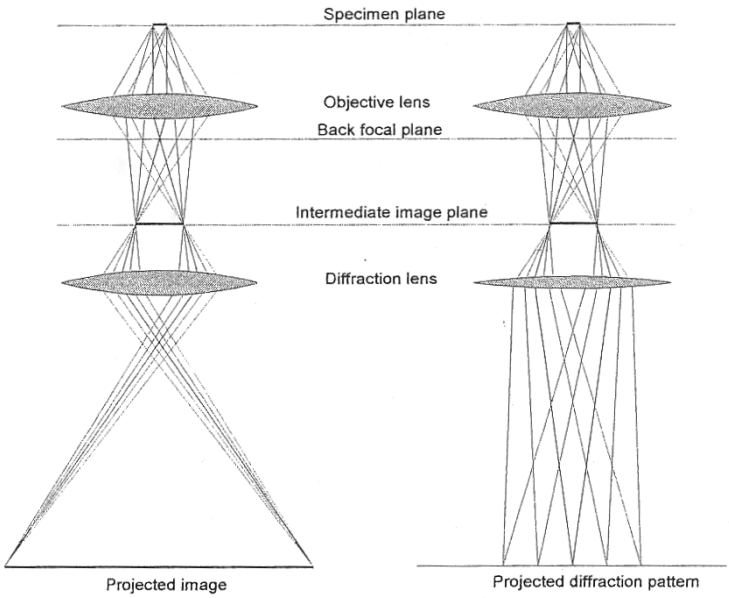

Figure 10. Schematic illustration of an electron microscope in imaging (left) and diffraction mode (right).

In the image mode, the lower lens further magnifies the intermediate image until it is finally projected onto the fluorescent screen. When a weaker lens is used below the intermediate image plane, the electron wavefront in the objective back focal plane may be projected onto the screen and consequently the diffraction pattern may be recorded. This is called the diffraction mode of operation.

One of the advantages of electron microscopy is that a very small area of the solid can be examined, and consequently it is possible to record the diffraction pattern from a very small area. The simplest way to do this would be to insert an aperture at the specimen to restrict the area actually illuminated by the beam, but a better solution is to insert this aperture into the intermediate image plane, where the image of the specimen is magnified. This removes the need for a very small aperture, yet still enables us to collect beams diffracted only from a small area in the specimen. This operation mode is called **selected area electron diffraction (SAED)**.

2.6 Some thoughts on the interaction of x-rays and electrons with light solid-state materials

Since we originally set out to examine solid state materials composed exclusively of light atoms, it might be worth pondering the particularities we are bound to encounter using the analytical techniques outlined above.

The atomic number (Z) effect arises because the attenuation of the electron beam depends on the specimen composition. In general, lighter atoms (i.e. atoms of lower atomic number, Z), will attenuate the electron beam less rapidly, and consequently we expect that the electron beam will sample a large volume of the specimen.

The absorption (A) effect arises because the x-rays emitted by atoms in the specimen also suffer absorption as they pass through the specimen on their way to the detector. The magnitude of this absorption depends on both the energy of the x-rays and on the average

atomic number of the specimen. We might expect no significant contribution from the average atomic number of the specimen to the absorption of the x-rays. However, the energies of K x-rays emitted from light atoms are comparatively low and hence will have a harder time escaping the bulk of the sample.

Special care should be employed regarding the quality of observations of effects which rely on electron shells transitions. We noted previously that the energy differences between the electron shells of an irradiated atom decrease with Z. As a consequence, the resolution of signals both in EELS and EDS will invariably suffer. In the first case, low energetic degeneracy of e.g. the $L_{1,2,3}$ levels will result in only minor interference of the electron beam with the specimen, and, as a consequence, in peak overlap and broadening. In the latter case, K x-rays emitted from most light atoms have comparably low energies (e.g. carbon K, nitrogen K and oxygen K all feature between 0.2 and $0.5\,\mathrm{keV}$) resulting in peak overlap. This makes light solid-state materials more suitable for bulk measurements via EELS and TEM, while EDS remains an option for surface sensitive sampling at best.

3 Graphitic carbon nitride

3.1 Introduction to carbon nitride materials

Terminologically all binary compounds of carbon and nitrogen can be considered as carbon nitrides. Molecular carbon and nitrogen containing compounds – analogous to carbon oxides like CO_2, CO and other C_xO_y species – are known to every chemist. First attempts to prepare solid state carbon nitride materials were known to literature since the early 1830s,[6, 15] and in 1922, Franklin described the formation of an amorphous carbon nitride material by thermolysis of mercury(II) thiocyanate,[16] more commonly known from its use in pyrotechnics as the Pharaoh's snakes. The resulting materials however have eluded rigorous analysis and characterisation for a long time mostly due to their insolubility in water and organic solvents. Interest in carbon nitrides – in particular its saturated, sp^3-hybridised, crystalline allotropes – was sparked in the 1980s by the work of Sung and Sung[8] and by the theoretician Cohen[17] who speculated that the bulk modulus for a "tetrahedral compound ... formed between C and N" would be "significantly larger than for diamond". Although the shear modulus, G_0, rather than the bulk modulus, B_0, is a good indicator for hardness,[18] the prospect of outstanding material properties, above all, extreme hardness and high thermal stability has lead to a large number of publications on carbon nitrides since the first theoretical paper was published, some of them claiming the successful formation of several of the initially predicted carbon nitride phases by chemical and physical vapour deposition techniques (CVD and PVD).[19, 20] Reoccurring criticism from Fang,[21] DeVries,[22] Matsumoto[20] and Malkow[23] however gives reason to believe that, to date, no satisfactory evidence has been presented that a crystalline solid of the proposed kind has been synthesised, moreover that in some cases non-stoichiometric, amorphous solids were the dominant product.

Due to the difficulties encountered in the synthesis of single-phase sp^3-hybridized carbon nitride phases on preparative scale by physical methods, synthetic approaches shifted towards a chemical route in the 1990s. A large number of experiments was devised which all utilise the condensation of suitable carbon and nitrogen containing, molecular

precursors to form graphitic carbon nitride materials (*g*-C_3N_4), which are regarded to be the most stable allotrope at ambient conditions.[12] Several C/N/H/S-containing compounds were identified, which were considered promising precursors for the chemical and bulk routes towards pure CN_x-phases - among these *s*-triazines (in particular their chlorides and fluorides),[24-26] *s*-heptazines[6, 27, 28] and thiocyanates.[16, 29] Note though, that bulk synthesis routes based on these precursors did not yield the desired, highly condensed, crystalline CN_x-phases either, but rather incompletely condensed materials. Elemental microanalyses of those substances show hydrogen contents of up to 2 wt % resembling a stoichiometry closer to melon (poly[(8-amino-1,3,4,6,7,8,9,9b-heptaazaphenalen-2,5-diyl)imine]) (1.5 wt % hydrogen).[30] Representatives for many attempts to synthesise C_3N_4 structures via high-pressure, high-temperature routes are the slow thermal decomposition[31] or the detonative synthesis[32] using tri-azido-*s*-triazine, $C_3N_3(N_3)_3$, which yielded a series of amorphous C/N/H/O-containing compounds, in the prior case carbon nanotubes, and nanoparticles in the latter. It should be noted that the field of HP-HT synthesis was advanced by Riedel, Kroke, McMillan *et al* very recently showing that conversion of dicyandiamide under HP-HT conditions indeed yields a crystalline carbon nitride imide phase, $C_2N_2(NH)$.[33] A more complete discussion of the history of both chemical and physical approaches towards a multitude of CN_x-phases can be found elsewhere.[12, 34]

The observant reader will have noticed that all of a sudden the topic of carbon nitride materials revolves around one particular allotrope namely graphitic carbon nitride and the synthetic challenges thereof. So why busy ourselves with this particular type of material which has led quite a few scientists astray? Well, there is hope that in analogy to the graphite/diamond system, a graphitic form of (sp^2 hybridised) carbon(IV) nitride (*g*-C_3N_4) could be transformed to the sp^3 hybridised form via high-pressure techniques.[35] Apart from its role as a potential precursor for its fabled 3D-allotrope, *g*-C_3N_4 is a thermally stable catalyst,[36-38] and is discussed as a membrane material or for gas storage.[39] Even more interestingly Wang, Domen and Antonietti demonstrated recently, that carbon nitride in its polymeric, conjugated form acts as semiconducting catalyst in the production of hydrogen from water under irradiation with visible light.[40] Thus, the question of “why” is covered sufficiently. The question of “how” is addressed in the following section.

3.2 Basic considerations on the synthetic pathway to graphitic carbon nitride

Kroke et al. proposed that *g*-C_3N_4 consists of sheets of highly ordered tri-*s*-triazine moieties connected through planarised, tertiary amino groups as depicted in Figure 11. The tri-*s*-triazine based structure was postulated on the basis of DFT calculations to be more stable at ambient conditions.[13] A very elaborate description of the underlying thermal self-condensation mechanism of cyanamide leading to these structures was previously published by Schnick and co-workers.[41] We will come back to this important study in the final proposal of a reaction mechanism (c.f. Figure 16), for now it suffices to know that it is based on the molecular reaction of cyanamide and its successive condensation products, which is driven both by deamination and the formation of aromatic units (Figure 11).

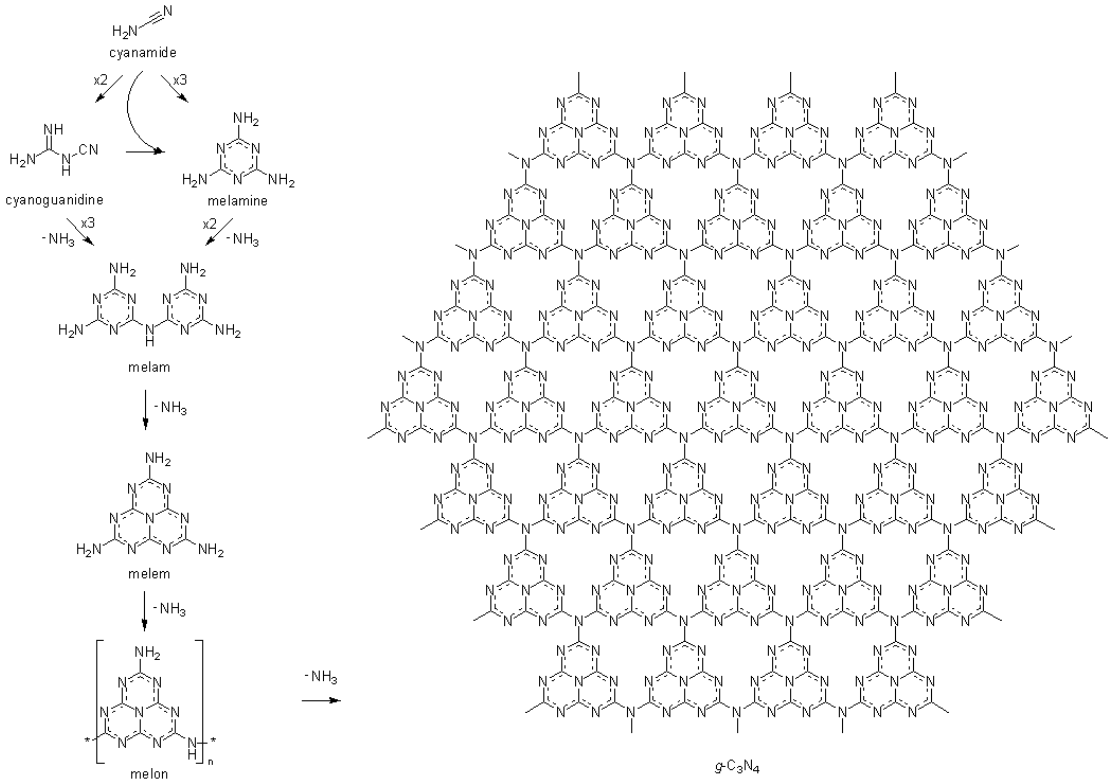

Figure 11. Condensation reactions of cyanamide yielding discrete oligomers, polymers and extended networks.

The reaction shown above was discussed in early literature as a possible formation mechanism for C_3N_4 analogous to the (formal) dehydration of tetrahydroxymethane via

carbonic acid to carbon dioxide. The idea then is that continued heating could very well lead us to the desired product.

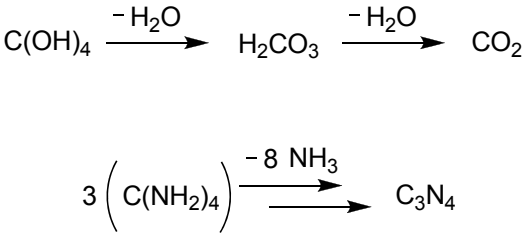

Figure 12. Formation mechanism of C_3N_4 analogous to the (formal) dehydration of tetrahydroxymethane via carbonic acid to carbon dioxide

Unfortunately, deamination is not the only thermally induced fragmentation process. A study employing thermogravimetric analysis (TGA) coupled with mass spectrometry (MS) reveals the evolution of three major gas phase products, namely ammonia (starting at 450 °C), a CNH species (starting at 480 °C) and a C_2N_2 species (starting at 540 °C) before the material decomposes at 680 to 700 °C, as seen below in Figure 13.

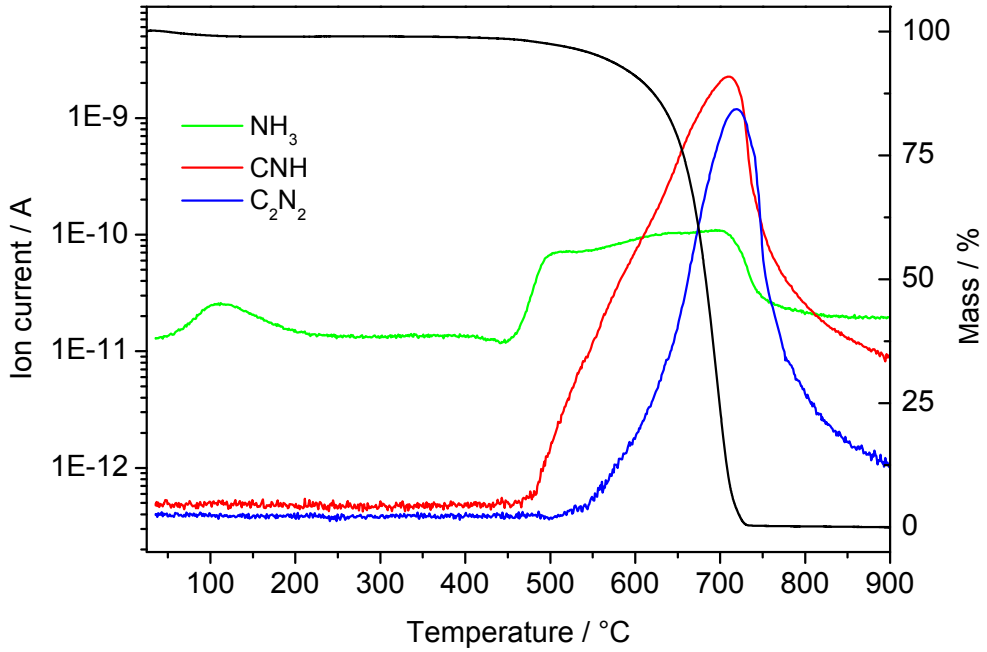

Figure 13. TGA/MS plot of the thermal condensation and decomposition products of melem (2,5,8-triamino-tri-s-triazine).

Assuming we start the condensation process with a monomer of the composition $C_nN_{2n}H_{2n}$ (C/N ratio is 0.5) it very quickly becomes obvious that a composition of $C_{3n}N_{4n}$ (C/N ratio is 0.75) cannot be achieved if carbon is eliminated along the way. Now, we observe a temperature window of 30 to 90 °C between the evolution of ammonia and the carbonaceous fragments, in which – naively assuming – the deamination reaction could be driven to completion. To test this hypothesis, the condensation mixture was arrested within the temperature window (at 530 °C) under inert atmosphere and subsequently examined (c.f. Figure 14).

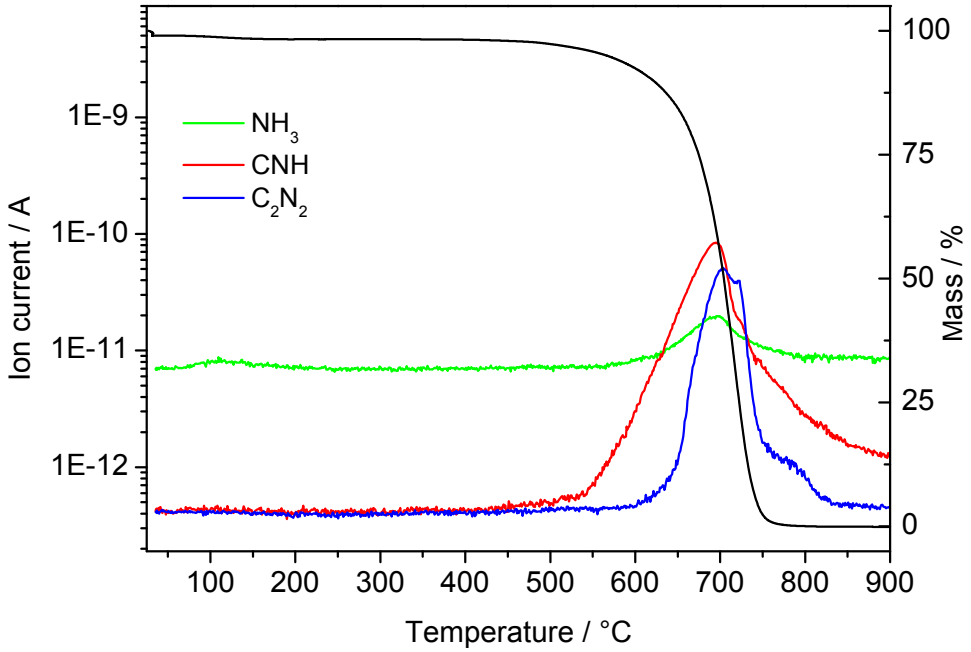

Figure 14. TGA/MS plot of the thermal condensation and decomposition products of carbon nitride as obtained from the bulk condensation reaction (terminated at 530 °C).

Although the overall evolution of ammonia could be reduced, there is a significant, residual amount of ammonia, which is not liberated until the carbon nitride material fully decomposes between 680 and 700 °C. This is bad news, for it means that bulk condensation along the lines suggested in Figure 11 will always yield a product of the composition $C_xN_yH_z$ with inherent primary, terminal ammonia groups and/or bridging secondary ammonia groups. Is this a dead-end on the way to a C_3N_4 material?

Incomplete condensation or polymerisation in the bulk - as applying for this type of reaction - is widely acknowledged as a predominantly kinetic problem. Schnick et al. demonstrated that the bulk reaction does not proceed significantly past the polymeric form (melon).[27] In a very elaborate study employing electron diffraction and solid-state NMR spectroscopy they have shown that the bulk condensation reaction of melem terminates at layers comprised of infinite chains of "melem monomers". These chains are condensed via N-H bridges forming a closely packed two-dimensional array.[42] Now, this principle problem is inherent to all of solid state chemistry. If we want to achieve perfect condensation in a kinetically inhibited system, we must require perfect pre-alignment. If the direction of growth and, hence, the alignment of our large, oligomeric precursors (melon) is statistically controlled, the number of terminal reactive groups with the right orientation to one another other will also be statistical, and the resulting product is expected to be littered with unreacted termini. This problem of oligomer-mobility can be overcome using an appropriate solvent. The nature of the polycondensation reaction of *s*-heptazine derivatives, namely the thermally induced reaction at temperatures of 400°C and above, however discards all standard solvents. Kanatzidis and co-workers have previously pointed out the limited choice of appropriate media for synthetic applications at intermediate temperatures (i.e., 150-350 °C) and successfully applied alkali-metal polysulfide melts in the synthesis of low-dimensional ternary chalcogenides.[43] The eutectic mixture of lithium chloride and potassium chloride (45:55 wt %, T_m: 352 °C)[44] has been known for some time as a medium for electrochemical processes, in particular in high-temperature galvanic cells[45] and more recently as a solvent for salts of lanthanides and actinides.[46] Sundermeyer *et al* showed already in the 1960s that known organic chemistry can be performed in molten salts.[47, 48] Among the successfully synthesised compounds were carbonyl and fluorocarbonyl pseudohalogenides[49] and cyanides, cyanates and thiocyanates of both silicon and carbon.[50] In this context Sundermeyer explicitly points out the good solvating properties of the eutectic mixture of LiCl and KCl with respect to nitrides, carbides, cyanides, cyanates and thiocyanates.

For our means the LiCl-KCl eutectic was identified as a good solvent due to its high-temperature stability, non-corrosive properties and a melting point below the polycondensation point of *s*-heptazine. Furthermore, the good solvation of the small

molecular precursors and subsequent aggregates of higher molecular weight facilitates the condensation of the carbon nitride network. Following up the leads from other groups that crystalline C/N-phases are indeed obtainable, the following section is intended to provide the proof that the synthesis of an extended, highly crystalline, graphitic carbon nitride is possible.

3.3 Formulation of a condensation pathway

Before we embark on the exciting path of classic organic synthesis in such an unconventional solvent as hot salt melt, let us try to fill out the blanks in the condensation pathway of C_3N_4. Previously we have learned that during the bulk condensation of a monomer of the composition $C_nN_{2n}H_{2n}$ ammonia alongside a CNH_2 species evolves starting at 450 °C; i.e. 200 °C prior to the full decomposition of the material (c.f. Figure 11). Interestingly, the point of this evolution is close to the formation temperature of melem, which is situated between 370 and 390 °C (c.f. Figure 15). Schnick *et al.* corroborated this result in a recent study.[51]

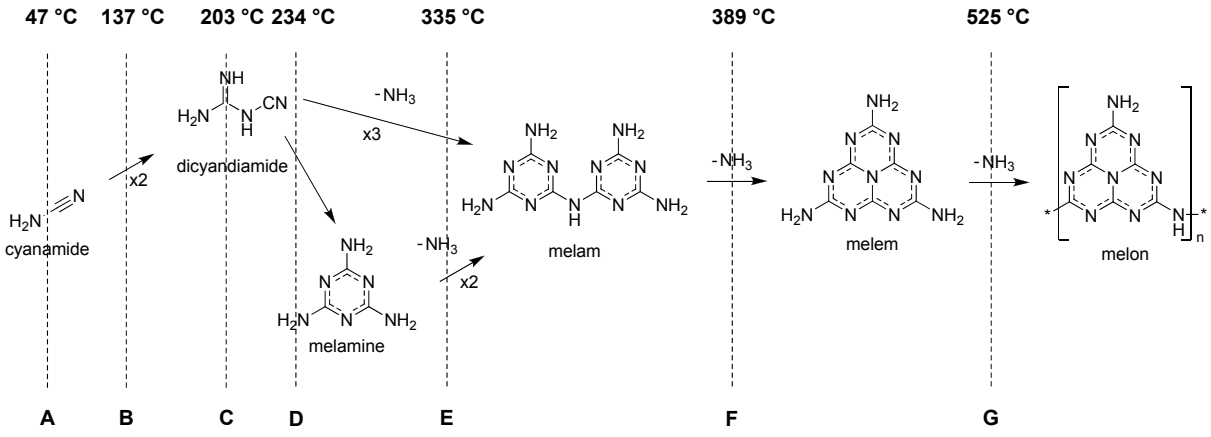

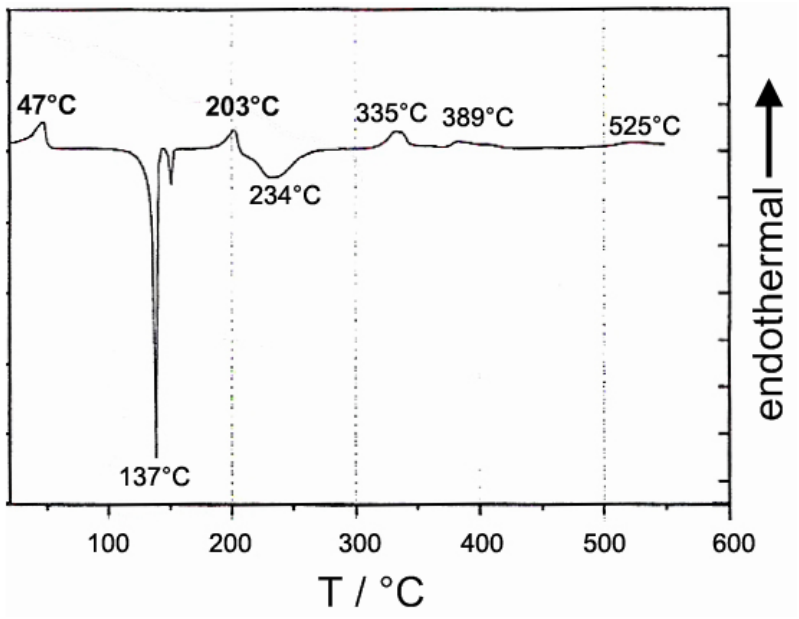

Figure 15. Differential scanning calorimetry study of the condensation of cyanamide. (A) phase transition of cynamide, (B) dimerisation of cyanamide to dicyandiamide, (C) phase transition of dicyandiamide, (D) condensation of dicyandiamide to melamine, (E) condensation of melamine to melam, (F) condensation of melam to melem, (G) condensation of melem to melon.

Simultaneous presence of such fragments suggests that major rearrangements involving opening and closing of the aromatic units must take place even after melam is formed – processes, which are not accounted for by the somewhat simplistic condensation pathway presented in Figure 11 and Figure 15. In fact the observant reader will have spotted that the steps leading from melamine to melem are nowhere as trivial as suggested. Up to this day there is no single piece of literature which satisfactory illuminates this black box, except for two references which can be found elsewhere – and which both are explicitly denominated as “possible formation mechanisms of melem”.[52, 53] Some information is of special significance though. Pooling these pieces of information together, we arrive at the reaction mechanism shown below.

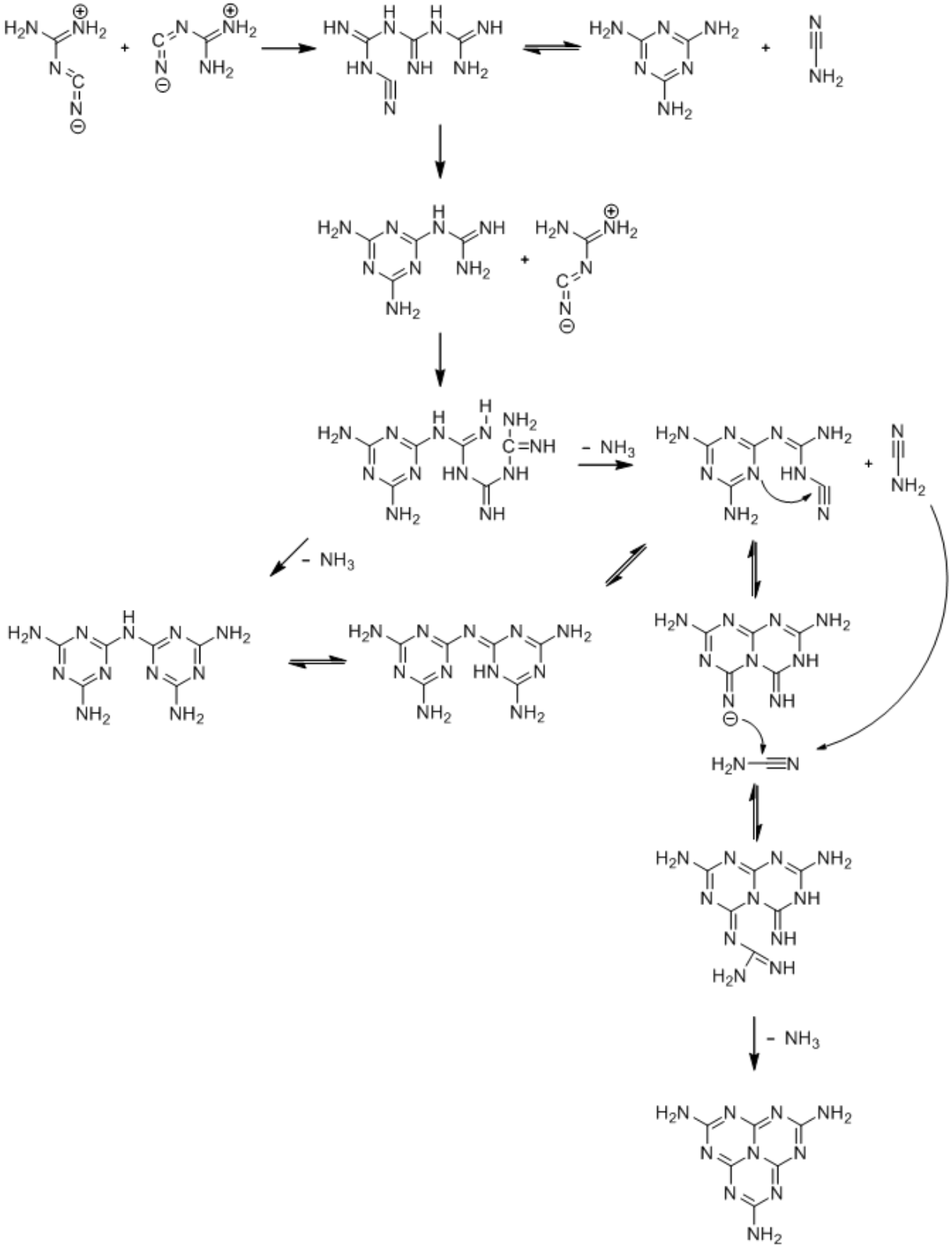

Figure 16. Proposed reaction mechanism for the condensation of dicyandiamide to melem.

There are two important facts to take away here: firstly, note that the tautomeric form of melam (melamine dimer in the centre) and the tautomerism in the last but one step

before heptazine is formed are both important, integral parts of the reaction mechanism conform with the tautomeric forms of melamine and heptazine observed by Schnick et al.[41] Secondly, we see that cyanamide (an HCN and NH_2 equivalent) is available during the whole course of the condensation, which is conform with the results of TGA/MS. Although an in-depth study of reaction kinetics and verification of all transient species was well beyond the scope of this work, we shall see in the later sections dealing with Heptazine-based frameworks (Chapter 6) that the proposed condensation pathway and mechanism shown in Figure 16 make sense.

3.4 Synthesis of graphitic carbon nitride and its intermediates in LiCl/KCl

Dicyandiamide (DCDA) (2 g, 23.79 mmol) was thoroughly grounded together with 10 g of a mixture of lithium chloride and potassium chloride (45:55 wt %). The reaction mixture was heated at 40 K min^{-1} under inert atmosphere and kept at the terminal temperature of 400 °C for 6 h. The resulting, homogenous, anhydrous block of LiCl-KCl eutectic and condensation intermediates of DCDA was subsequently sealed in a quartz glass ampoule and heated at 20 K min^{-1} to 600 °C (12 h) to obtain a higher degree of condensation. Excess salt was dissolved in boiling, distilled water and removed through repeated washing. The material was thoroughly dried at 200 °C/10^{-5} torr to yield *g*-C_3N_4 (1.42 g, 7.71 mmol, 97% yield) as a brown powder; IR (ATR FT-IR, cm^{-1}) 2179 (vw), 1610 (m), 1552 (m), 1358 (vs), 1264 (vs), 1227 (vs), 1152 (vs), 994 (m), 803 (s), 673 (m).

A series of condensation products of dicyandiamide in the salt melt was prepared in analogous fashion, terminating the reaction after 6 h at temperatures in the range of 380 °C to 600 °C in steps of 20 °C. To highlight the difference between the ionothermal and the bulk condensation route, a second series was prepared in analogous fashion with the difference being that no salt was added.

3.5 Characterisation of graphitic carbon nitride

The composition of a sample of *g*-C_3N_4 according to a preliminary elemental microanalysis was as follows: C, 31.9 %; N, 52.7 %; H, 0.67 %; O, 4.9 % with the difference

from 100 wt % being presumably due to chelated salt. Treatment of this sample with boiling sulphuric acid and subsequent Cl-, Li- and K-titration yielded the following: Cl, 3.30 %; Li, 2.62 %; K, 0.24 %. It should be noted that the hydrogen content of any C_3N_4-like material prepared from thermally induced bulk condensation without the molten salt as a solvent yielded no better value than 1.5 wt %, which would correspond to the H-content of melon rather than to an extended C_3N_4 sheet. Note also that a major part of the hydrogen content can be attributed to adsorbed water. A reasonable formulation of the dried C_3N_4 material was found to be $C_{3.0}N_{4.2}H_{0.07}$, corresponding to the expected formula of an extensively condensed material with a low degree of defects and few terminal amino groups. Strikingly the Cl-, Li- and K-titration revealed an excessive amount of lithium too large to be attributed to residual salt and too small to be a periodically incorporated constituent of the carbon nitride framework. The elusive nature of lithium with respect to most crystallographic and analytical methods challenges all general statements about its roll and situation in the material at hand.

The vibrational spectra of dicyandiamide condensed in molten salt and in the bulk were compared with the spectrum of melem (Figure 17). Several strong bands in the 1200 to 1600 cm^{-1} region were found, which correspond to the typical stretching modes of CN heterocycles. Additionally the characteristic breathing mode of the triazine units at 800 cm^{-1} is observed. It should be noted that the broad peaks at around 3000 cm^{-1} indicative of secondary and primary amines (and their intermolecular H-bonding) are absent in the spectrum of the condensation product from the molten salt. Brought into context with the low hydrogen content, this find indicates a more thorough condensation of the C_3N_4 material in the molten salt than any bulk condensation could allow so far.

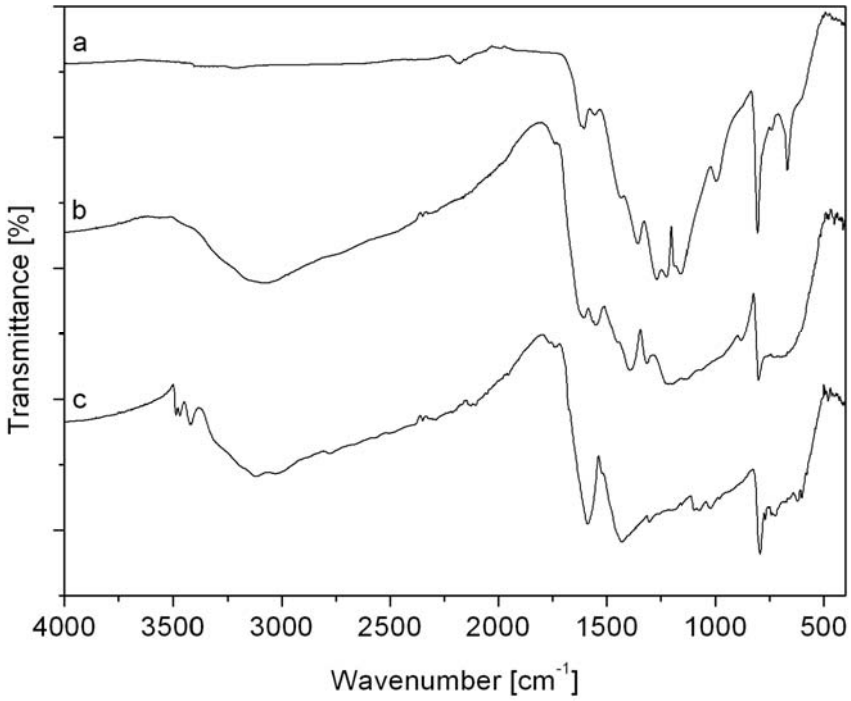

Figure 17. FTIR spectra of dicyandiamide condensed in a eutectic salt melt of LiCl/KCl (**a**), dicyandiamide condensed in the bulk (**b**), melem (**c**).

The progress of condensation via the bulk route compared with the salt melt reaction is illustrated in Figure 18, A and B respectively. The products of both condensation routes show features characteristic for aromatic CN heterocycles at 1200 to 1600 cm^{-1} and the breathing mode of the triazine units at 800 cm^{-1}. However, note should be taken that the stretching modes of secondary and primary amines and their intermolecular H-bonding interactions vanish almost completely for condensation products obtained from the salt melt at temperatures above 560 °C. This find supports the idea, that the final condensation product obtained from the salt melt is devoid of terminal, not-reacted amino groups and is cohesive as an effect of covalent interactions rather than intermolecular H-bonding.

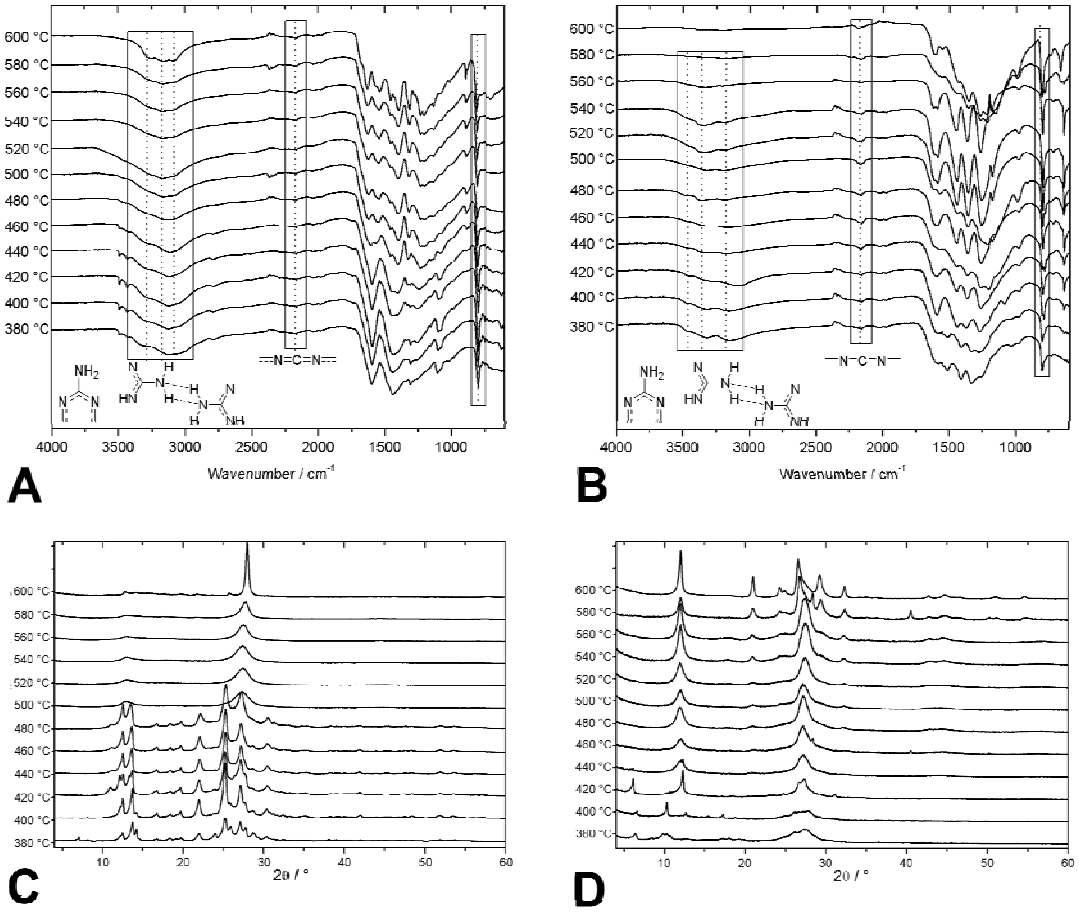

Figure 18. FTIR spectra of dicyandiamide condensed in the bulk (**A**) and in the salt melt (**B**) and their respective PXRD patterns (**C**) and (**D**).

The XRD pattern of graphitic carbon nitride obtained from thermal condensation of dicyandiamide in a molten salt was found to be well described by a hexagonal unit cell with the space group $P6_3cm$ (No. 185), with parameters $a = b = 8.434$ Å, $c = 6.722$ Å. The corresponding Bragg peak positions and systematic absences can be seen in Figure 19, A giving an excellent correlation with the experimental powder X-ray pattern. The green difference plot indicates an acceptable degree of fitting of the refined profile and of the previously calculated unit cell parameters. The fit predicts average crystallite sizes of about 200 nm, which is corroborated by electron microscopy. Furthermore, a structureless LeBail fit assuming homogenous crystallite sizes (i.e. same FWHM values) for peaks of the same phase confirms that all indexed peaks are indeed part of one unique phase. (Figure 19, A)

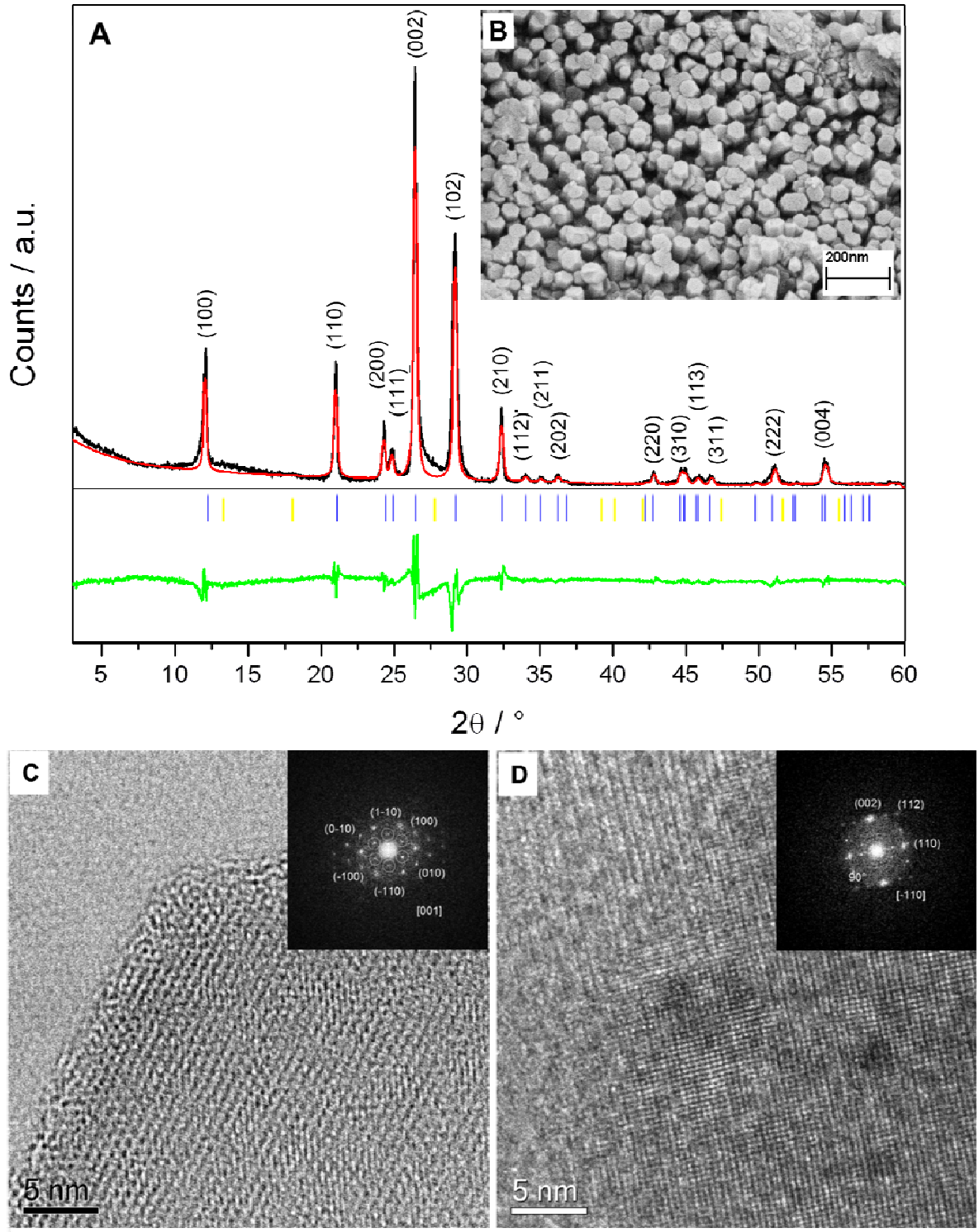

Figure 19. Physical characterisation of crystalline, graphitic carbon nitride as obtained from the quartz glass ampoule (salt melt reaction). (**A**) structureless LeBail fit performed on the XRD pattern of *g*-C_3N_4 with the observed pattern (black), the refined profile (red), the difference plot (green), Bragg peak positions (blue) and reflections limited by the space

group symmetry (yellow). (**B**) SEM picture and HRTEM pictures showing (**C**) a view in [001] direction and (**D**) a view of the [-110] zone of *g*-C_3N_4.

The strongest peak at 26.5° is well known from discotic systems as the stacking peak of conjugated aromatic rings and was indexed as (002). This corresponds to an interplanar stacking distance of d = 3.36 Å; a value which is comparable to the packing in crystalline graphite, with d = 3.35 Å.[54] Another pronounced peak is found at 12.1° which corresponds to a distance d = 7.30 Å and was indexed as (100). The structural motif giving rise to this reflection is confirmed by high-resolution transmission electron microscopy as reported below, and it is found in the possible unit cells of some of the previously reported carbon nitride materials (c.f. Figure 2) with a layer to layer distance of 3.4 Å. (Figure 21, A) The structure of the crystalline, graphitic carbon nitride can be derived in analogy to graphite. The best Rietveld fit gave a structure based on triazine units (Figure 20), however a population of the unit cell with heptazine (C_6N_7) units is possible if a less complete degree of condensation is assumed (Figure 21, B). Regardless of the composition, both model-layers are stacked in a graphitic, ABAB-fashion. It should be noted however, that the structural model chosen still is simplistic, as it assumes perfectly planar, fully aromatic C_3N_4 sheets, the absence of any stacking defects and neglects the admittedly small scattering contribution of lithium. In the light of the recent theoretical study by Senker *et al* which suggests a corrugated confirmation of individual graphitic carbon nitride sheets in *g*-C_3N_4,[55] it was not possible to investigate the nature of the dominant cohesive forces which seem to favour a perfectly planar arrangement of the graphitic sheets of the here reported material. Taking into account that residual amounts of Cl, K and Li were detectable via titration even after extensive washing, it cannot be unambiguously ruled out, that intercalation of Cl, K and Li is not taking place and could in fact be responsible for planarization due to electronic effects.

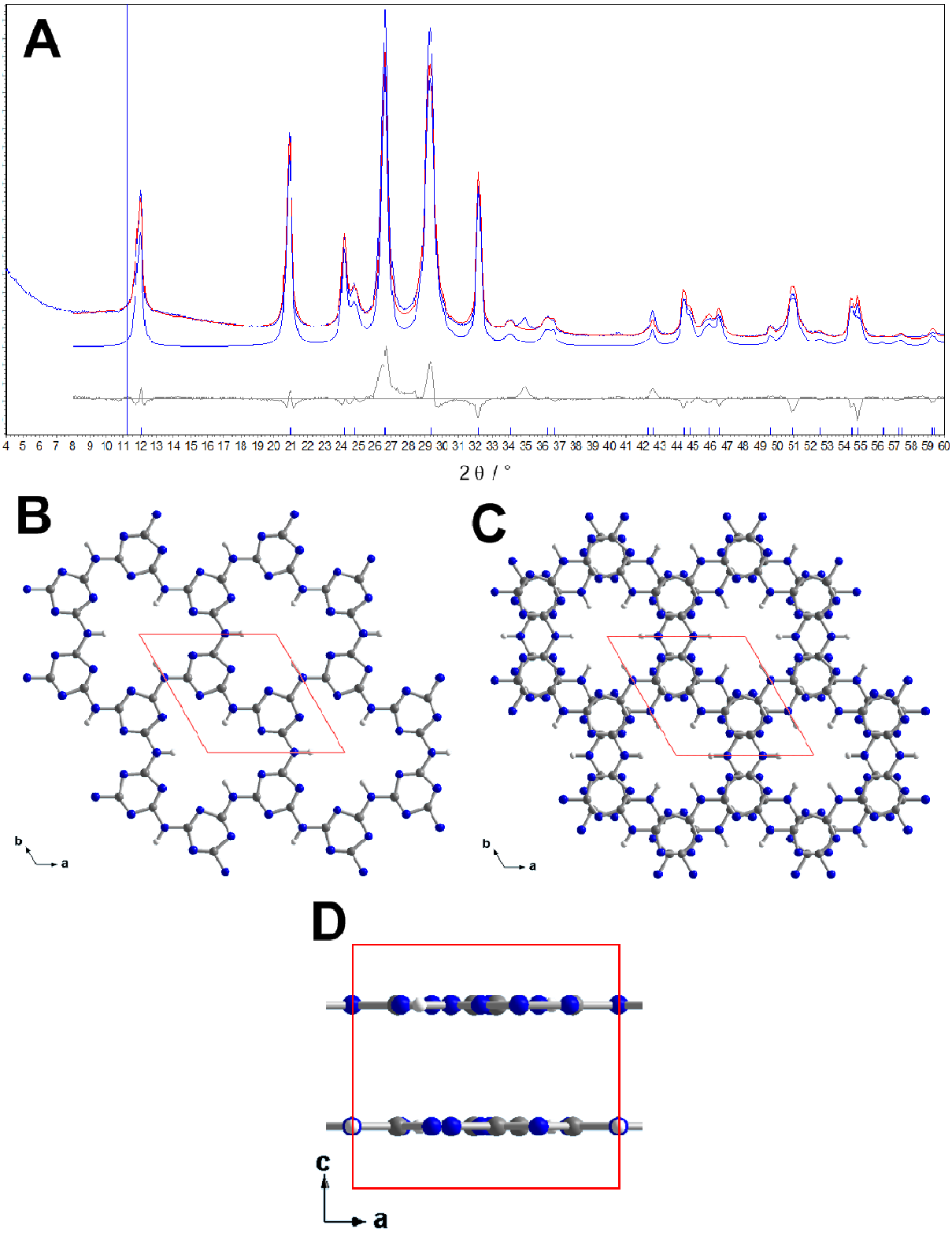

Figure 20. (**A**) Rietveld refinement using Bruker's *Topas Academic* performed on the XRD pattern of *g*-C_3N_4. Proposed structure of crystalline, graphitic carbon nitride as established from the best fit based on triazine units. Carbon, nitrogen and hydrogen atoms are represented as grey, blue and white spheres respectively – (**B**) shows one (**C**) two consecutive layers along the *c*-axis, (**D**) shows both layers along the *b*-axis. The unit cell with parameters $a = b = 8.434$ Å, $c = 6.722$ Å is indicated in red.

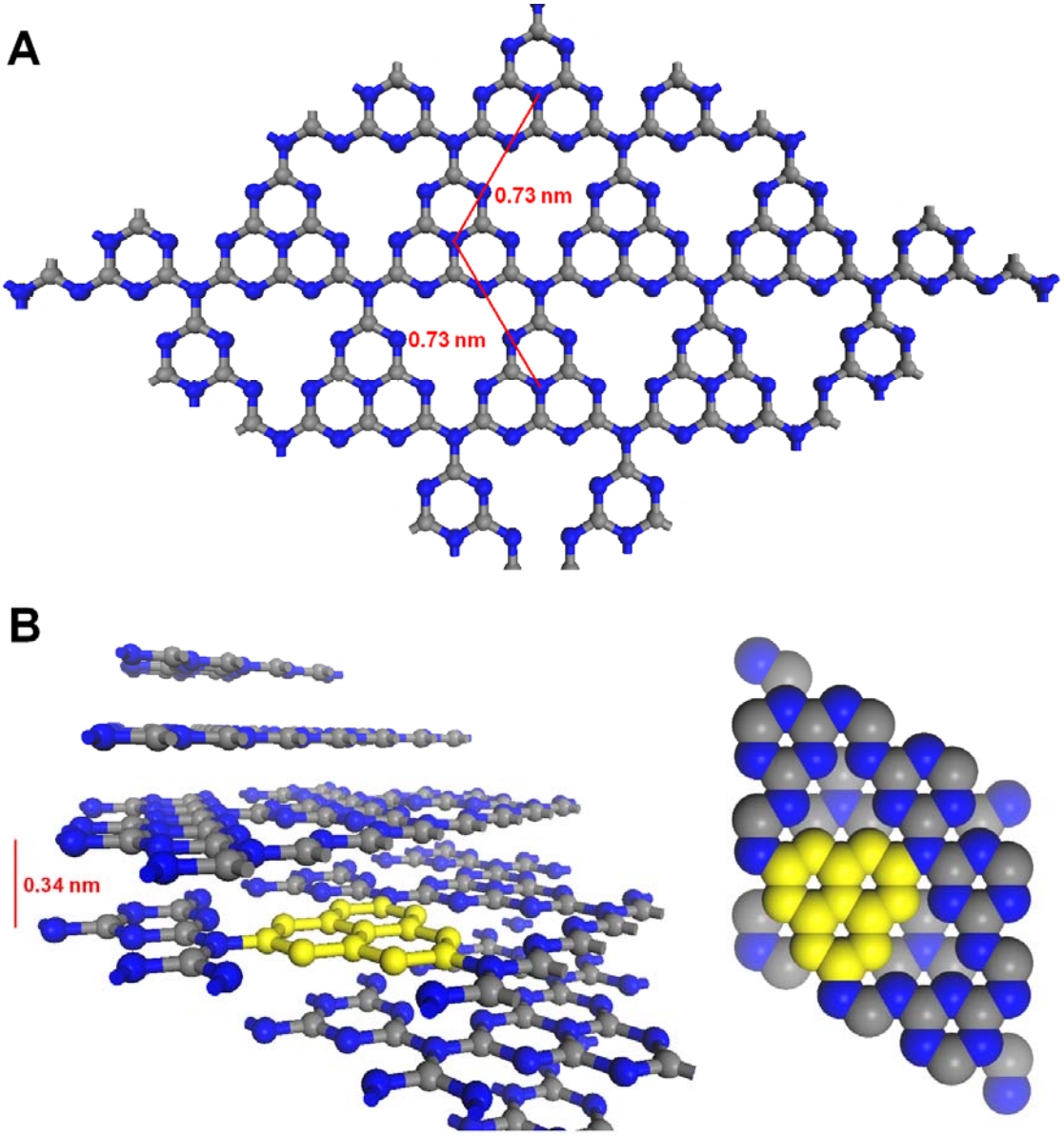

Figure 21. Proposed structure of crystalline, graphitic carbon nitride as established by geometry optimisation using Accelrys' *Materials Studio Modelling*. Carbon and nitrogen atoms are represented as grey and blue spheres respectively. In (**B**) a heptazine unit was highlighted in yellow as a guide for the eye.

The progress of condensation via the bulk route contrasted with the salt melt reaction was also monitored using powder X-ray diffraction. The bulk route produces well-known condensation products of low molecular weight in the temperature region between 380 and 480 °C as described elsewhere[6] and finally forms various oligomeric forms of Liebig's melon[51] from 500 °C onwards as seen in Figure 18, C. The terminal, polymeric structure obtained via bulk condensation has two very distinct features namely a peak at

12.7° and 27.9°. Komatsu attributed the first peak to the (110) reflection of an orthorhombic melon with *a* = 7.396 Å, *b* = 20.924 Å and *c* = 12.954 Å,[28] while Schnick et al. incorporated this peak as a (210) reflection of an orthorhombic melon with *a* = 16.7 Å, *b* = 12.4 Å and *c* = 3.2 Å.[51] Nonetheless both publications agree, that the peak at 27.9° corresponds to a layered structural motif, namely stacked chains of heptazine units linked by bridges of secondary amines.

The reaction in the salt melt progresses in a very different fashion. (Figure 18, D) The pronounced peak at 12.0° which is thought to be a structural motif of a nascent sheet of planar carbon nitride and the (001) reflection in a hexagonal unit cell containing nitrogen bridged heptazine units is formed between 440 and 460 °C; i.e. very early in the condensation process. Simultaneously, we observe the formation of a broad peak at around 27.1°, which persists up to 580 °C. This peak can be attributed to a pseudo-(002) stacking motif of the nascent graphitic carbon nitride domains, similar to the turbostratic phase of graphite.[54] As the temperature increases (540 to 600 °C) peaks with a (**l)-component become more pronounced and all visible peaks become sharper. At the same time, the FWHM value of the pseudo-(002) peak decreases as well and its position moves to the final 26.5°. This can be rationalised with increasing degree of condensation and hence an increase of crystallite size in all dimensions; especially through the stacking of extended graphitic carbon nitride sheets. Again, a study by scanning electron microscopy confirms this find showing hexagonal prisms of increasing length in Figure 22.

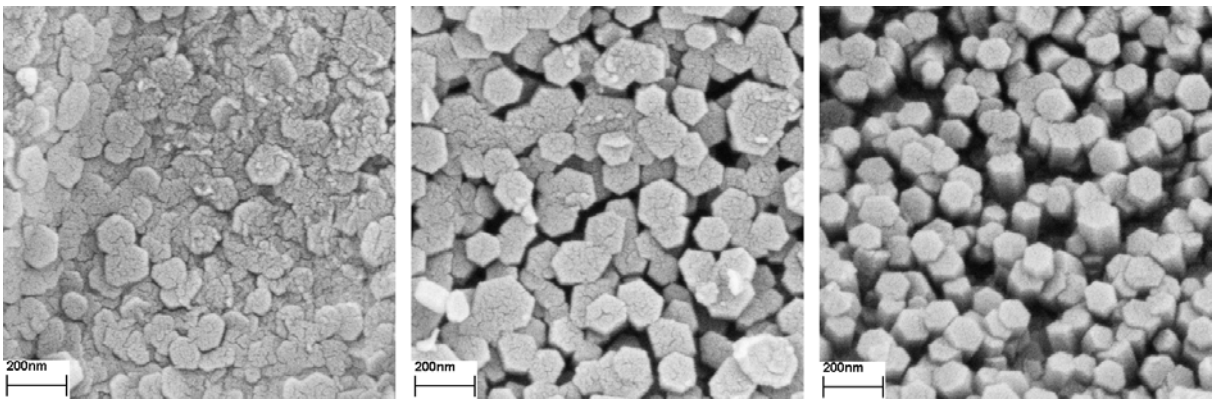

Figure 22. SEM pictures showing hexagonal prisms of increasing length visualising the preferred direction of growth in z-direction of the crystalline, graphitic carbon nitride as obtained from the salt melt.

Samples of crystalline, graphitic carbon nitride were sufficiently stable to allow HRTEM and EELS measurements. Figure 19, C shows view in [001] direction on the edge of one of the hexagonal prisms visible in the SEM. Measurements of the in-plane distance reveal a *d*-spacing of 7.25 Å at an angle of 60° which corresponds to the spacing of coplanar, N-linked heptazine units and is in perfect agreement with the PXRD data. Figure 19, D shows a view of the [-110] zone axis of the *g*-C_3N_4. The two measured distances would in this case correspond to the (002) and (110) planes, revealing thus the interlayer spacing of the heptazine units as well as the interplanar spacing already found with the corresponding XRD measurements. The EELS spectrum of the samples (Figure 23) shows that the system is composed of sp^2-hybridized carbon and nitrogen atoms, as indicated by the presence of the 1s → π* transition for both elements. The carbon-K-ionisation edge and nitrogen-K-ionisation edge show nearly identical near edge structures indicating a similar threefold coordination and electronic environment of both carbon and nitrogen in the synthesized material. Furthermore the Cl-L-ionisation edge confirms residual chlorine, as established via elementary analysis. In addition note that no energy loss due to oxygen could be detected, corroborating that the oxygen content established from elemental microanalysis cannot be attributed to an intrinsic structural component of the product.

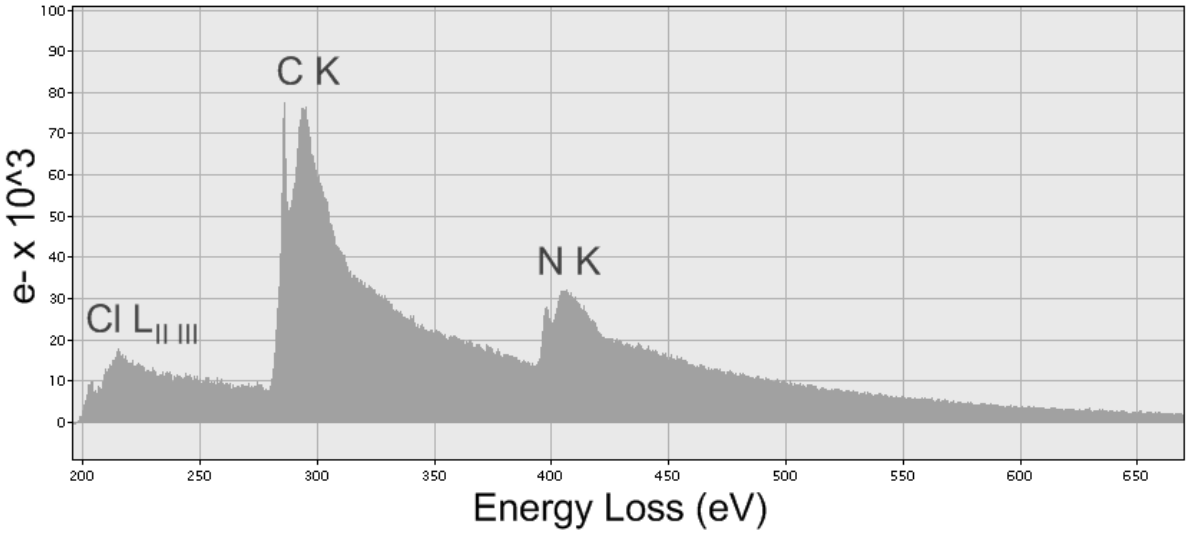

Figure 23. EELS spectrum of carbon and nitrogen K edges recorded for *g*-C_3N_4.

We have seen here the formation of highly crystalline, graphitic carbon nitride by a simple self-condensation process of dicyandiamide in a salt melt of lithium chloride and potassium chloride and contrasted it with Liebig's melon as received via the traditional bulk condensation route. FTIR and elemental analysis of the product hint towards a structure with few defects and few unreacted end groups and hence to an extensively condensed framework. PXRD analysis and high resolution transmission electron microscopy show the presence of pronounced in-plane ordering with a repeat distance of d = 7.30 Å – which could correspond to a separation of coplanar, covalently linked heptazine units in a defect-rich material, or to the ordering of N-linked triazine units – and a planar, graphitic interlayer distance of d = 3.36 Å. Taking these finds into consideration, the structural model for the material obtained is based on extended sheets of covalently linked *s*-heptazine (C_6N_7) units which stack in a graphitic fashion, supporting predictions of Kroke *et al*.[13]

The following chapters will elaborate on the particularities of the control of the condensation and crystallisation process of *g*-C_3N_4. We will see how the choice of the solvent holds the key in the manufacturing of new carbon nitride allotropes and how such a material could be used to create intercalation compounds of *g*-C_3N_4, analogous to graphite opening up applications in the field of lasers and photo-catalysts, to name only two.

4 A new phase of graphitic carbon nitride – *g*-C_3N_4-mod2, analogous to rhombohedral graphite

4.1 A toolbox of solvent systems for ionothermal synthesis

The eutectic salt-melt of lithium chloride and potassium chloride is not the end of the road for ionothermal synthesis. A quick glance at the "Molten Salts Handbook"[56] reveals a whole multitude of salt-melts with suitable melting points to match our synthetic requirements. An overview of suitable eutectic melts is given below:

Class				m.p. / °C
A	LiCl (45 wt%)	KCl (55 wt%)		352
B	NaCl (11 wt %)	KCl (14 wt%)	$ZnCl_2$ (75 wt%)	203
C	LiCl (43 wt%)	KCl (52 wt%)	NaCl (5 wt%)	335
D	LiBr (52 wt%)	KBr (48 wt%)		348

The binary and ternary mixtures can be sorted into four different classes denoted A through C. Class A contains a small anion (Cl) and a mix of a small (Li) and a large (K) cation, B contains a small anion and to a large excess a large, catalytically active cation (Zn), C contains a small anion and a full scope of cations ranging from small (Li), to medium (Na) to large (K), and D contains a large anion (Br) and a mix of a small and a large cation.

The following section will deal exclusively with the contrast between products from class A and D salt melts, some words should be devoted to successful experiments performed in the other two solvent classes. Ionothermal reaction of nitriles in $ZnCl_2$ was established previously by Kuhn et al. to yield high surface area organic materials featuring both micro- and mesopores based on polytriazines.[57] Therein, $ZnCl_2$ acted both as solvent and catalyst. A reaction of dicyandiamide and of 1-cyano, 4-(2,4-diamino-1,3,5-triazino)benzene (ArCNTz, seen again in chapter 6.3) in class B solvents yielded a material with a high surface area and distinct crystal structure. A reaction of dicyandiamide in class C solvents gave a mixture of the carbon nitride phases encountered both in chapter 3 and 4. Although these results are not disclosed in the work at hand, they should be kept in mind as

a pool of potential new tools in the quest for other carbon nitride allotropes and nanostructures.

4.2 Synthesis and characterisation of the graphitic carbon nitride, g-C_3N_4-mod2

The lithium bromide and potassium bromide salt-melt was used in analogous fashion to the LiCl/KCl eutectic in chapter 3 with some slight variations. Dicyandiamide (DCDA) (2 g, 23.79 mmol) was thoroughly grounded together with 10 g of a mixture of lithium bromide and potassium bromide (52:48 wt %). The reaction mixture was heated at 40 K min^{-1} under inert atmosphere and kept at the terminal temperature of 400 °C for 12 h. The resulting, homogenous, anhydrous block of LiCl-KCl eutectic and condensation intermediates of DCDA was subsequently sealed in a quartz glass ampoule and heated at 20 K min^{-1} to 600 °C (48 h) to obtain a higher degree of condensation. The quartz ampoule was cooled to room temperature with 8 K h^{-1}. The slow cooling ramp was chosen to increase the size of the crystallites. Excess salt was dissolved in boiling, distilled water and removed through repeated washing. The product was thoroughly dried at 200 °C/10^{-5} torr to yield the graphitic carbon nitride material, which we will designate for clarity as *g*-C_3N_4-mod2 (1.22 g, 6.62 mmol, 83% yield) as a brown-red powder. A series of condensation products of dicyandiamide in the salt melt was prepared in analogous fashion, terminating the reaction after 6 h at temperatures in the range of 380 °C to 600 °C in steps of 20 °C. Note that these samples were heated in open crucibles.

Elemental microanalysis and titration of a sample of *g*-C_3N_4-mod2 gave the following values: C, 34.7 %; N, 56.4 %; H, 0.82 %; O, 4.7 %; Br, 2.26 % with the difference from 100 wt % being presumably due to either Li- or K-ions. As expected the hydrogen content of *g*-C_3N_4-mod2 is very low with a major part of the hydrogen probably due to adsorbed water. A reasonable formulation of the dried C_3N_4 material was found to be $C_{3.0}N_{4.18}H_{0.09}$; very close to the carbon nitride material obtained from the LiCl/KCl salt-melt as outlined in chapter 3. The size difference between Br- and Cl-anions would have most likely featured in a preferential uptake of either one if indeed any anion would be an integral part of the carbon

nitride structure. However, the residual Br-content matches the Cl-content of the previously prepared graphitic carbon nitride supporting the idea, that the remaining anions are most likely due to pockets of salt enclosed during the growth process of the carbon nitride framework.

The vibrational spectra of dicyandiamide condensed in LiBr/KBr and in LiCl/KCl were compared with the spectrum of dicyandiamide condensed in the bulk (Figure 24). The region from 1200 to 1600 cm^{-1}, which is characteristic for stretching modes of CN heterocycles, could not be well resolved for the product from the LiBr/KBr eutectic. However, the breathing mode of the triazine units is still well observed at 800 cm^{-1}. It should be noted that the broad peaks at around 3000 cm^{-1} indicative of secondary and primary amines (and their intermolecular H-bonding) are absent in the spectrum of both the condensation products from the molten salts, which is in agreement with the results of the elemental analysis. In both cases we are dealing with an extended carbon nitride framework with few defects and secondary or primary ammonia groups.

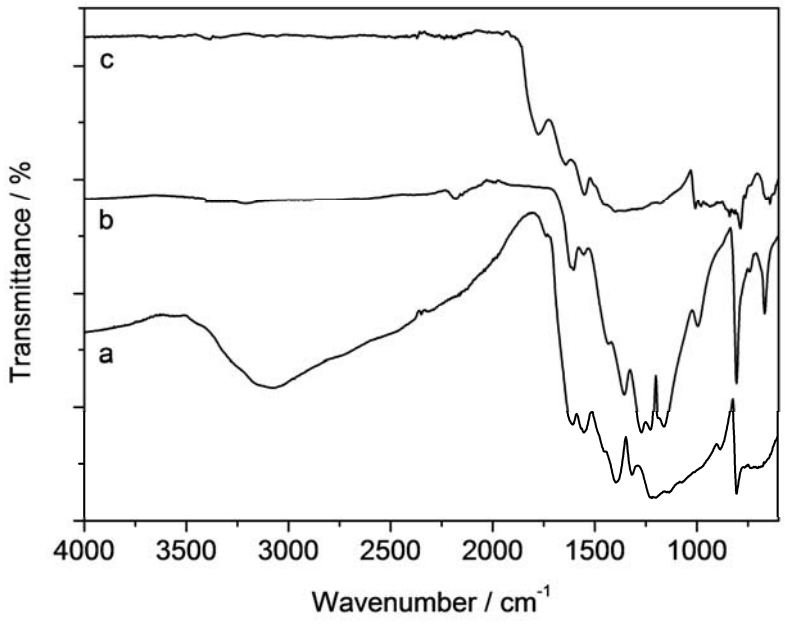

Figure 24. FTIR spectra of dicyandiamide condensed in the bulk (**a**), dicyandiamide condensed in a eutectic melt of LiCl/KCl (**b**), dicyandiamide condensed in a eutectic melt of LiBr/KBr (**c**).

From the elemental analysis and vibrational spectroscopy the difference between the graphitic carbon nitrides obtained from two different solvent systems is not apparent. Should we not expect the same product given that the condensation pathway outlined above is not obstructed by the partaking of any of the ionic species from the solvent?

The main difference between both systems becomes apparent when we consider the structural information. The powder XRD patterns of *g*-C_3N_4-mod2 and the graphitic carbon nitride from the eutectic melt of LiCl/KCl are shown contrasted with one another in Figure 25. The indexed Bragg peak positions of all in-plane reflections of a hexagonal unit cell with the parameters $a = b = 8.434$ Å are superimposed on both patterns. We observe that all (*h k* 0)-peaks remain mostly unchanged; i.e. the in-plane order remains the same as proposed in Figure 21, A, namely a layer of nitrogen bridged heptazine units. Peaks which do not match in positions all have in common that they contain an (* * *l*)-component. In other words, the reflections which are determined by inter-planar order have changed, and so has presumably the packing motif.

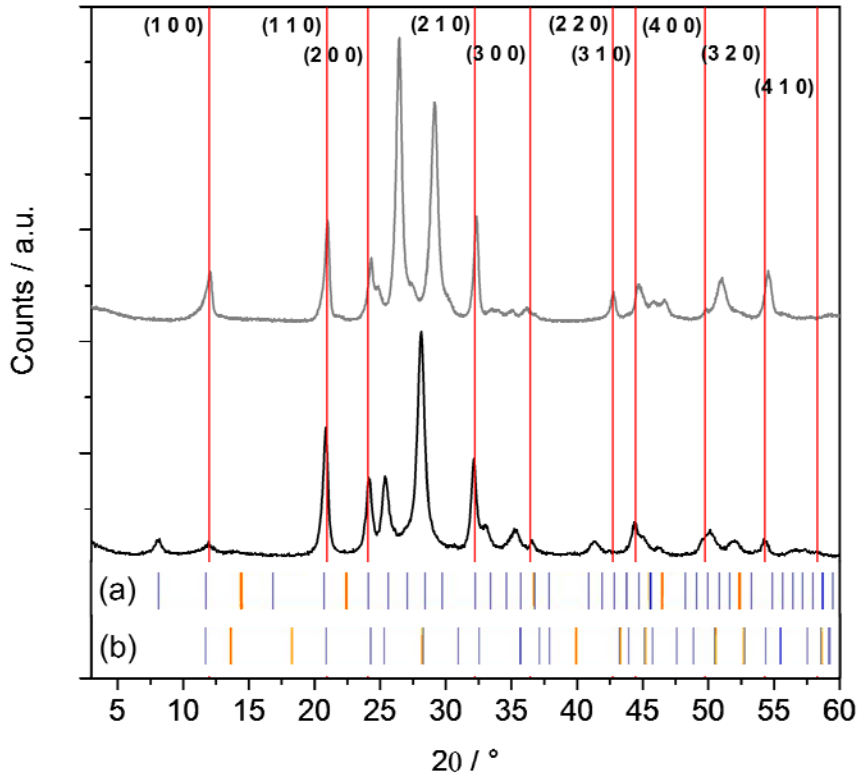

Figure 25. Powder XRD pattern of *g*-C_3N_4-mod2 (black) and graphitic carbon nitride as obtained from the LiCl/KCl eutectic (grey), Bragg peak positions (blue) and reflections limited by space-group symmetry (orange) for two different hexagonal unit cells with parameters (a) $a = b = 8.434$ Å and $c = 10.560$ Å and (b) $a = b = 8.434$ Å and $c = 7.040$ Å (both

assuming an interlayer spacing of 3.520 Å) and all (*h k* 0) reflections (red) to shown the preservation of in-plane order between the two carbon nitride species.

The change in crystallographic structure during the formation of *g*-C_3N_4-mod2 was monitored in Figure 26. The peak at 12.0 °, which is indicative of the (100) reflection in a hexagonal unit cell that contains nitrogen-bridged heptazine units, forms early in the reaction between 440 and 460 °C. Stacking, however, remains mostly disordered with more pronounced (** * l*)-peaks developing very late above 580 °C. The unit cell dimension in direction of the *c*-axis remains a challenge. Two plausible models are suggested. Figure 25, (a) shows the Bragg peak and systematic absences of a hexagonal unit cell with a glide plane perpendicular to the (*a*+*c*)-axis (2*h* + *k* = 2n) with the parameters *a* = *b* = 8.434 Å and *c* = 10.560 Å, while Figure 25, (b) is modelled on a hexagonal unit cell with a glide plane perpendicular to the *b*-axis (*l* = 2n) with the parameters *a* = *b* = 8.434 Å and *c* = 7.040 Å. Now this apparent discrepancy does not affect the general concept of a graphitic system of stacked sheets of nitrogen bridged heptazine units.

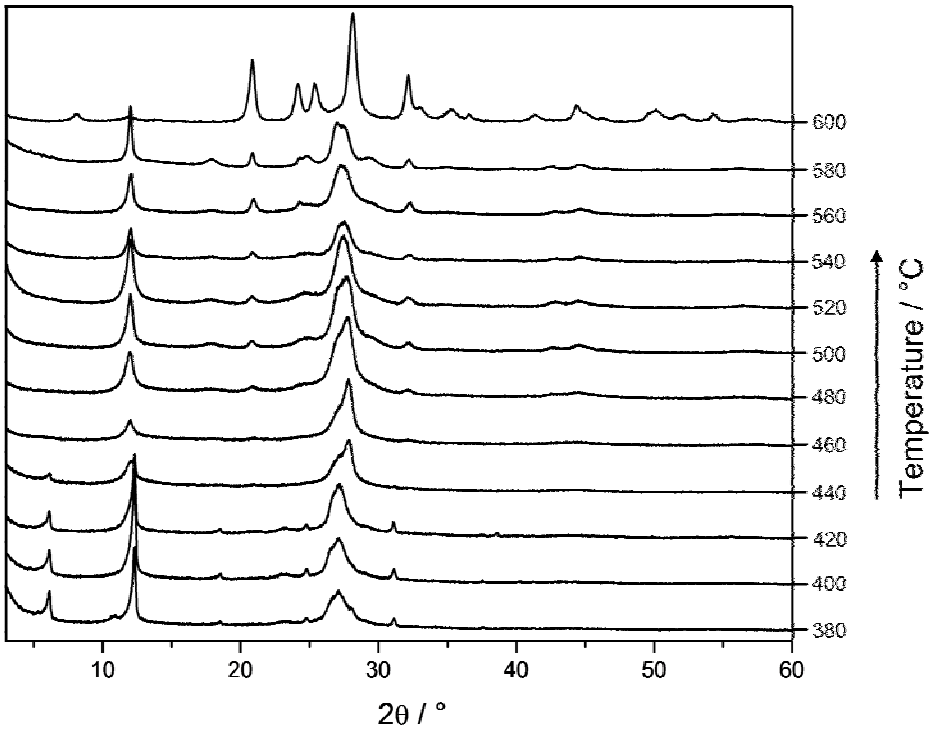

Figure 26. PXRD patterns of dicyandiamide condensed in the LiBr/KBr salt melt and terminated at the temperatures given.

Note that in both cases the stacking distance between two sheets is assumed to be 3.520 Å with model (b) being the double- and model (a) the triple-distance before the stacking pattern of sheets from one unit cell maps onto the next unit cell. This stacking distance is not unusual for discotic, aromatic systems and compares well with the stacking distance of sheets of graphitic carbon nitride obtained from LiCl/KCl (*d* = 3.36 Å) and to the packing in crystalline graphite (d=3.35 Å). Note however, that the interlayer distance in *g*-C_3N_4-mod2 is somewhat larger by approximately 0.15 Å. One possible explanation for this apparent gallery height is corrugation of graphitic carbon sheets which was postulated by Carlsson in a previous publication.[58] Such a wave formation does not change the actual gallery height but the apparent length of the unit-cell repeat along the c-axis and could account for the observed difference. Now one other possible cause of such an extension of gallery height could be imposed by the packing motif itself. We have seen in chapter 3 that graphitic carbon nitride obtained from the eutectic salt melt LiCl/KCl stacks in a graphitic, AB fashion. This packing motif accommodates the unsaturated, aromatic heptazine unit of layer A above the cavity spanned by three heptazine units of layer B. In this way, repulsion between the aromatic units is minimised. On the other hand, a packing motif in which the heptazine unit of layer A can be fully or partially superimposed on a heptazine unit in the next layer will experience stronger repulsion between the π-systems in each sheet. Such an AA' packing motif would presumably account for an increased interlayer spacing and would conform model (b). A more exotic packing motif e.g. ABA' or ABC could accommodate three layers in one unit cell and would be in agreement with model (a). The verification of these hypotheses poses one fundamental problem. Both models assume large unit cells of 650 $Å^3$ for case (a) and 433 $Å^3$ in case (b). In-depth structure analysis and determination of atomic coordinates exclusively for light (i.e. weakly scattering) atoms from powder XRD patterns hence becomes a redundant task – in fact, just about any set of light atoms could match the peak intensities. It would be more prudent at this point to look for evidence elsewhere.

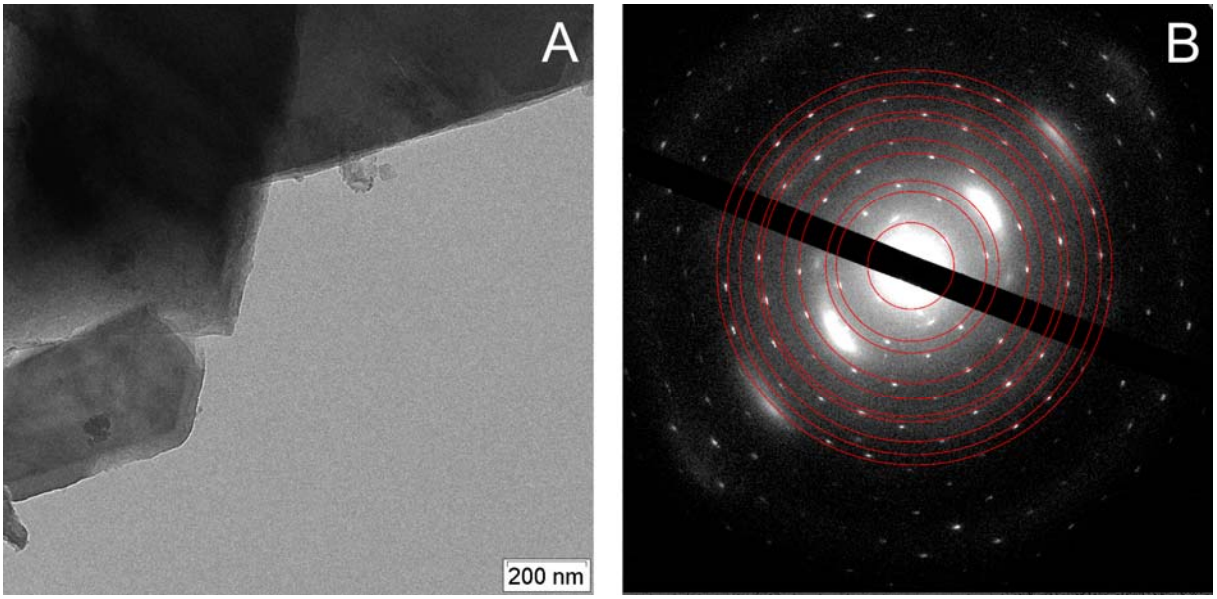

Figure 27. TEM picture (**A**) and corresponding selected area electron diffraction (**B**) of dicyandiamide condensed in the LiBr/KBr salt melt (*g*-C_3N_4-mod2) both revealing characteristic hexagonal angles and patterns.

Figure 27, B shows an electron diffraction study of the area shown in Figure 27, A. Firstly, the hexagonal pattern of the diffraction peaks is apparent to the bare eye. Verification of distances and angles confirms that we are looking in the (0 0 *l*)-direction, i.e. perpendicular to the graphitic carbon nitride plane. Centrosymmetric rings were drawn through the diffraction spots, and their diameters were compared to an aluminium standard. The ring radii were converted to real space distances and are given from centre to outer ring in the table below:

		ED	XRD	
ring #	d / Å	2θ(calc) / °	2θ(obs) / °	(*h k l*)
1	7.3793	11.9836	12.108	(1 0 0)
2	4.2573	20.8486	21.051	(1 1 0)
3	3.6897	24.1006	24.354	(2 0 0)
4	2.7672	32.3256	32.405	(2 1 0)
5	2.4489	36.6672	36.890	(3 0 0)
6	2.1369	42.2587	42.857	(2 2 0)
7	2.0498	44.1466	44.700	(3 1 0)
8	1.8448	49.3602	49.904	(4 0 0)
9	1.7135	53.4293	54.737	(3 2 0)
10	1.6135	57.0326	57.803	(4 1 0)

The real space distances were correlated with expected and observed reflections in the powder XRD pattern in Figure 25 and gave a perfect match. Furthermore the distance between the electron scatterers which give rise to the observed diffraction spots was found to be 7.38 Å, which we established previously as the ideal distance between nitrogen linked, co-planar heptazine units. We knew already that we are dealing with sheets matching in structure and chemistry to the previously obtained graphitic carbon nitride. But the quality and size of crystals obtained from the LiBr/KBr eutectic should give reason for amazement. Figure 28 shows typical particle morphologies found for *g*-C_3N_4-mod2 after removal of the salt. While crystallite sizes did not seem to exceed the order of magnitude of 200 nm for the condensation product of dicyandiamide obtained from the LiCl/KCl eutectic, Figure 28 shows splinters of hexagonal crystals of the order of magnitude of 500 to 2000 nm and sharp breaking edges with characteristic 120° and 60° angles.

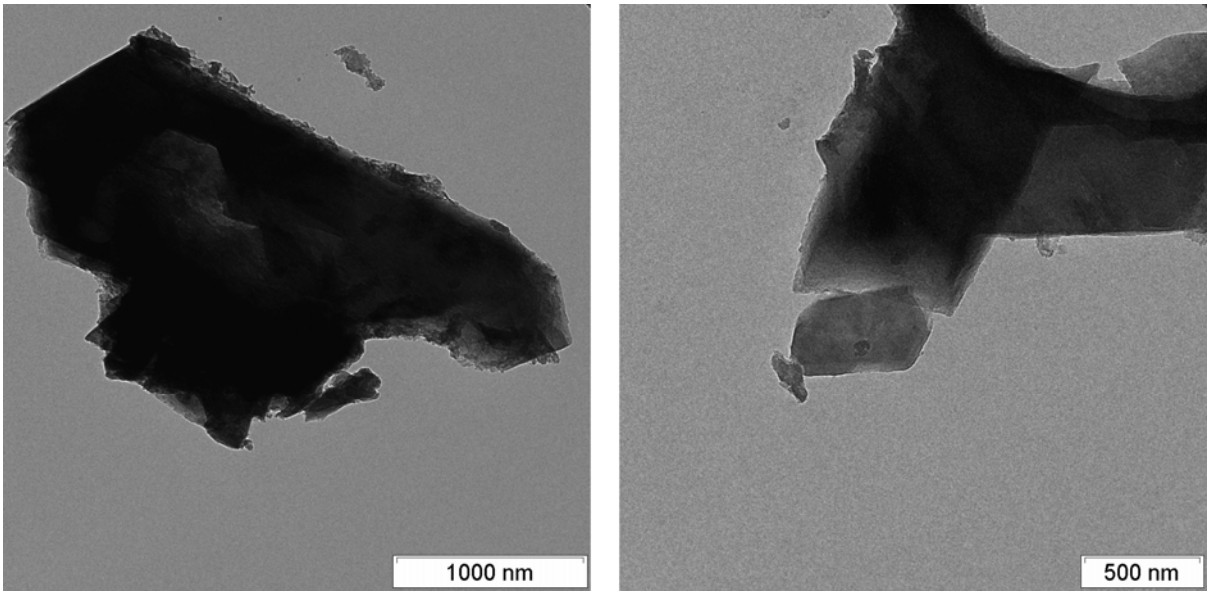

Figure 28. Representative TEM pictures of *g*-C_3N_4-mod2 showing sharp breaking edges with characteristic 120° and 60° angles.

Coming back to the seemingly unresolved question of an interplanar stacking order, brings us back to Figure 27, B which holds more information. Figure 29 shows the aforementioned electron diffraction pattern but this time centrosymmetric rings were drawn through the smeared out diffraction spots found on a line passing though the centre of diffraction. Correlation with real space gave distances of 3.52 Å for the inner ring and 1.76 Å for the outer ring (25.28° and 51.91° respectively in terms of 2θ). For one, this find

supports the notion that 3.52 Å was correctly assigned as the interplanar stacking distance in the previous powder XRD study. Unfortunately the one missing piece of information to clearly distinguish between both models outlined above would be the unambiguous presence (or absence) of a similarly shaped diffraction spot on the orange ring seen in Figure 29. This diffraction spot could verify whether the low angle peak seen at 8.3° in the powder XRD pattern indeed is an integral part of the stacking reflection of three layers in an ABC fashion or not. However, the assumed position of this diffraction peak coincides with the evanescence of the primary electron beam, and no definite answer can be given by this method.

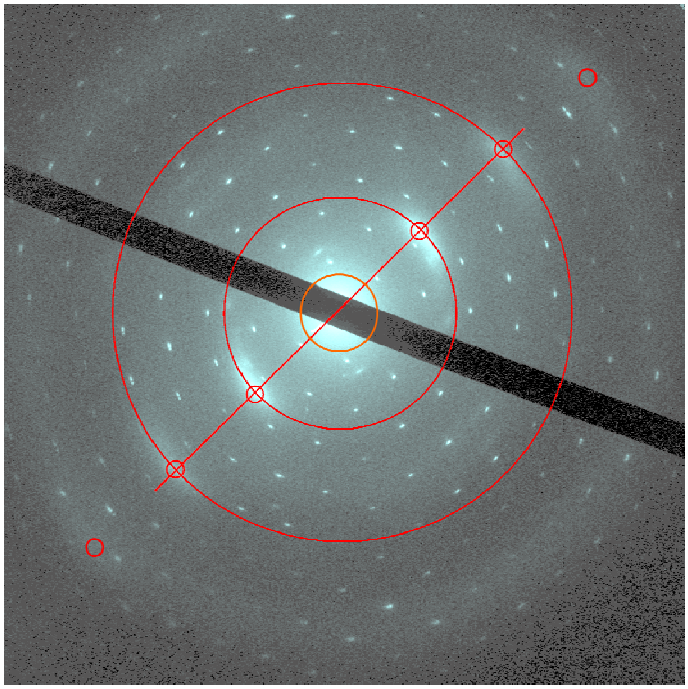

Figure 29. Selected area electron diffraction (SAED) pattern of *g*-C_3N_4-mod2. Red spots and rings mark (0 0 *l*)-peaks.

The possibility of a triple stacking motif for graphitic carbon nitride should not come as a big surprise. We have established earlier, that graphitic carbon nitride obtained from lithium chloride and potassium chloride packs in analogy to graphite in an AB-fashion. And again it is the graphite system which provides the example of a "defect" stacking motif, namely ABC in its rhombohedral phase.[59, 60] Applying the specifications of the symmetry of rhombohedral graphite to our previously calculated space group parameters we can propose the ABA' packing motif for the carbon nitride sheets in which the B-sheet is offset

by 8/9 units in term of the *a*-vector and the A'- (or C-) sheet is offset by 3/9 units in term of the *a*-vector. The resulting structure and its analogy to rhombohedral graphite is seen in Figure 30.

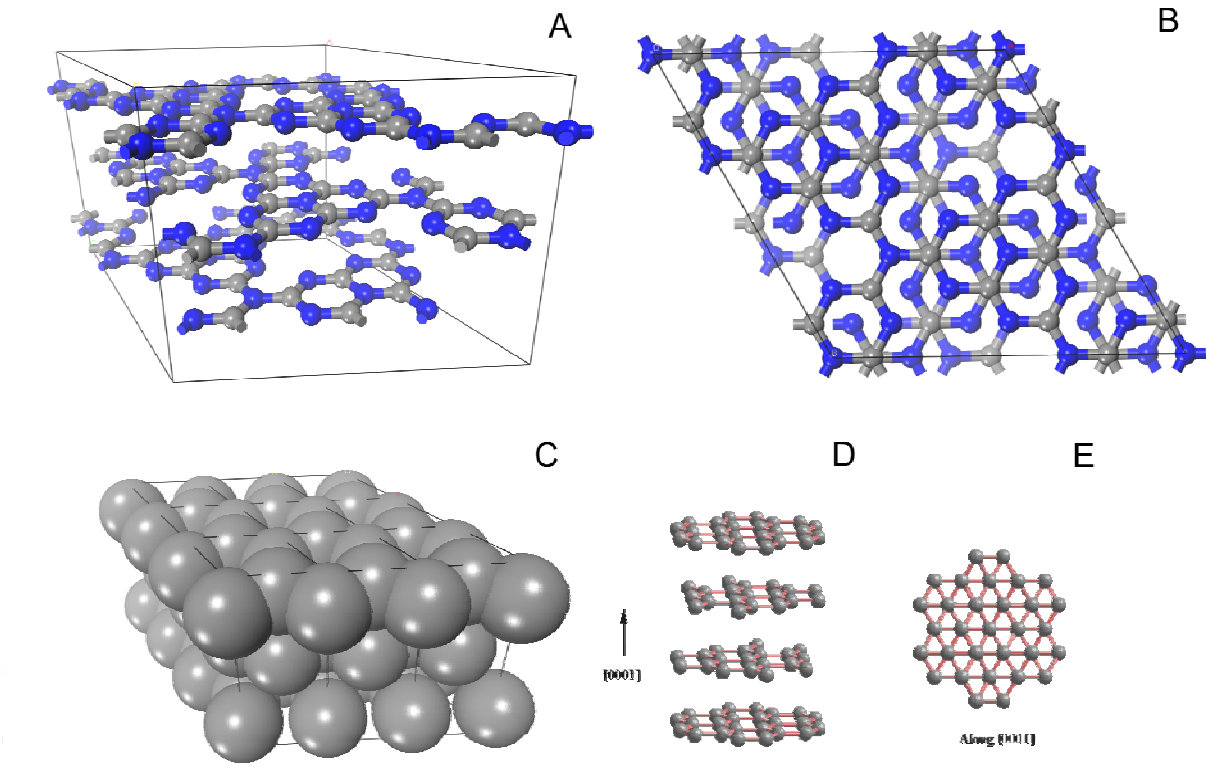

Figure 30. Proposed structure of crystalline, graphitic carbon nitride (*g*-C_3N_4-mod2) (**A**, **B**) analogous to rhombohedral graphite (**C**, **D**, **E**).

This leaves us with the ultimate question as to why two different solvent systems give two so distinctly different crystal structures and morphologies under the same reaction conditions. As so many times the answer is hidden within the question. We have seen that during the condensation process of dicyandiamide in the LiBr/KBr eutectic melt the interplanar order (in terms of pronounced diffraction peaks with (* * *l*)-component) does not materialise until very late in the heat procedure. On the other hand we have seen that up to 5 fold larger platelets of carbon nitride are obtained from a LiBr/KBr eutectic melt as compared to the dimensions of the hexagonal prisms coming from LiCl/KCl. Since virtually no kinetic or solvochemical data is available on the LiCl/KCl and LiBr/KBr eutectic melts, it can only be surmised that the eutectic salt melt of lithium bromide and potassium bromide

must be a better solvent for individual sheets of carbon nitride allowing for longer condensation times and hence larger aggregates. This solvochemical stabilisation could prevent individual sheets from finding a thermodynamically favourable packing motif until very late into the reaction, when large and mostly immobile sheets precipitate from the solution.

This chapter demonstrated with what relative ease a new crystal phase of the graphitic carbon nitride – a class of material not known until recently – could be obtained just by the variation of the solvent. Although no further light could be shed on the actual structure of *g*-C_3N_4-mod2, the study at hand established the "toolbox of solvent systems" as an important component of ionothermal synthesis. Even at temperatures usually alien to the organic or polymeric chemist (i.e. above 350 °C) principles of solvation and crystal growth persist. The empirical find that Br-based solvent systems might be of greater use to solubilise aromatic species like graphitic carbon nitride will be a concept we will revisit in chapter 6.

5 Graphite chemistry with g-C_3N_4 – reductive intercalation

In the previous chapter 3 we have seen some of the structural and chemical analogies between the lamellar carbon nitride allotrope *g*-C_3N_4 and graphite, the layered allotropic modification of carbon. In both materials light atoms are covalently linked in parallel planes, in each of which they form a network of hexagons with interatomic distances close to these of fully aromatic molecules. The distance between parallel planes in graphite (3.35 Å) and in graphitic carbon nitride (3.36 Å) is slightly smaller than the van der Waals thicknesses of aromatic molecules (between 3.4 and 3.6 Å). The absence of covalent bonding between the parallel carbon layers in graphite makes possible the intercalation of monoatomic or monomolecular layers of various substances such as alkali metals, halogens, strong acids and metal halides. Such lamellar compounds of graphite with intercalated alkali metals were first observed in 1926.[61] They have continued to attract the attention of research workers, since they have much in common both with "solid solutions" and with the complexes formed by alkali metals with aromatic hydrocarbons. The unusual structure of lamellar compounds of graphite with alkali metals confers on them several interesting properties. Thus those with potassium, rubidium, and caesium are superconductors, react with hydrogen and nitrogen, catalyse the *ortho-para* conversion of hydrogen, and catalyse the isomerisation and the polymerisation of alkenes. Furthermore, alkali metal intercalates have received much attention due to their electronic properties. The sizeable diamagnetic susceptibility of the graphite is lost, and a small Pauli paramagnetism arises.[62, 63] In-plane electrical conductivity increases 10-fold and approximately 200-fold along the c-axis at the first stage.[64, 65] Literature covering alkali metal intercalates extensively can be found elsewhere,[66, 67] but in summary, the electronic properties of MC_x compounds are consistent with reduction of the graphite upon intercalation.

Apart from these interesting chemical properties, there is reason to believe that graphite sheets may form multiwalled nanotubes through a scrolling mechanism.[68, 69] A recent paper by Viculis *et al.*[70] showed that carbon nanoscrolls can be obtained when the first-stage intercalation compound of graphite and potassium, KC_8, is exfoliated in a highly exothermic reaction with an aqueous solvent, as given below:

$$KC_8 + CH_3CH_2OH \longrightarrow 8\,C + KOCH_3CH_3 + 1/2\,H_2$$

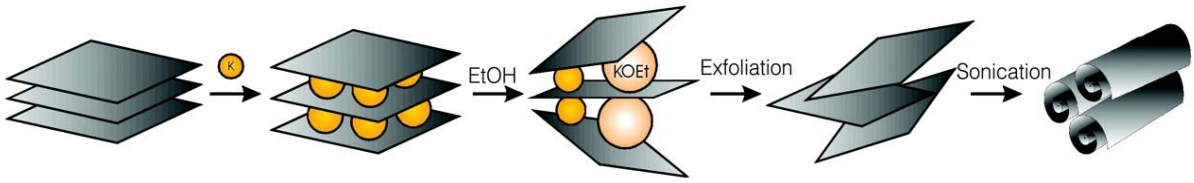

Figure 31. Schematic of the intercalation/exfoliation process. Graphite is intercalated with potassium metal and then exfoliated with ethanol (EtOH) to form a dispersion of carbon sheets. Sonication produces carbon nanoscrolls.

This facile concept which seamlessly worked for the graphitic carbon system was applied to the graphitic carbon nitride system in turn.

5.1 Synthesis and characterisation of $K(C_6N_8)_3$ – a potassium intercalation compound of g-C_3N_4

A Pyrex tube containing graphitic carbon nitride as obtained via the procedure outlined in chapter 3.4 was evacuated and thoroughly dried. Potassium was added under inert helium atmosphere, and the tube was sealed and heated for 72 hours at 200 °C. The initially (light) brown powder of *g*-C_3N_4 transformed into a black powder as the silvery ball of molten potassium gradually disappeared. The powder was thoroughly examined by x-ray diffraction, TEM and SEM, and it should be noted that it remained stable under air throughout, while KC_8 is an extremely air and moisture sensitive material by comparison.

Figure 32 shows a comparison of the x-ray diffraction patterns of the starting material, *g*-C_3N_4, and the potassium intercalation compound, $K(C_6N_8)_x$. Note the new peaks in the pattern of the intercalation compound, of which some coincide with the hypothetical positions of peaks not observed in the pattern of *g*-C_3N_4 due to systematic absence conditions. In layman's terms, it seems that the intercalation broke the symmetry element (or elements), which caused the original extinction of some of the diffracted beams.

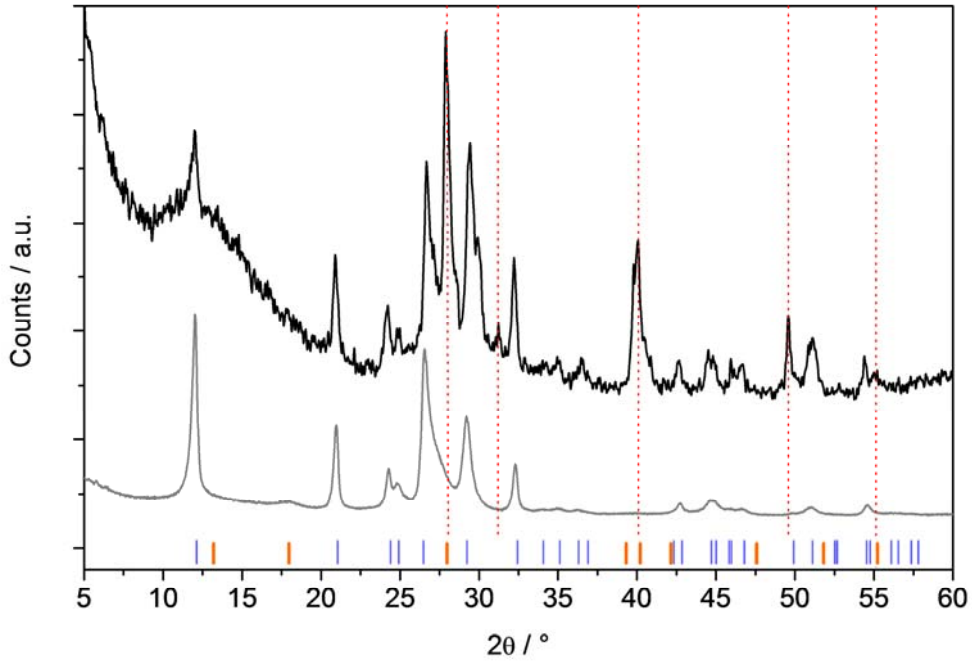

Figure 32. Comparison of PXRD patterns of pure *g*-C_3N_4 as obtained from the condensation in LiCl/KCl salt melt (grey) and its potassium intercalation compound, $K(C_6N_8)_3$ (black). New reflections due to potassium intercalation are marked in red.

The symmetry element in this particular case is a c-glide plane perpendicular to the b-axis (*l* = 2n) such as present for the *Pmc*2_1 (C_{2v}) point group. The equivalent positions of this symmetry operation are relatively easy to depict in standard notation for a primitive cell (c.f. Figure 33.).

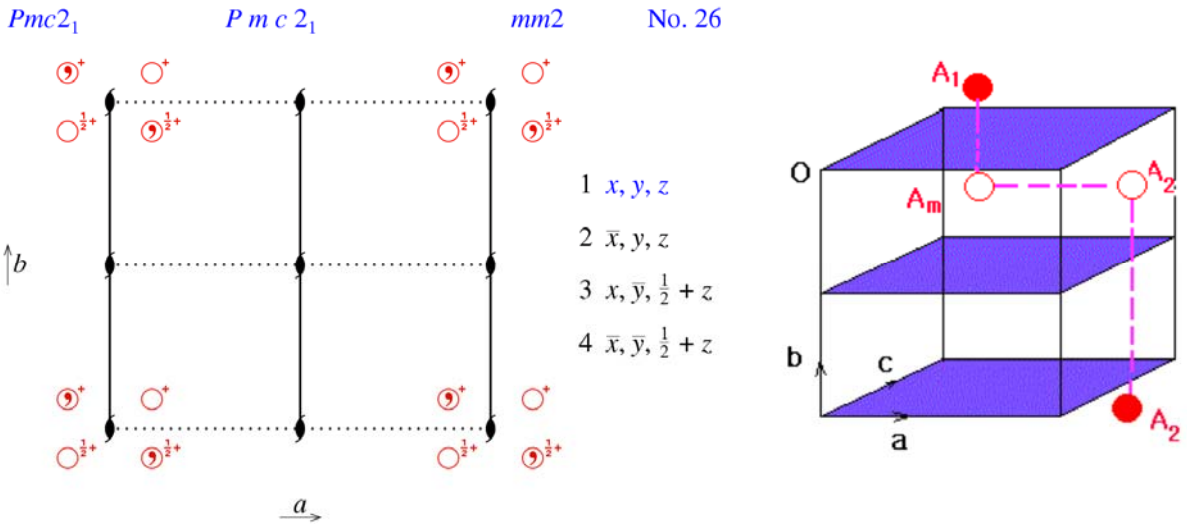

Figure 33. Visualisation of the effect of a c-glide plane perpendicular to the b-axis (*l* = 2n) for the *Pmc*2_1 (C_{2v}) point group.

In case of a hexagonal unit-cell the standard notation is not very helpful but gets rather cluttered. In the following examples the in-plane cavities between the heptazine units were marked with spheres of varying colours, in order to elucidate the effect of a c-glide plane perpendicular to the b-axis.

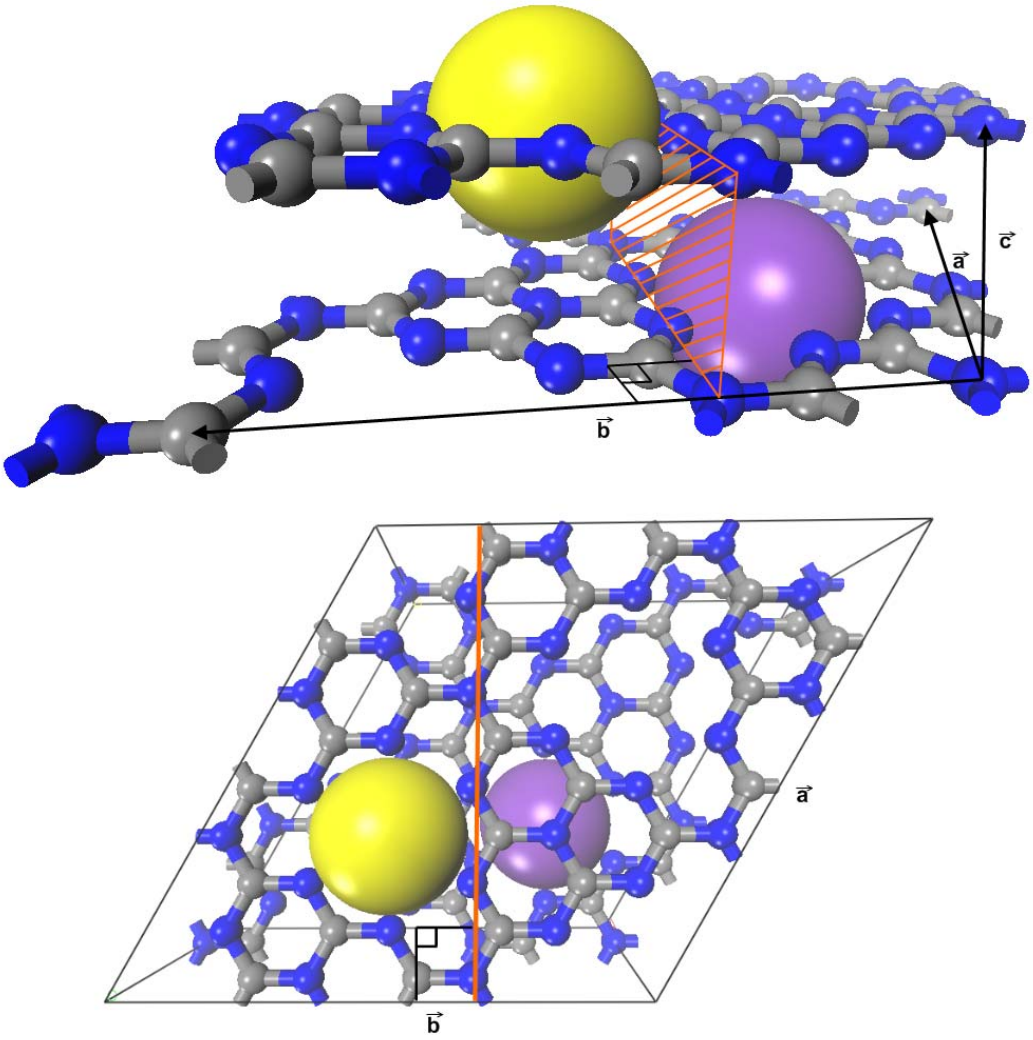

Figure 34. Effect of a c-glide plane perpendicular to the b-axis (l = 2n) in g-C_3N_4 (marked in orange).

Now, let us dwell on the meaning of Figure 34 for a moment. If the intercalation of potassium broke the symmetry element of the graphitic carbon nitride material (denoted above as the orange plane parallel to the c-axis and perpendicular to the b-axis), then the positions (denoted with yellow and purple) will no longer be equivalent – in other words, the intercalated potassium cannot occupy both positions along the b-axis. The collapse of

the symmetry element “c-glide plane perpendicular to the b-axis” accounts for the reappearance of the peaks at 27.87°, 40.06°, 49.59° and 55.14° in terms of 2θ.

Peaks at 2θ 13.44° and 39.12° do not appear though – this particular symmetry element must hence be preserved in the symmetry of the intercalation compound. The symmetry element in question is a c-glide plane perpendicular to the (a+b)-axis (*l* =2n). If we construct the corresponding crystal lattice we find the following:

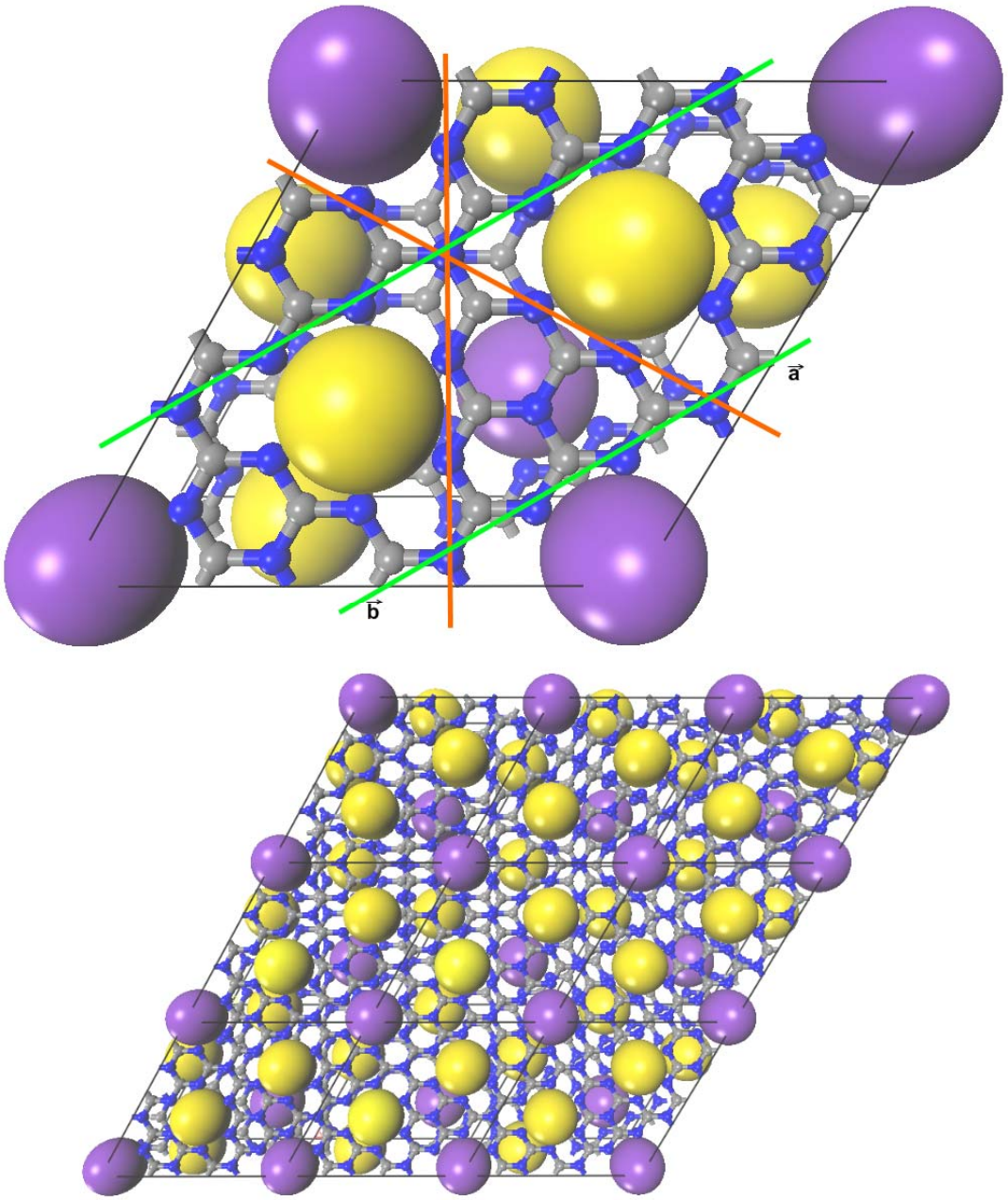

Figure 35. Effect of a c-glide plane perpendicular to the a- and b-axis (*l* = 2n) (marked in orange) and of a c-glide plane perpendicular to the (a+b)-axis (marked in green) in *g*-C_3N_4.

We do not know where and how the potassium is incorporated in the material, yet. This missing piece of information, however, does not matter for the purpose of a purely phenomenological examination of the effect of symmetry operations, since it will hold true for all potential coordination sites in the material. The choice to visualise the cavities is not completely arbitrary, though. Metal-organic compounds including many crown ethers (and azo-equivalents) are known in which a potassium ion is surrounded by six or eight coordination sites. In this particular case a six-fold coordination site would be opened up by the nitrogen atoms of three neighbouring heptazine units, as shown below:

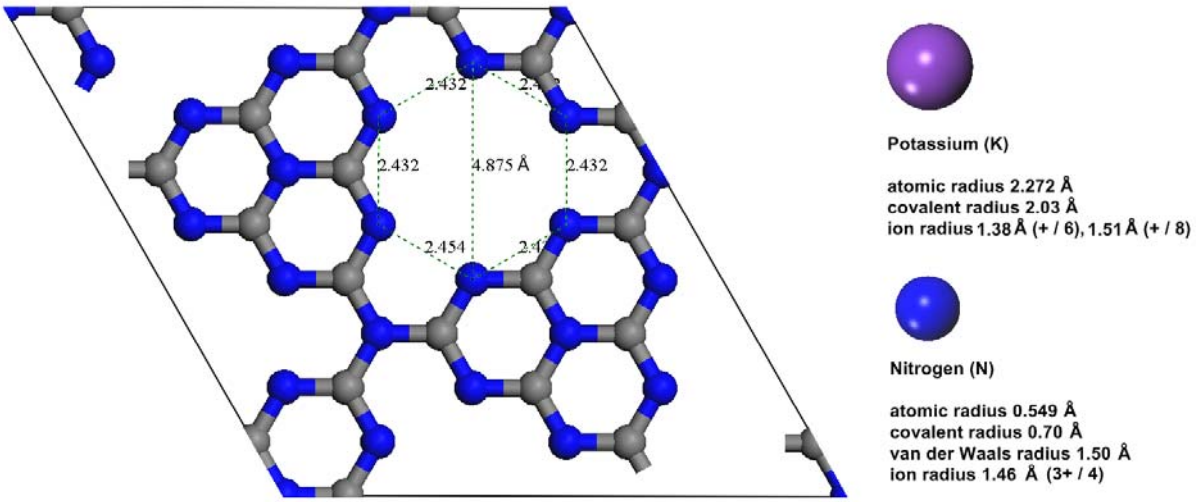

Figure 36. Size comparison of the in-plane cavity in *g*-C_3N_4 and the intercalated potassium.

Note though, that the diameter of the cavity is sufficiently large for an in-plane incorporation of a potassium atom. Taking the spatial requirement of the nitrogen lone-pairs into account, we are left with 2 Å to accommodate a species which has an uncharged, covalent diameter of 4.06 Å and an ionic diameter of 2.76 Å. This makes a shift of the potassium into the inter-lamellar space a very likely possibility of accommodation. For now we will content ourselves with the general occurrence of the potassium throughout the carbon nitride framework. This in turn can be viewed in analogy to the graphite system, KC_8. Likewise, potassium incorporated in the carbon nitride framework observes a nearest neighbour distance of one structural repeat (c.f. Figure 37).

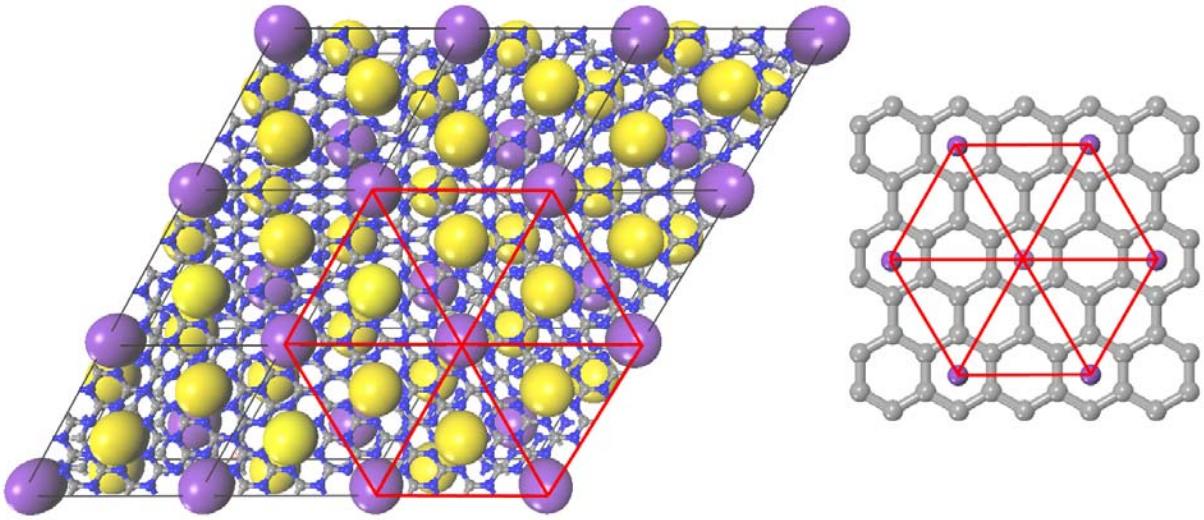

Figure 37. Proposed structure of $K(C_6N_8)_3$ and its graphite equivalent, KC_8. Equivalent sites in $K(C_6N_8)_3$ are marked in either purple or yellow.

Electron microscopy reveals that the exterior crystal morphology of the carbon nitride material does not change significantly upon conversion with metallic potassium. The hexagonal prisms of the order of magnitude of 200 nm known already from chapter 3 as graphitic carbon nitride are the sole species visible in surface and transmission electron microscopy. Figure 38 shows a SAED picture which reveals four diffraction spots marked in on a ring which corresponds to a d-spacing of 0.318 nm. Following the model we suggested in Figure 37, the four spots are identified in terms of (*h k l*) as the (2 0 -1), (0 2 -1), (2 -2 -1) and their inverse reflections. These reflections in turn constitute the x-ray diffraction peak observed at $2\theta = 27.87°$.

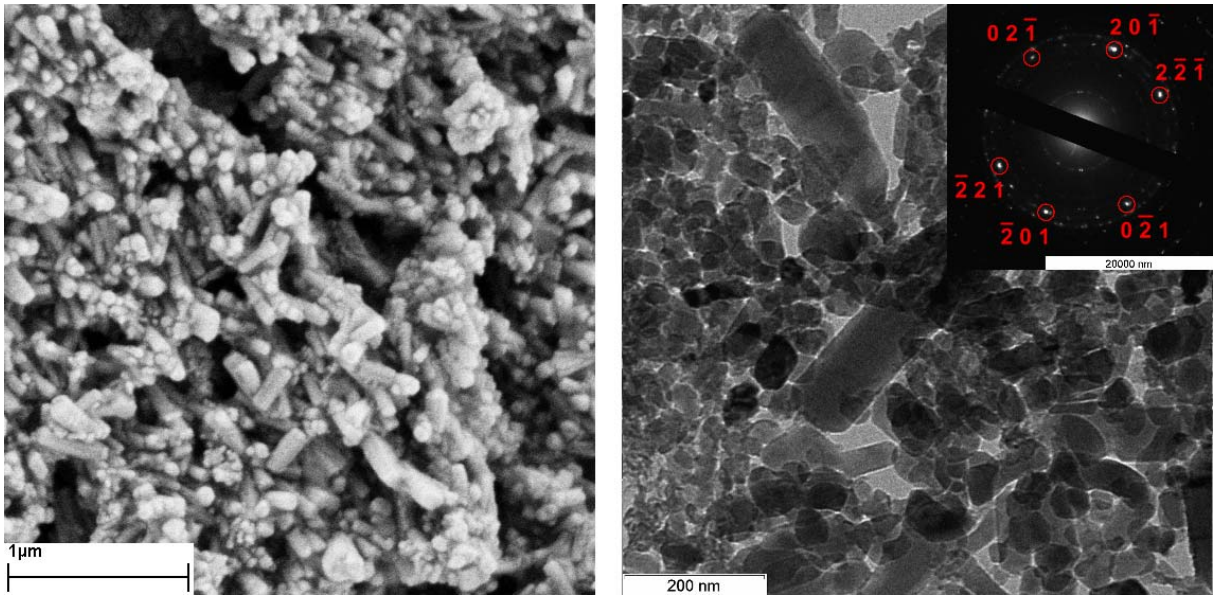

Figure 38. SEM (left) and TEM (right) pictures of $K(C_6N_8)_3$ as obtained after the intercalation reaction. The inset in the TEM picture shows the three reflections (2 0 -1), (0 2 -1), (2 -2 -1) and their inverse reflections constituting the x-ray diffraction peak observed at $2\theta = 27.87°$.

These findings corroborate our proposed structural model, and we can term the dominant species of the observed intercalation compound with $K(C_6N_8)_3$ according to its stoichiometric ratio.

Following the lead of Viculis *et al.* that potassium intercalated graphite can be exfoliated using aqueous solvents, the $K(C_6N_8)_3$ intercalation compound is subjected to a 50 vol. % EtOH/water solution. Upon sonification $K(C_6N_8)_3$ (5 mg) forms a stable solution in EtOH/water (2 mL) – an unprecedented property, since there exists no known solvent for the non-intercalated, pure graphitic carbon nitride. The resulting solution is basic because of the formation of potassium ethoxide and is strongly fluorescent.

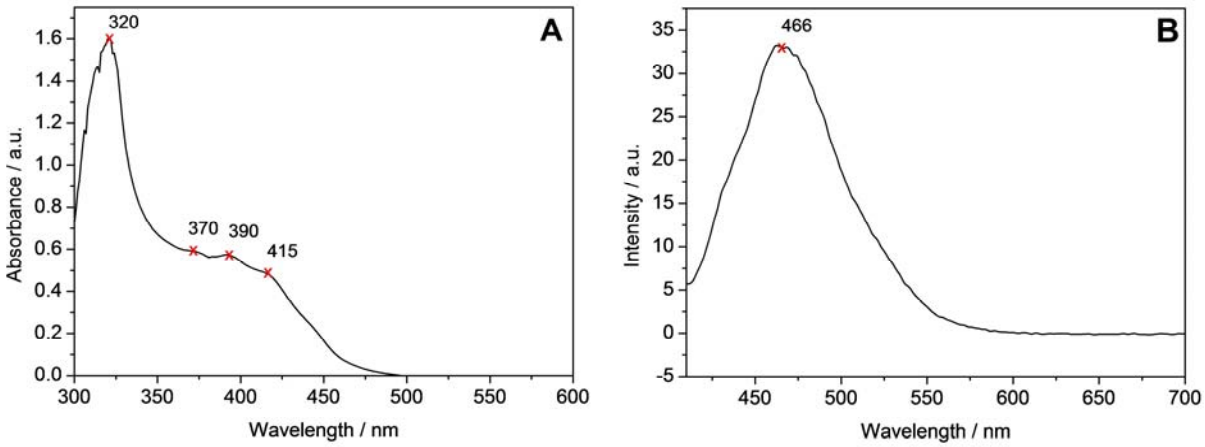

Figure 39. (A) Ultraviolet-visible transmission spectrum and **(B)** fluorescence emission spectrum of the $K(C_6N_8)_3$ intercalation compound in 50 vol. % EtOH/water. Fluorescence was excited at 390 nm with 1% attenuation.

Figure 39 shows the UV-Vis and fluorescence spectra of $K(C_6N_8)_3$ in EtOH/water. It is somewhat challenging to put this data into context of non-intercalated *g*-C_3N_4, since the UV-Vis spectra of the solid material can only be obtained in diffuse reflectance mode and only for the more brightly coloured (i.e. less condensed) samples. A nice study on the UV-Vis properties of a type of photoactive, polymeric carbon nitride was published in an aforementioned paper by Wang *et al.*[40] Therein, cyanamide was heated to temperatures between 673 and 873 K yielding a set of condensation products presented above in Figure 15 ranging from melem to a cross-linked, stacked poly-melon. The paper suggests that the absorption edge moves towards higher wavelengths as the condensation is driven to completion by higher temperatures. More complete condensation is believed to be associated with a smaller bandgap between the conduction and the valence band of the carbon nitride material. The bandgap of the carbon nitride obtained at 600 °C is estimated to be 2.7 eV from its ultraviolet–visible spectrum, showing an intrinsic semiconductor-like absorption in the blue region of the visible spectrum, just as the aqueous solution of $K(C_6N_8)_3$.

The inset in Figure 40 shows the effect of added conjugation in naphthalene, anthracene and tetracene, which causes bathochromic shifts of these absorption bands. If this well established phenomenon is any indicator, the UV-Vis active species in the aqueous solution of $K(C_6N_8)_3$ must have an even more extended aromatic system, than any of the

species obtained via the bulk condensation pathway. Sheet of perfectly condensed, graphitic carbon nitride could be considered as such an extended aromatic system, and it seems that they remain intact in the solution.

The absorbance maximum at 320 nm in the UV-Vis spectrum of solubilised $K(C_6N_8)_3$ has two potential explanations. For one it could simply be the adsorption of the constituent heptazine units in each individual, solubilised sheet; a signal which is masked by bulk effects (i.e. excitation of multiple states) for the bulk-condensed samples. Another explanation would be that this near-Vis absorption is caused by charge transfer effects, which might be expected for the product of a reductive intercalation process. In analogy to the purple-coloured charge-transfer complex formed by iodine and starch, the heptazine framework could act as the electron acceptor.

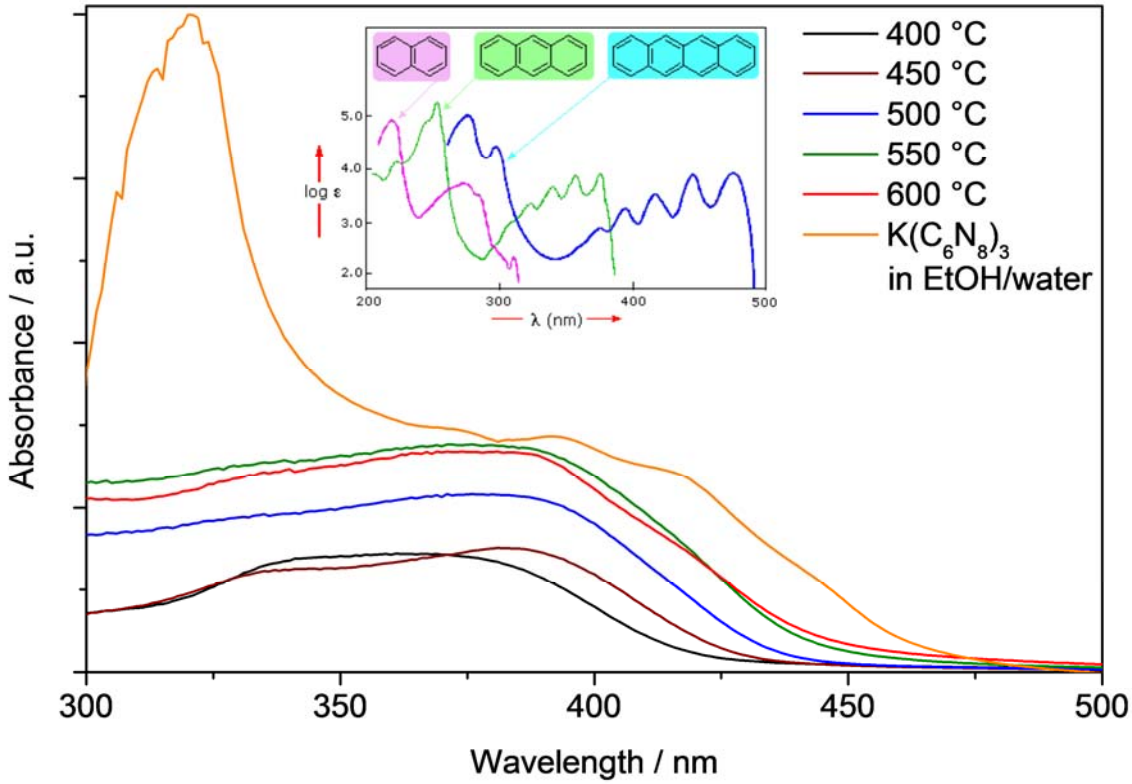

Figure 40. Comparison of the ultraviolet-visible transmission spectra of $K(C_6N_8)_3$ in EtOH/water (orange) with the bulk condensation products of dicyandiamide terminated at temperatures ranging from 400 to 600 °C.

The solution of $K(C_6N_8)_3$ in EtOH/water was finally spread on carbon grids and imaged with a Carl Zeiss Omega 912 transmission electron microscope (TEM). Typical

images of the carbon nitride scrolls (or bundles of scrolls) are shown in Figure 41, A through C, while Figure 41, D through F shows the carbon nanoscrolls and bundles obtained in an analogous way from graphite by Viculis *et al.* as described previously. Figure 41, A shows isolated bundles of scrolled carbon nitride sheets all approximately 1400 nm in length and 150 nm broad, most likely consisting of several rolled up carbon nitride layers. Figure 41, B shows a bundled mass of graphitic carbon nitride sheets representative of the bulk of the scrolled graphite. Figure 41, C is particularly interesting as it shows electron beam damage done to the carbon nitride sheets. Viculis *et al.* observed that their nanoscrolls oxidise in air to carbon dioxide at 450 °C; far lower than pristine graphite, which is stable in air up to 650°C. This lowered oxidation resistance and thermal stability was attributed to reduced van der Waals interactions compared to the bulk material; an argument which holds true for the graphitic carbon nitride system as well. It should be noted that the origin and nature of the globuli (diameter of approx. 115 nm) seen in Figure 41, A through C is not determined yet.

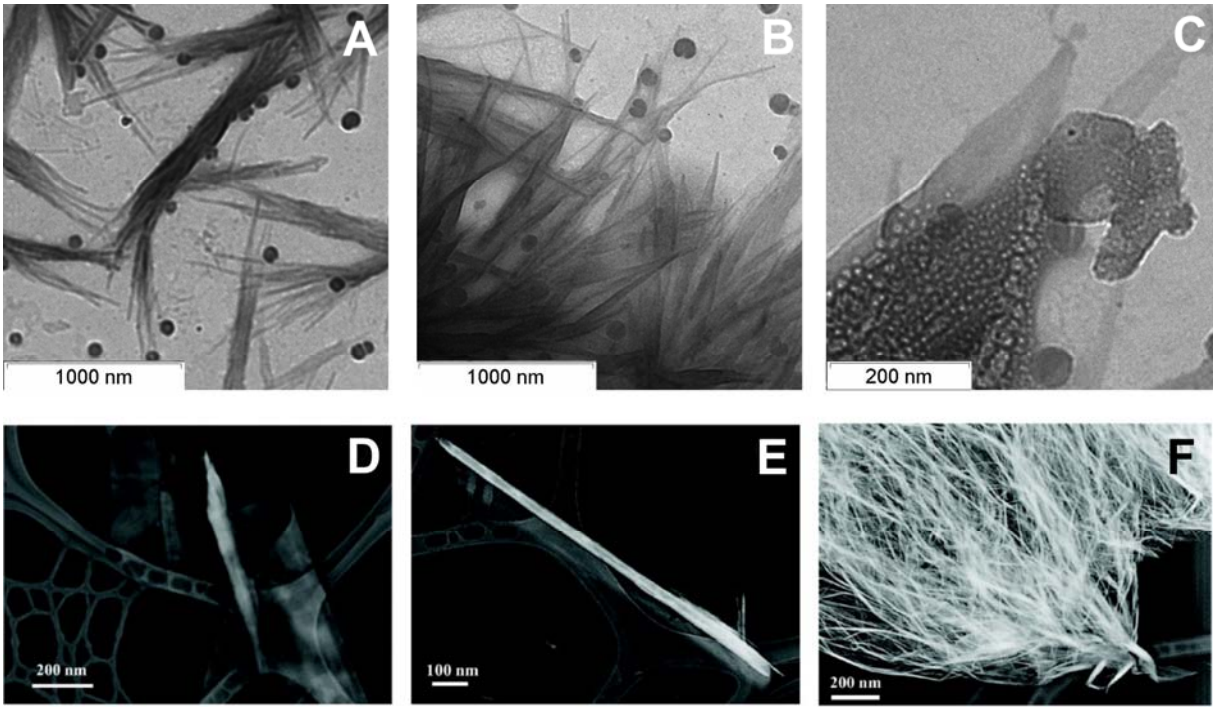

Figure 41. TEM images of **(A)** isolated bundles of graphitic carbon nitride, **(B)** mass of graphitic carbon nitride bundles, and **(C)** electron beam damage to a selected area of graphitic carbon nitride bundles. Below taken from the paper by Viculis *et al.*[71] for comparison **(D)** a thin plate of graphitic sheets in the process of scrolling, **(E)** an isolated carbon nanoscroll with open ends, and **(F)** a mass of scrolled material, representative of the bulk of the sample.

These observations lead us to the final conclusion. A conversion of potassium metal with graphitic carbon nitride, which was obtained according to the procedure of Bojdys *et al.*[72] yields an intercalation compound analogous to known graphitic systems. The intercalated potassium occupies interlamellar space between heptazine units and the cavities spanned by them in an alternating fashion, and follows a nearest-neighbour distance of one structural repeat. An intercalation compound of such symmetry has the corresponding molecular formula of $K(C_6N_8)_3$.

This is already a surprising find, since it extends known graphite chemistry to a novel class of materials, the carbon nitrides. A piece of more extraordinary graphite chemistry was performed on $K(C_6N_8)_3$ in analogy to KC_8, showing that the treatment of $K(C_6N_8)_3$ with aqueous solvents induces exfoliation of the graphitic carbon nitride sheets, which remain intact in the solution.

6 Heptazine-based frameworks

6.1 Introduction to rationally designed frameworks

We have seen previously in chapter 3 that the linking of organic molecules by means of covalent bonds yields crystals of discrete 2D and 3D morphology – a truly underdeveloped field of chemistry. Progress in this area has been impeded by longstanding practical and conceptual challenges, and we have elaborated on some of them. Foremost, unlike molecular or 1D systems, the insolubility of 2D and 3D structures precludes the use of step-wise synthesis and makes their isolation in crystalline form very difficult. Second, the number of possible structures that may result from linking specific building-unit geometries into 2D or 3D extended structures is essentially infinite and complicates their synthesis by design.

The realisation of a concept how to link molecular systems into a 2D and 3D framework was demonstrated by Yaghi and co-workers recently.[73, 74] Both publications make use of the formal dehydration mechanism of boronic acid to give the auto-condensation product or the condensation product with a suitable linker. Linker geometries vary between discoid and tetrahedral inducing 2D and 3D linking, respectively. An example of such a discoid system is given below:

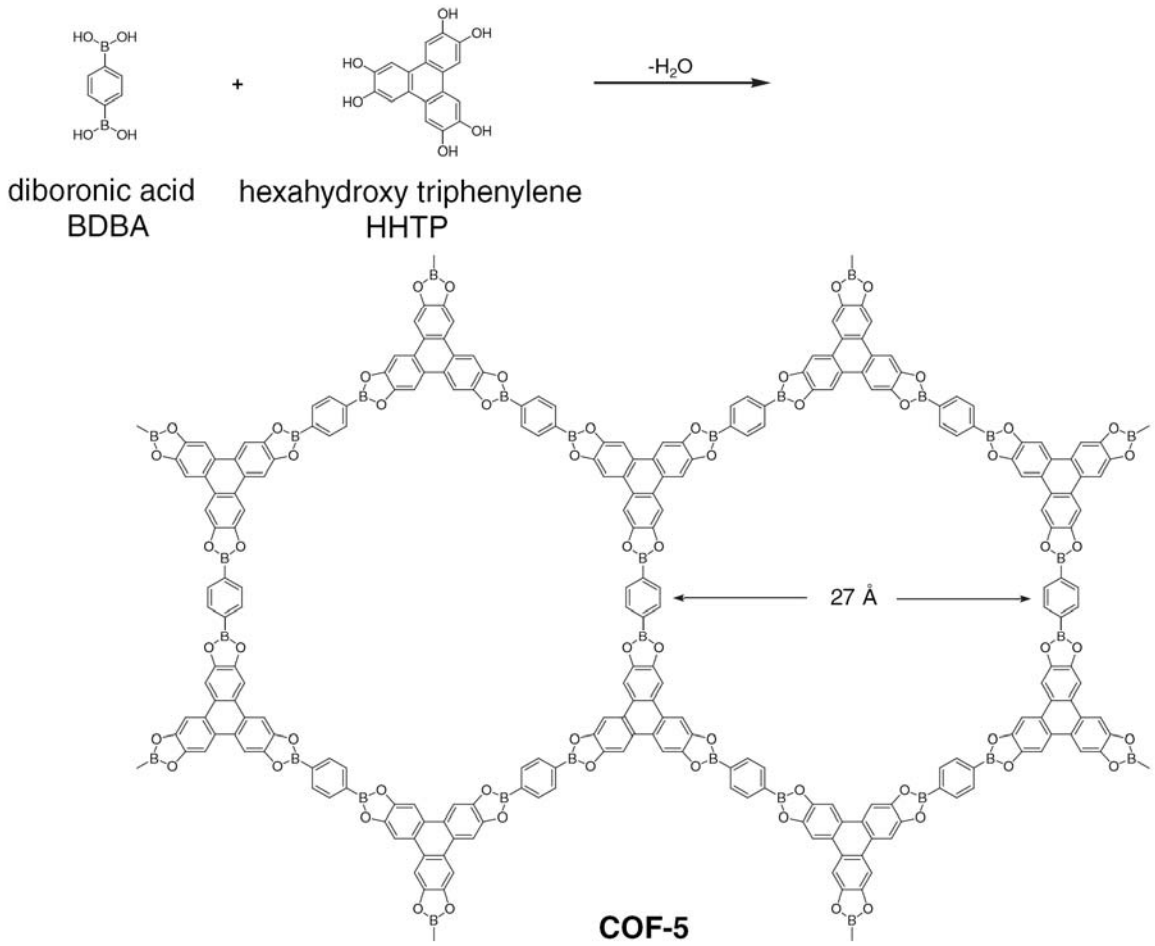

Figure 42. Condensation reaction of diboronic acid (BDBA) and hexahydroxy triphenylene (HHTP) to give extended COF-5 as shown by Yaghi et al.[73]

Let us examine the reasons why the ionothermal synthesis of graphitic carbon nitride based on condensation of dicyandiamide was successful. We have addressed the first challenge employing an ionogenic salt-cast as a rather unconventional solvent. Likewise we have seen in chapter 4 that the choice of the salt melt can have a big impact on crystallisation behaviour. Secondly, the lucky choice of reactants and their mechanistic peculiarities allowed for a condensation under (apparently) reversible conditions. In this chapter we shall see, how the proposed reaction mechanism seen in Figure 16 can be generalised and applied to a wider array of organic building blocks.

Taking the condensation mechanism from Figure 16, suppose we substitute one ammonia equivalent on each reacting species by an arbitrary group, R, then the condensation pathway turns out to be:

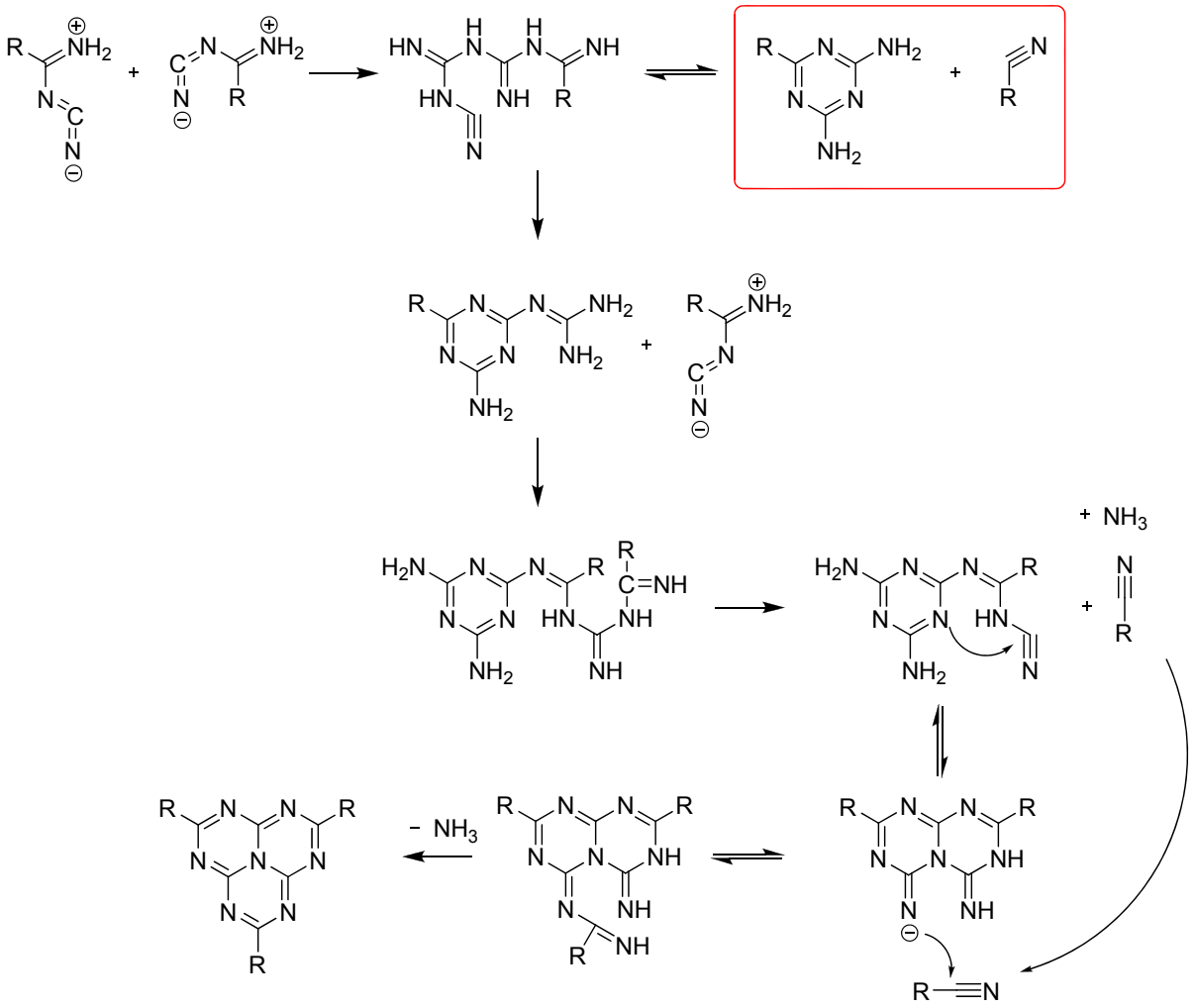

Figure 43. Proposed reaction mechanism for the condensation of a tri-substituted heptazine unit analogous to the formation of Liebig's melem.

Note that the formation of the heptazine unit proceeds under formal deamination of the partaking species, and under ideal conditions no excess of reactive molecules which would be available for side-reactions is created. Note further that the condensation process requires nothing more but an R-triazine and an R-carbonitrile equivalent in one-to-one molar ratio. The main difference between the substituted and non-substituted condensation mechanism from Figure 16 is that the formation of a melam equivalent is not a formal requirement; it is still an option, though, when the condensation of two R-triazine groups under deamination is considered. A self-propagating condensation mechanism would employ one, single molecular precursor which contains both the triazine and the carbonitrile functionality at its termini (c.f. Figure 43, red inset). While the condensation reaction of grahitic carbon nitride requires high temperatures to promote the deamination of the tri-*s*-heptazine unit, the condensation of a heptazine based framework could be

completed at lower temperatures, since no small molecules need to be driven out of the system once the heptazine unit is formed. The particular threefold symmetry and planar arrangement of the tri-substituted heptazine unit would in theory allow the synthesis of planar, 2D frameworks which would be expected to stack in a graphitic or similar fashion. The design of the corresponding molecular precursors is presented in the following section.

6.2 Synthesis of the triazine precursor materials

The compounds used are bi-substituted aromatics, preferably with two cyano-groups in *para*-postions. In the case that a dicyano-compound is not readily available, a suitable compound is synthesised from its dibromo precursor. Displacement of the bromide by cyanide ion, using the copper (I) salt as the nucleophile, yields the stable primary nitrile, as shown below. Cu(I) is removed from the system via complexation with TMEDA, and the so obtained dicyano compound is extracted with dichloromethane.

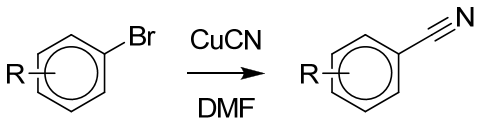

Figure 44. Synthetic scheme for the displacement of the bromide by cyanide ion, using the copper (I) salt as the nucleophile.

One of the nitriles can then be converted into a triazine group (an ammeline derivative) with dicyandiamide (DCDA) in a base catalysed reaction. The formation of the stable, aromatic triazine unit drives the reaction to completion. Mono-substituted aromatics readily precipitate from boiling isopropanol after short reaction times.

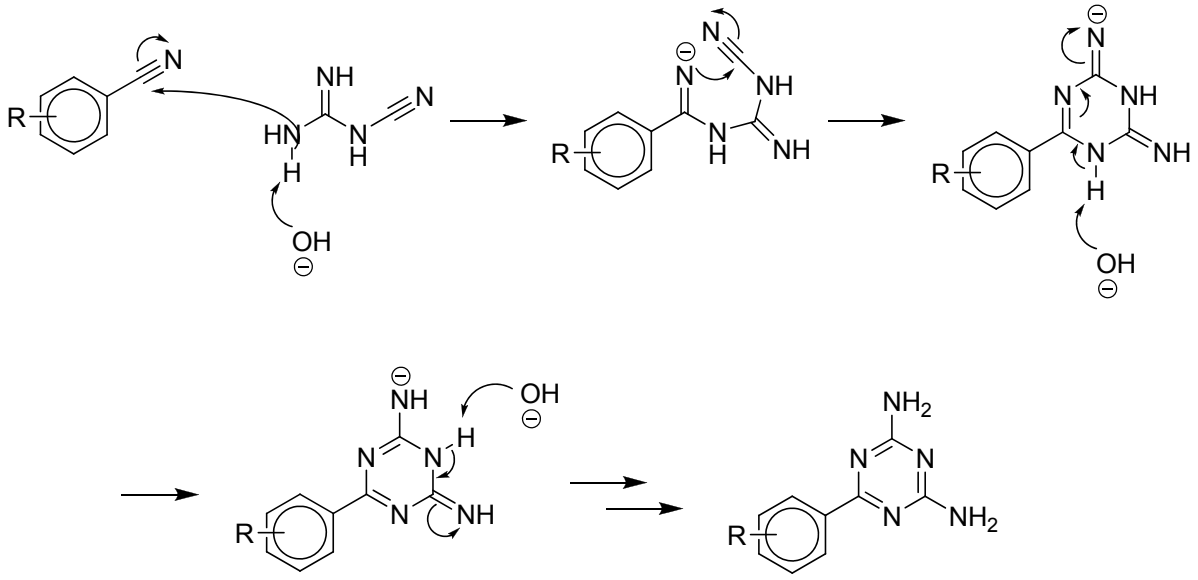

Figure 45. Synthetic scheme for the conversion of a nitrile into a triazine group with dicyandiamide (DCDA) in a base catalysed reaction.

Now as we see from Figure 43 any molecular building-block synthesised along the lines presented above will contain a triazine and a carbonitride equivalent and will hence be a suitable candidate for autocondensation.

6.3 From ArCNTz to HBF-1 – ionothermal synthesis and characterisation

The molecular precursor with the cumbersome name 1-cyano, 4-(2,4-diamino-1,3,5-triazino)benzene (in short ArCNTz) was prepared according to the procedure outlined in chapter 6.2 (a detailed procedure is given in the appendix, section 8.3). ArCNTz (0.5 g, 2.36 mmol) was thoroughly grounded together with a mixture of lithium bromide and potassium bromide (10 g, 52:48 wt %) as the solvent of choice. The reaction mixture was heated at 40 K min^{-1} under inert atmosphere and kept at terminal temperatures ranging between 380 and 450 °C for up to 48 h. Excess salt was dissolved in boiling, distilled water and removed through repeated washing. The product was thoroughly dried at 200 °C/10^{-5} torr to yield the heptazine based framework, HBF-1 (0.2 g, 0.352 mmol, 45% yield) as a black-brown powder. The best yield was achieved at 430 °C and 26 h of reaction time.

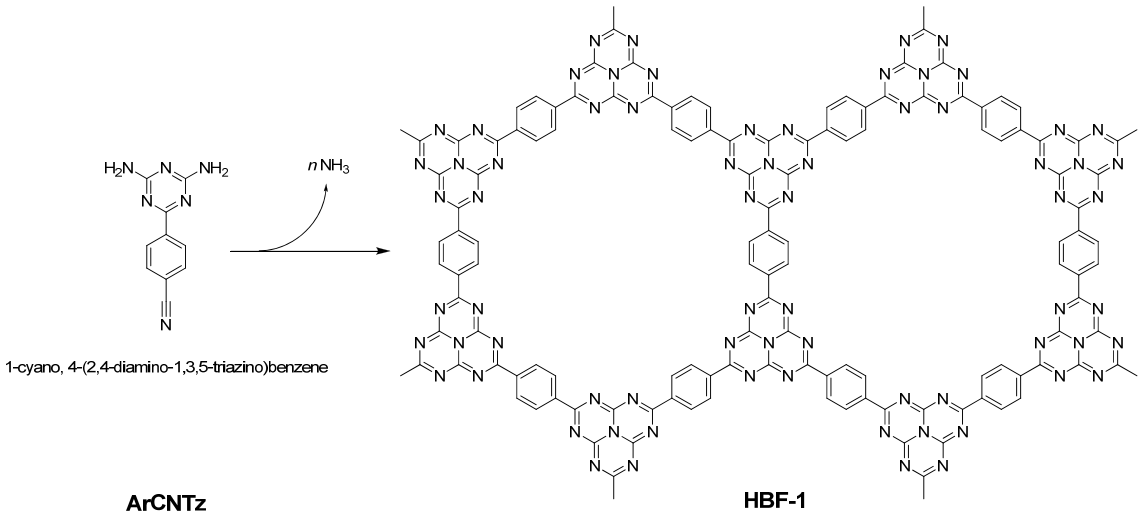

Figure 46. Condensation reaction of 1-cyano, 4-(2,4-diamino-1,3,5-triazino)benzene (ArCNTz) to give the extended heptazine based framework (HBF-1).

The composition of a sample of HBF-1, according to elemental microanalysis, was as follows: 57.1% C, 33.2% N, and 2.63% H, with the difference of 7.1% presumably due to chelated salt and adsorbed water. The N/C ratio of 0.497 for the obtained product is strikingly close to the ideal ratio of 0.467 for a perfect structure. The dried HBF-1 material was found to have the following molecular formula: $C_{30.0}N_{14.9}H_{16.47}$, which corresponds to the expected formula of an extensively condensed material (c.f. Figure 47).

A comparison of the vibrational spectra of the different stages of condensation of ArCNTz in lithium bromide and potassium bromide melt is shown in Figure 47, (**b**) through (**e**) and of the starting material in Figure 47, (**a**). Some areas of interest are marked out as a guide for the eye. Note that broad ammonia bands at around 3200 cm^{-1} indicative of secondary and primary amines (and their intermolecular hydrogen bonding) next to disappear for the high temperature condensation product. Since aromatic C-H bonds are an integral part of HBF-1 some remaining bands in this region are expected. The carbonitrile band around 2250 cm^{-1} also gradually disappears as the condensation is driven to completion. The aromatic C-C band at 1600 cm^{-1} remains visible throughout the process, which corroborates the results from elemental microanalysis, that no aromatic groups are eliminated. The characteristic breathing mode of the triazine and heptazine units at 800 cm^{-1} is also preserved throughout the process. Put into perspective with the results of the

elemental microanalysis, it is safe to assume that the material we are looking at consist of condensed domains at least on the nanometre scale with few terminal groups or defects.

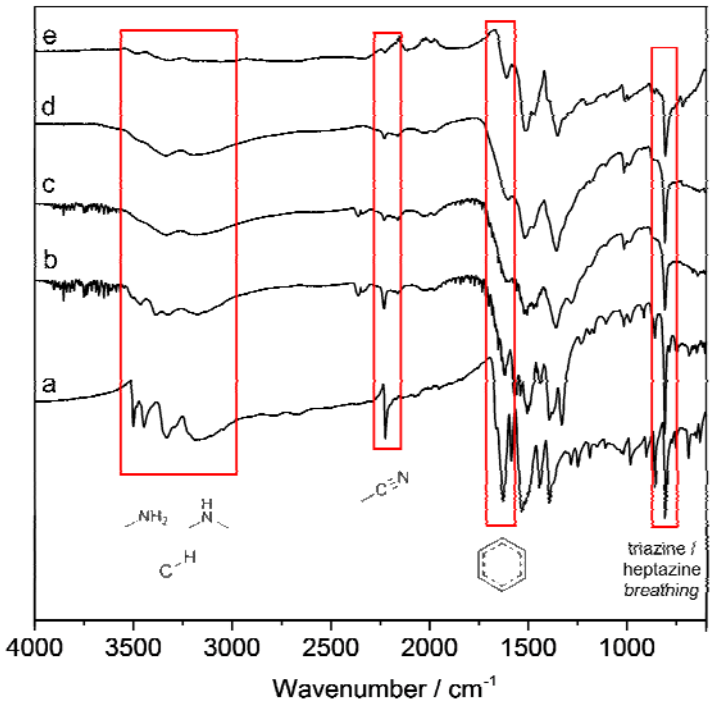

Figure 47. FTIR spectra of (**a**) the ArCNTz monomer, and the condensation products of ArCNTz in LiBr/KBr melt at (**b**) 400 °C (48 h), (**c**) 410 °C (48 h), (**d**) 420 °C (48h) and (**e**) 430 (48 h).

In a reference experiment ArCNTz was subjected to the same heating procedure but without any addition of salt, i.e. a bulk condensation was performed analogous to the graphitic carbon nitride system. The composition of these condensation products was according to elemental microanalysis 60.0% C, 31.1% N, and 3.83% H which corresponds to the molecular formula: $C_{18.0}N_{8.0}H_{13.66}$. The excess hydrogen content can be attributed to secondary and primary amino groups as seen in the vibrational spectrum of the material in Figure 49, A. The powder XRD pattern of the bulk condensation material shows no pronounced structural components except for a very broad peak at 26.1° in terms of 2θ which is known from systems like turbostatic graphite, bulk carbon nitride and overall from largely amorphous but stiff polymers (Figure 49, B). Keeping these results in mind, it is more likely that the bulk condensation proceeds as shown in Figure 48 yielding an aryl-bridged triazine polymer either in linear conformation or as a branched network with many

unreacted ammonia groups of the composition $C_{18.0}N_{8.0}H_{12}$ – a perfect match the results of our elemental microanalysis. The resulting product would then be a linear polymer, which could quite likely pack through π-π interactions giving rise to the aforementioned diffraction peak at 26.1° but would be far from the crystalline, covalently linked, extended framework we set out to design. Again, as previously described in chapter 3 for the graphitic carbon nitride, the formation of a condensed framework is hindered by kinetics.

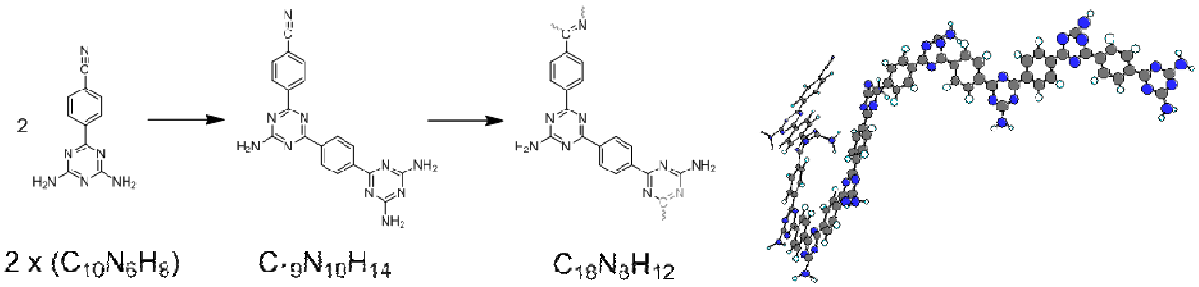

Figure 48. General bulk condensation scheme of ArCNTz.

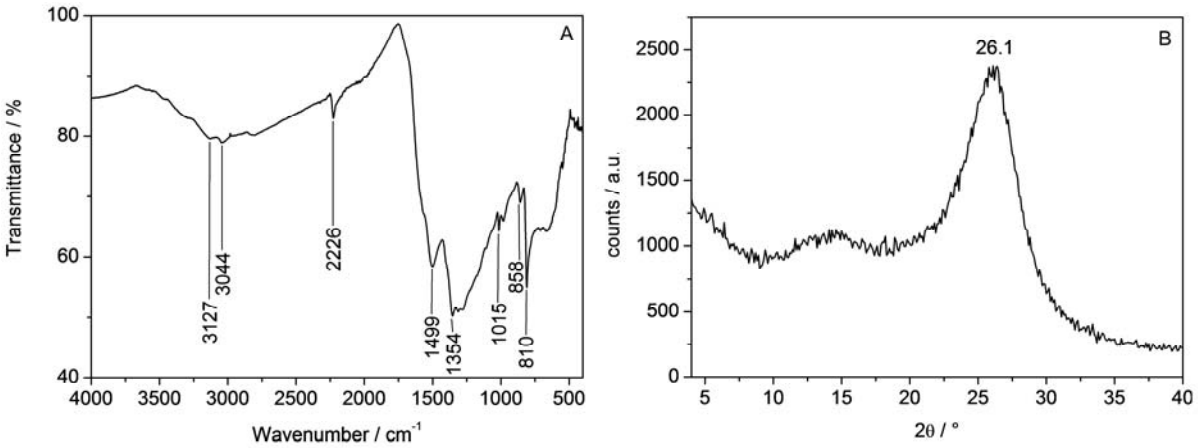

Figure 49. Vibrational spectrum **(A)** and PXRD pattern **(B)** of the bulk condensation product of ArCNTz obtained at 430 °C.

To assess the crystal structure of HBF-1 the powder XRD patterns of two condensation products were chosen, namely the most thoroughly condensed products obtained at 430 and 440 °C as seen in Figure 50, C and A respectively. Both patterns were indexed using *ab initio* calculations and a structureless LeBail fitting procedure. The peak positions of both condensation products gave an excellent correlation with the calculated Bragg peak positions of a hexagonal unit cell of the space group P6 (No. 191) with the parameters of $a = b = 18.248$ Å and $c = 11.939$ Å. Strangely though, the best figure of merit

during the indexing procedure was attributed to a unit cell of not-all intuitive dimensions and a very specific set of symmetry operations, namely the monoclinic space group C2 (No. 5) with lattice parameters *a* = 18.248 Å, *b* = 31.606 Å and *c* = 11.939 Å ($\alpha = \beta = \gamma = 90°$) (c.f. Figure 50, B). In fact this stringent set of symmetry conditions gave a figure of merit (FOM) two fold higher than that of the hexagonal system (FOM of 31 and 15, respectively)

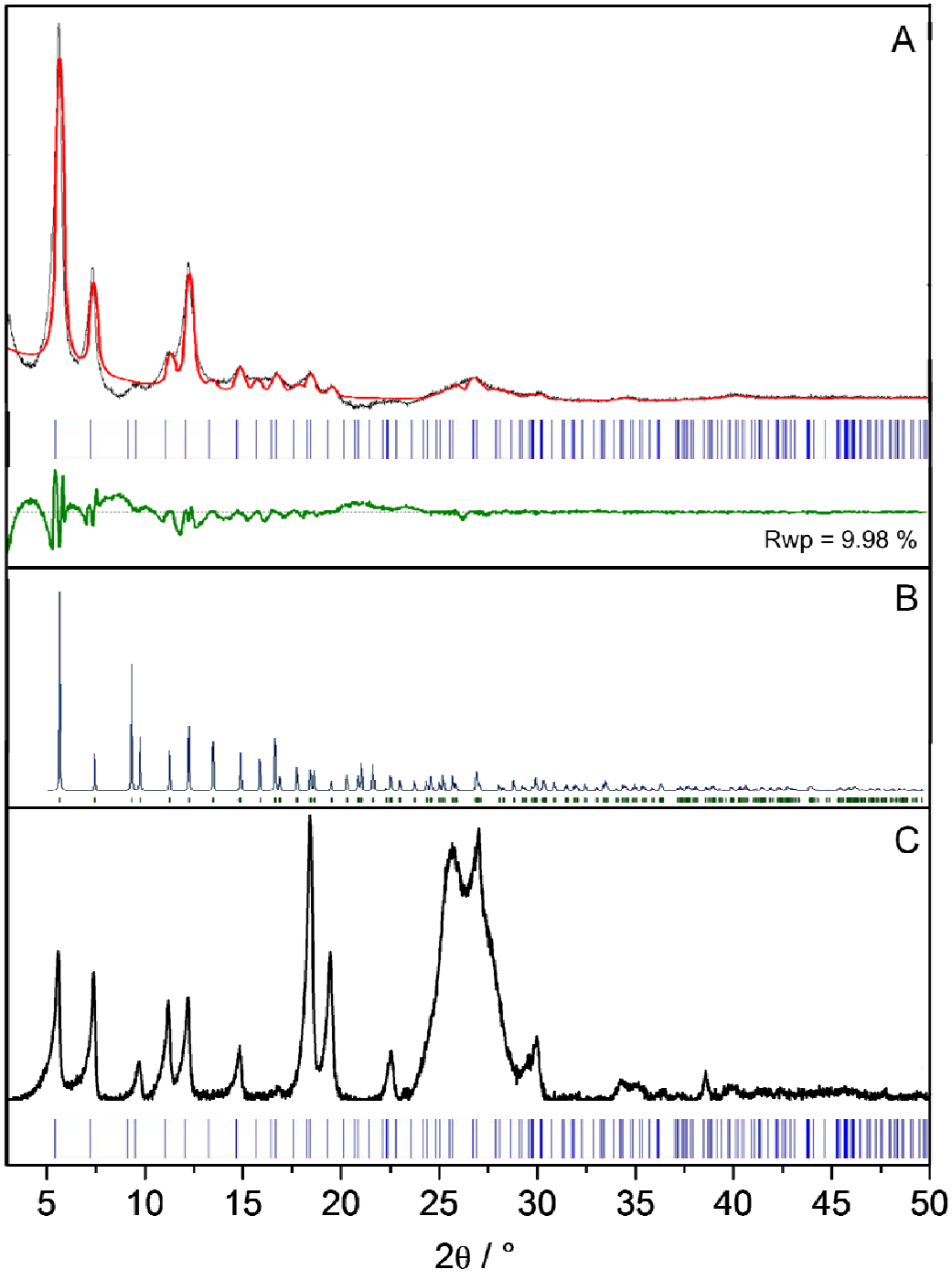

Figure 50. Physical characterisation of HBF-1 as obtained from the condensation of ArCNTz in the LiBr/KBr salt melt at 440 °C **(A)** and 430 °C **(C)** with the calculated pattern **(B)**.

Structureless LeBail fit performed on the XRD pattern of HBF-1 **(A)**, the refined profile (red), the difference plot (green) and Bragg peak positions (blue).

The structureless fits for both unit cells give good correlations of peak positions however the relative and absolute peak intensities are fair at best. Some thought should be invested, as to how these unit cells should be populated in a chemically reasonable fashion. Figure 51 shows a layer of the ideal HBF-1 superimposed on a hexagonal grid with parameters $a = b = 18.248$ Å ($\gamma = 120°$). The hexagonal unit cell is devised in such a way, that each corner of one rhombus is occupied by a hepatazine unit. A cavity of 14.2 Å is spanned in one half of the rhombus, while the other is occupied by another heptazine unit. The distance between the aryl-bridged heptazines in such an arrangement would then necessarily be 10.6 Å. A density functional theory calculation for a similar unit – namely a fully aromatic, aryl-bridged heptazine and a triazine unit – gave a next to perfect match for this distance with 10.9 Å (c.f. Figure 51). In this perfect bonding pattern we can even retrieve the ominous monoclinic C2 lattice with $a = 18.248$ Å, $b = 31.606$ Å ($\alpha = \beta = 90°$), which is also cornered by heptazine units but which encompasses the equivalent of two cavities and can be seen in Figure 51 superimposed in dashed orange lines. Hence, from a chemist's point of view the in-plane bonding pattern makes sense – so how about the rigorous scrutiny of a scattering expert? Table 1 shows an overview of all observed peaks and their assignment in term of (*h k l*)-values for each corresponding unit cell, and luckily we see that there is no ambiguity and that all observed peaks can be assigned. As an example, both model unit cells assign the first low-angle peak to an in-plane reflection. In the light of previous elemental and functional groups analyses this reflection study corroborates that each sheet of HBF-1 consists of aryl-linked, co-planar heptazine units.

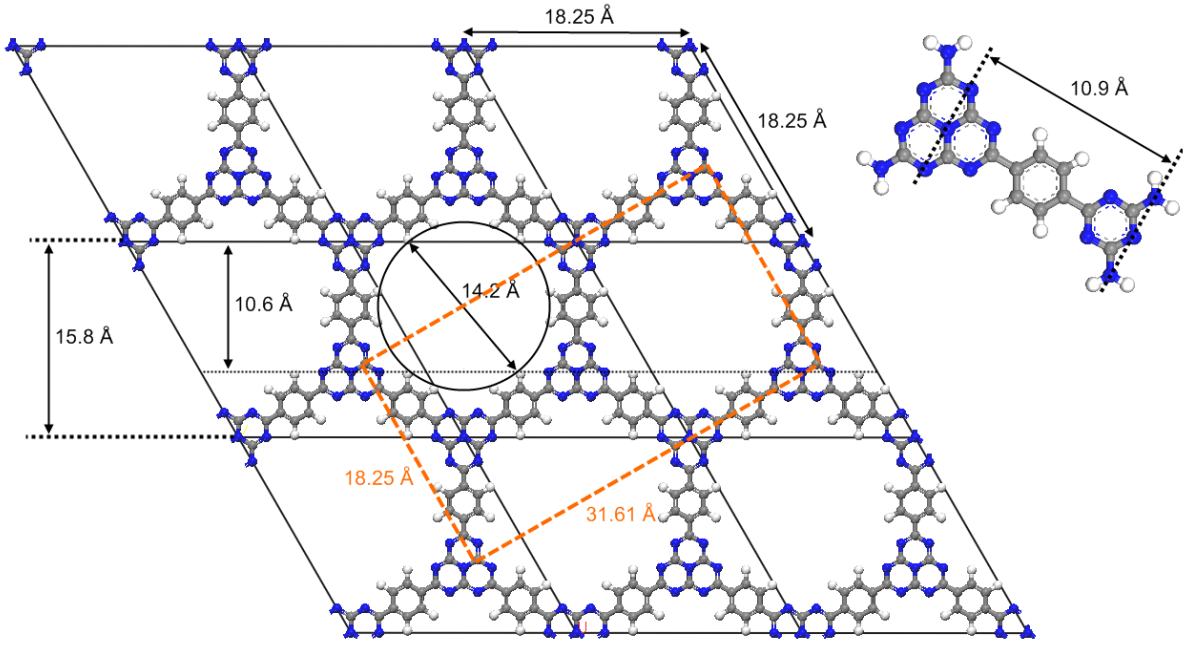

Figure 51. Proposed structural model for the in-plane order of HBF-1. The monoclinic C2 lattice (orange) is superimposed on the hexagonal grid (black).

The packing motif of these sheets, however, is not trivial to deduce. In both models the repeat distance of one unit cell along the c-axis is given unambiguously as 11.948 Å. If we suggest that singular sheets of aryl-linked, co-planar heptazine units stack in a graphitic fashion, we would require an interplanar stacking distance of the order of magnitude of graphite or other aromatic, discotic systems, namely 3.35 Å for crystalline graphite, 3.36 Å for graphitic carbon nitride and 3.52 Å for *g*-C_3N_4-mod2. Within 11.948 Å we could accommodate three layers of aryl-linked heptazines with a gallery height of 3.983 Å. Coming back to Table 1, we do indeed observe a corresponding reflection with reasonable intensity at 22.59° in terms of 2θ which in both models corresponds to the (0 0 3)-reflection. Now this gallery height is approximately 0.5 Å larger than that of any known discotic, aromatic systems. Although rotation about the C-C bond linking the aryl and the heptazine group is somewhat sterically hindered, it is not impossible, making individual sheets of HBF-1 rather floppy. Again corrugation of these sheets is a likely source of this apparent increase in gallery height, given that the corresponding reflections in the XRD pattern are projections of an average of all the unit-cell lengths along the c-axis.

Table 1.

HBF-1			
Hexagonal P6 (No. 191) *a* = *b* = 18.248 Å, *c* = 11.939 Å Monoclinc C2 (No. 5) *a* = 18.248 Å, *b* = 31.606 Å and *c* = 11.939 Å			
(*h k l*) P6	(*h k l*) C2	2θ / °	*d* / Å
(0 1 0)	(0 2 0), (1 1 0)	5.59	15.815
(0 0 1)	(0 0 1)	7.40	11.948
(1 1 0)	(2 0 0), (1 3 0)	9.67	9.146
(0 2 0)	(0 4 0), (2 2 0)	11.16	7.927
(1 1 1)	(2 0 1), (1 3 1)	12.19	7.260
(0 0 2)	(0 0 2)	14.78	5.992
(0 3 0)	(3 1 1)	16.77	5.286
(0 3 1)	(3 3 1)	18.40	4.821
(2 2 0)	(4 0 0)	19.43	4.568
(0 4 0)	(0 0 3)	22.59	3.935
(1 4 1)	(5 3 1)	27.00	3.303
(3 3 0)	(6 0 0)	29.52	3.026
(1 3 3)	(4 0 3)	29.98	2.981
(0 4 3)	(4 4 3)	31.86	2.809
(1 4 3)	(5 3 3)	34.38	2.609
(1 5 2)	(6 4 2)	35.02	2.562
(1 3 4)	(4 2 4)	36.44	2.466
(2 5 2)	(7 3 2)	38.53	2.336

This polymorphous disorder can be seen in the presence of a broad peak centred around 25.6° (*d* = 3.46 Å), which is visible throughout the whole condensation process leading to HBF-1. The condensation process was monitored in a powder XRD study presented in Figure 52 and is rather straightforward to follow. The crystalline component starts forming early at around 400 °C. The low-angle peak at 5.59° indicative of in-plane order forms from a broad pseudo-(001) peak at 5.3° visible as early as 390 °C. Simultaneously the broad peak at 25.6° diminishes as the temperature increases and the reaction is driven to completion. This indicates that either a phase change from an anisotropic to a crystalline material is taking place, or that the amorphous component is

decomposing in the process. In the light of the relatively low yield of these condensation reactions (around 40-50 %) the second scenario is more likely. As we have seen for the exfoliated graphite and graphitic carbon nitride systems in chapter 5 it is the crystalline packing which induces thermal and oxidative stability. Regrettably, in the case of the synthesis of HBF-1 the thermal requirement for deamination and ring-forming condensation must be balanced against the thermal decomposition of anisotropic crystallites or amorphous, polymeric intermediates – a trade-off which is redeemed in lower yield.

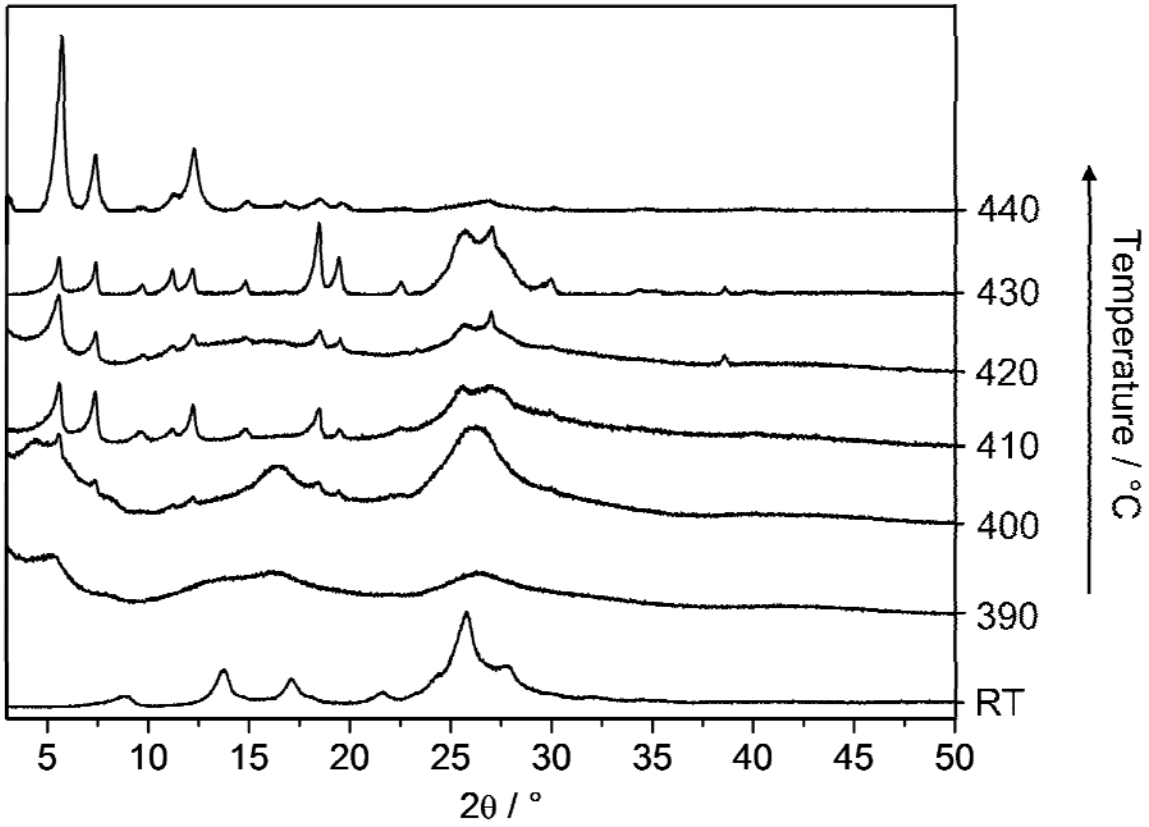

Figure 52. PXRD patterns of ArCNTz condensed in the LiBr/KBr salt melt and terminated at the temperatures given.

However, for the crystalline component a packing motif based on the results from diffraction and indexing can be proposed. A space filling concept which omits most steric repulsion effects would be an ABA' packing with the B-layer offset by 0.833 units along the *a*-axis and 0.333 units along the *b*-axis, and the A'-layer offset by 0.5 units along the *b*-axis. What sounds like a fanciful construct becomes obvious when the symmetry requirements of the monoclinic space group C2 are applied.

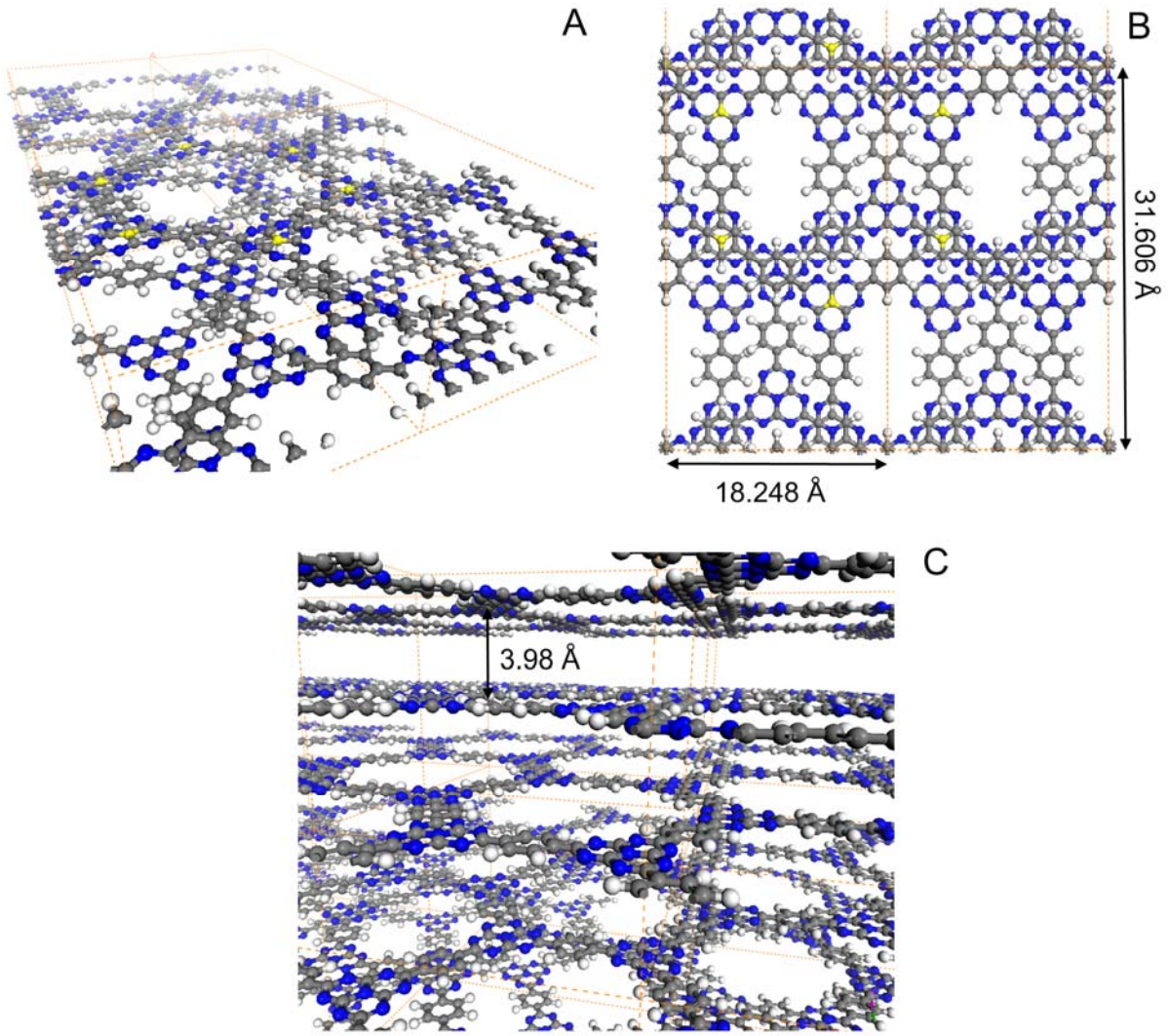

Figure 53. Proposed structure of HBF-1 as established by geometry optimisation using Accelrys' *Materials Studio Modelling*. Carbon and nitrogen atoms are represented as grey and blue spheres respectively. In (**A**) and (**B**) the central nitrogen atoms of neigbouring heptazine units were highlighted in yellow as a guide for the eye.

It is this structural model who was used as a basis for more rigorous Rietveld refinement with PowderCell (Version 2.4), and the result of this fit is seen in Figure 50, A. Peak broadening, asymmetry, and zero-shift errors were accounted for in a calculated diffraction profile and refined against the observed scattering to extract the intensities (F_{obs}) for each structure. The green difference plot, in Figure 50, A, indicate that the degree of fitting is acceptable for the refined profile (including unit cell parameters). Note that although we have not taken factors like aryl tilting or sheet buckling into account in the initial guess for the structure due to limited calculation time and capacity the fit yielded a

reasonable R_{wp}-value of 9.98 %. A full listing of atomic positions for this model can be found in the appendix, 8.7.

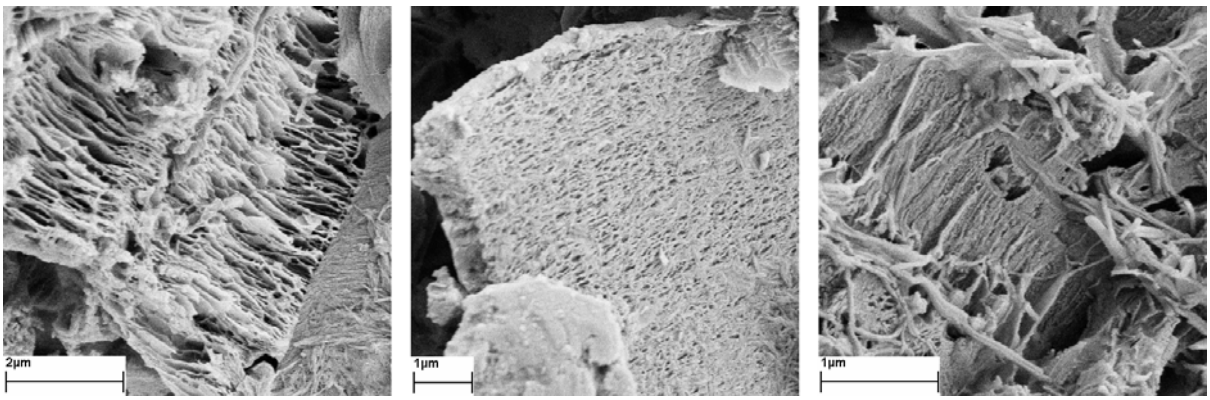

Figure 54. Representative SEM pictures of HBF-1 showing a propensity of the material to form layered structures.

The phase morphology of HBF-1 was studied by exhaustive scanning electron microscopy (SEM) imaging of the products from multiple reactions. Figure 54 reveals that HBF-1 has a high propensity to form layered structures, as might be expected. However no other clear indicators of molecular symmetry are visible in the shape of the crystals. As discussed previously the failure of this crystal system to adapt a discernible morphology on nanoscale might very well be the consequence of sterically disfavoured stacking. It seems rather that interplanar order is achieved on a very small length scale and a multitude of stacked domains lie next to each other in these pictures.

The architectural stability and porosity of HBF-1 was initially studied by measuring the nitrogen adsorption, however with a result of approx. 30 $m^2\ g^{-1}$ external surface area. Subsequently, a water adsorption study was performed on the guest-free material. A sample of as-synthesized HBF-1 was evacuated with 10^{-5} Torr vacuum pressure and heated to 160 °C for 12 hours to remove all the guests. This sample was used for measurement of the isotherm from 0 to 1 bar water vapour pressure, which shows gradual uptake at P/P_0 from 0.05 to 0.7, and no significant features of a accessible micropores (c.f. Figure 55). The slow rise in the isotherm occurring at higher pressures is due to the existence of a small population of external mesopores between the crystallites; this feature is not uncommon for particles with platelet morphologies.[75] Unfortunately, the Brunauer-Emmett-Teller (BET)

model cannot be reliably applied to water adsorption, so no good estimate of the apparent surface area can be given.

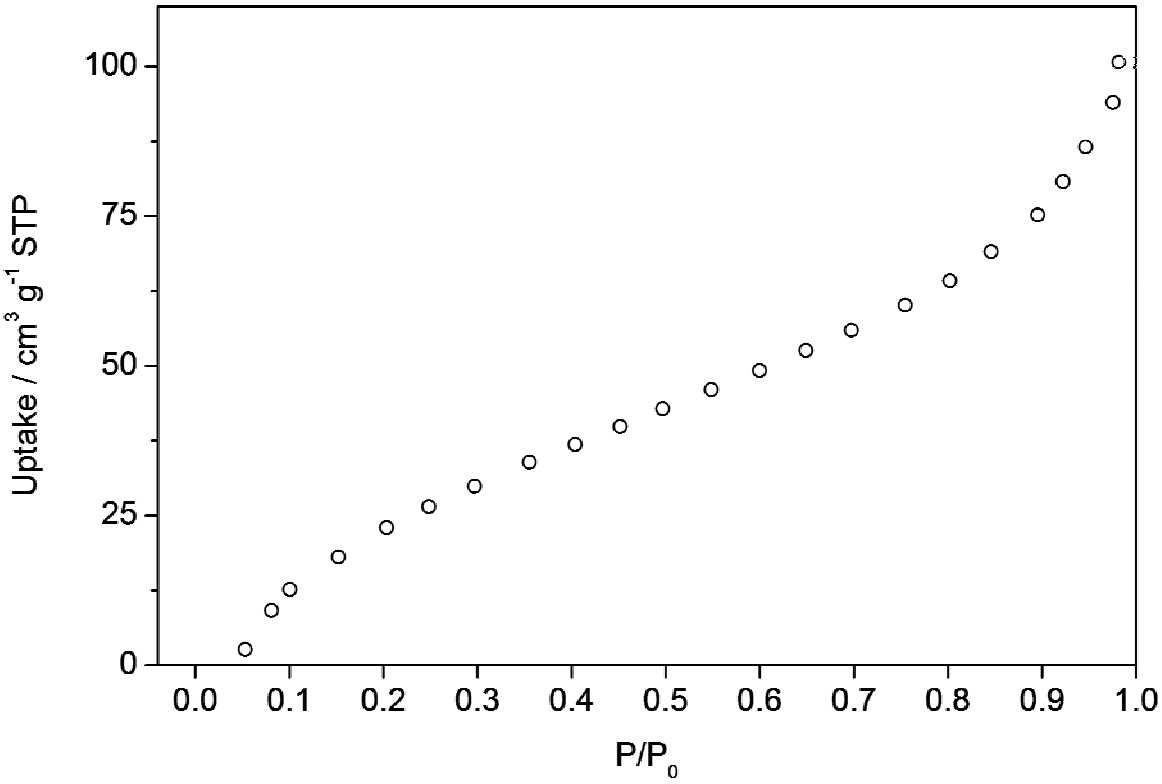

Figure 55. Water adsorption isotherm for HBF-1.

The lack of accessible micropores in both nitrogen and water adsorption reflects the structural model given in Figure 53 which predicts that cavities are superimposed by linkers from neighbouring layers.

6.4 From BiPhCNTz to HBF-2 – ionothermal synthesis and characterisation

In the preceding chapter we have demonstrated the synthesis of the heptazine based framework (HBF-1) from a simple molecular building block namely a *para*-substituted benzene ring with one triazine and one carbonitrile functionality (ArCNTz). The particular condensation mechanism employed relies on deamination and formation of a linking, tri-substituted heptazine unit (c.f. Figure 43). In this chapter we shall extend the repertoire of molecular building blocks for this type of condensation and thus demonstrate two-fold;

firstly, that the proposed condensation mechanism can be generalised and secondly that the crystal structure of heptazine based frameworks can be rationally tuned.

The formal name of the molecular precursor employed in this study is 4'-(4,6-diamino-1,3,5-triazin-2-yl)biphenyl-4-carbonitrile (in short BiPhCNTz). It is based on a biphenyl unit with one triazine and one carbonitrile group in *para*-position. The full synthetic procedure and characterisation can be found in the appendix, section 8.4. BiPhCNTz (1 g, 3.47 mmol) was homogenized with a 10 g of lithium bromide and potassium bromide in the eutectic ratio of 52:48 wt%. The reaction mixture was heated at 40 K min^{-1} under inert atmosphere and kept at terminal temperatures ranging between 390 and 450 °C for up to 80 h. Excess salt was dissolved in boiling, distilled water and removed through repeated washing. The product was thoroughly dried at 200 °C and 10^{-5} torr to yield the heptazine based framework, HBF-2 (0.34 g, 0.432 mmol, 50% yield) as a black-brown powder. It was found that the best yield was obtained at 430 °C and 26 h of reaction time.

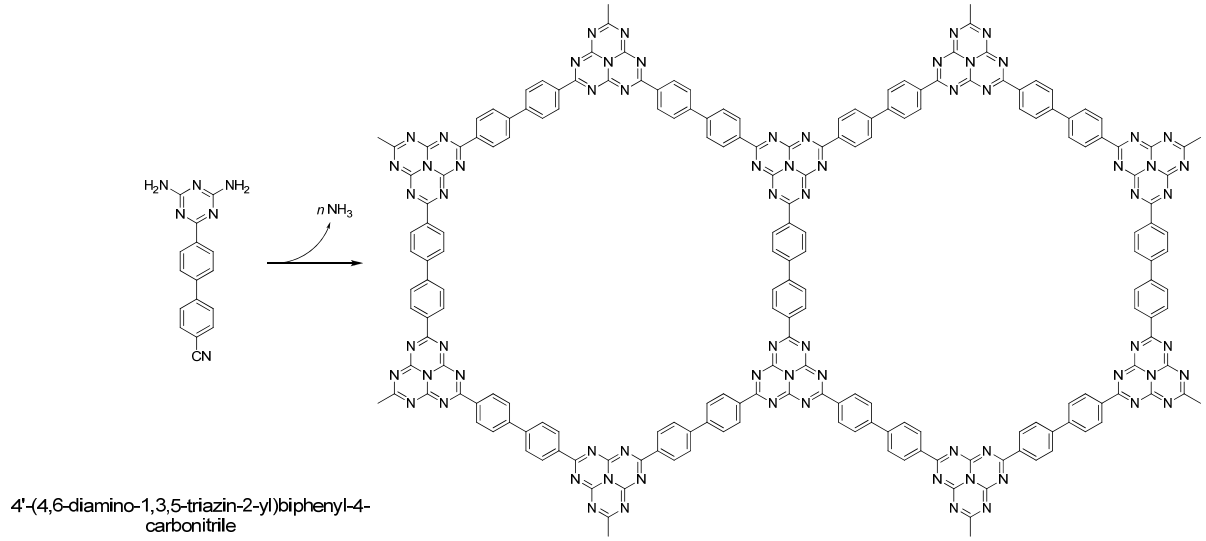

Figure 56. Condensation reaction of 4'-(4,6-diamino-1,3,5-triazin-2-yl)biphenyl-4-carbonitrile (BiPhCNTz) to give the extended heptazine based framework (HBF-2).

A preliminary elemental microanalysis of HBF-2 revealed the following composition: 63.4% C, 21.7% N, and 3.26% H, which would correspond to the molecular formula of $C_{48.0}N_{14.11}H_{29.44}$. The difference of 11.6% is rather large but in the light of the next to perfect

match of the C/N/H-ratio with the predicted structure (c.f. Figure 56), it is assumed that adsorbed water or remaining salt, which clog up the pores account for the mass discrepancy.

A close examination of the vibrational spectra (ATR-FTIR) obtained from intermediate condensation products reveals that the ammonia band disappears almost entirely around 430 and 440 °C, and the carbonitrile band around 2250 cm^{-1} also gradually disappears. At the same time the aromatic stretch at around 1600 cm^{-1} and the heptazine breathing mode at 800 cm^{-1} persist throughout the reaction. This is similar behaviour previously observed for the HBF-1 material and seen in context of the elemental analysis, it indicates that as the temperature rises, the condensation is driven to completion and all triazine and carbonitrile groups react with each other forming an extended heptazine based framework (Figure 57, A).

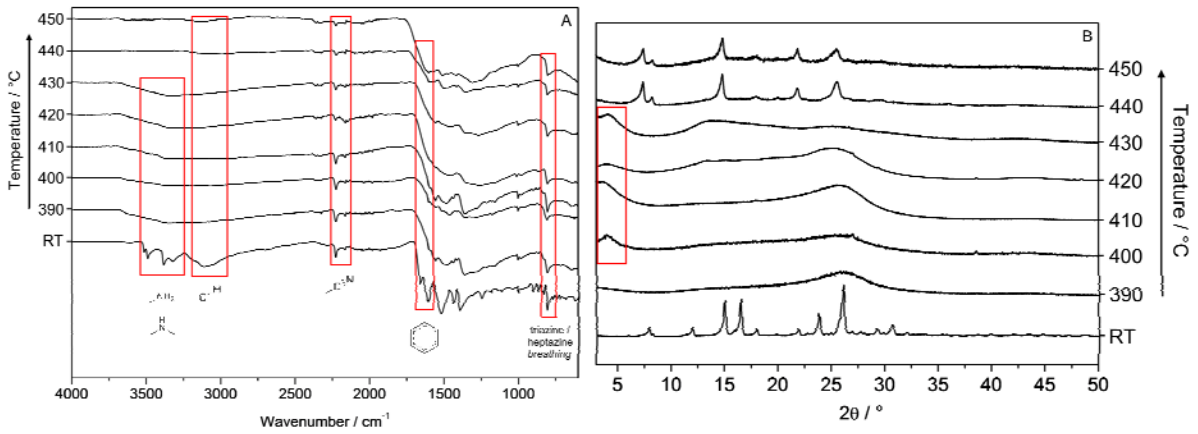

Figure 57. FTIR spectra of BiPhCNTz condensed in the LiBr/KBr salt melt (**A**) and the respective PXRD patterns (**B**).

Indexing of the experimental XRD patterns unambiguously gave unit cell parameters nearly equivalent to those outlined in the model (c.f. Table 2). To obtain the experimental values, the unit cell parameters were freely refined using full pattern decomposition and profile fitting of the diffraction patterns employing a model-biased Le Bail routine. The best fit was given by a hexagonal unit cell of the type P6 with parameters $a = b = 27.410$ Å, $c = 11.835$ Å ($g = 120°$). A sheet of the proposed model is seen below:

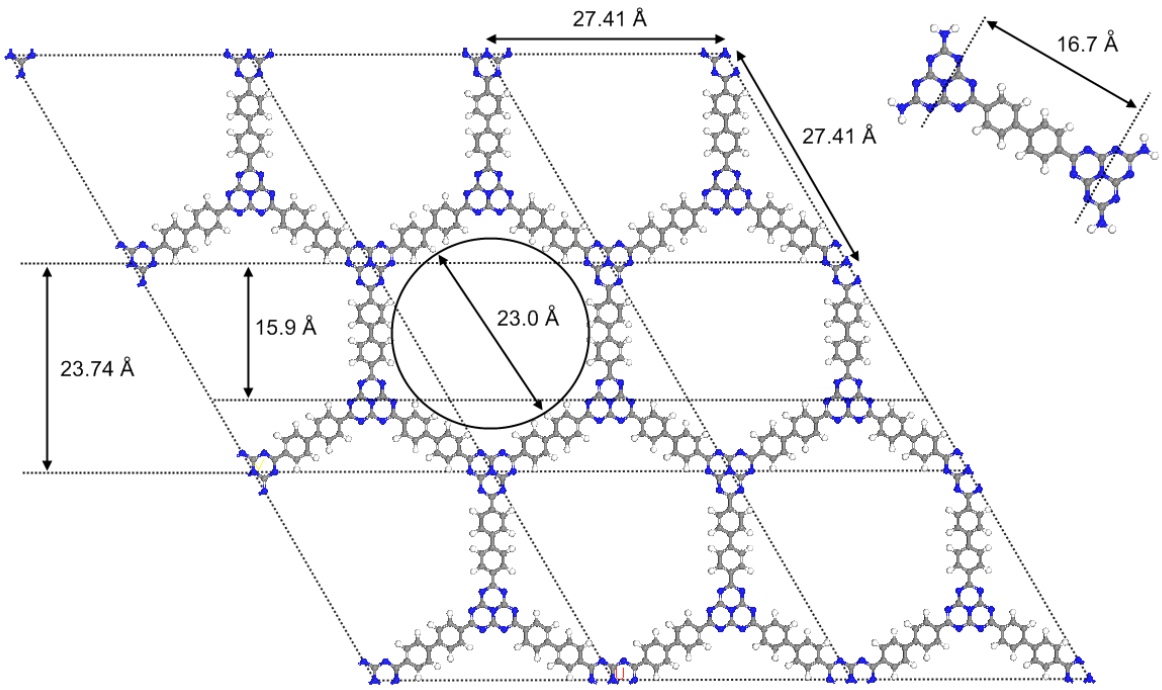

Figure 58. Proposed structural model for the in-plane order of HBF-2.

The model in Figure 58 assumes a distance between two heptazine units of 15.9 Å which is in reasonable agreement with the individually calculated distance between two heptazine units linked by a biphenyl of 16.7 Å. Since we are dealing with an initial model here, we will comment on the apparent discrepancy of 0.8 Å when we deal with the interlayer packing. Note that the first visible low angle peak in Table 2 which was indexed as $d_{(0\ 2\ 0)}$ = 12.07 Å corresponds nicely to the predicted distances in the model, namely half the unit cell height in both *a*- and *b*-direction given as 23.74 / 2 = 11.87 Å.

The green difference plot, in Figure 59, indicates an acceptable degree of fitting for the refined profile. The number of observed peaks in the pattern of HBF-2 was too few to permit refinement of atom positions in the model using Rietveld methods. Nevertheless, the initial intensities calculated via PowderCell (Version 2.4) used in the extraction represent viable models for these data, because statistically reasonable profiles could be obtained from readily convergent refinements [HBF-2: R_{wp} 8.39 %].

The changes in crystal structure during the condensation process of HBF-2 were monitored in Figure 57, B. The series of powder XRD patterns confirms the crystallinity of HBF-2 and reveals no diffraction peaks that could be attributed to the starting material or

their known solvate. The crystalline component emerges very late in the reaction around 440 and 450 °C. Prior to that, a very broad peak at 25.7 ° in terms of 2θ indicates that polymeric, aromatic precursors similar to the species observed in the previous chapters are among the intermediates of the condensation reaction. This peak likewise vanishes as the reaction is driven to completion by ever increasing temperatures. Simultaneously a pseudo-(1 0 0) peak is observed at 4.16 ° 2θ (*d* = 21.3 Å) for reaction intermediates in the temperature range of 400 to 430 °C. As this peak vanishes at higher temperatures, more defined peaks with (*h k* 0) components emerge.

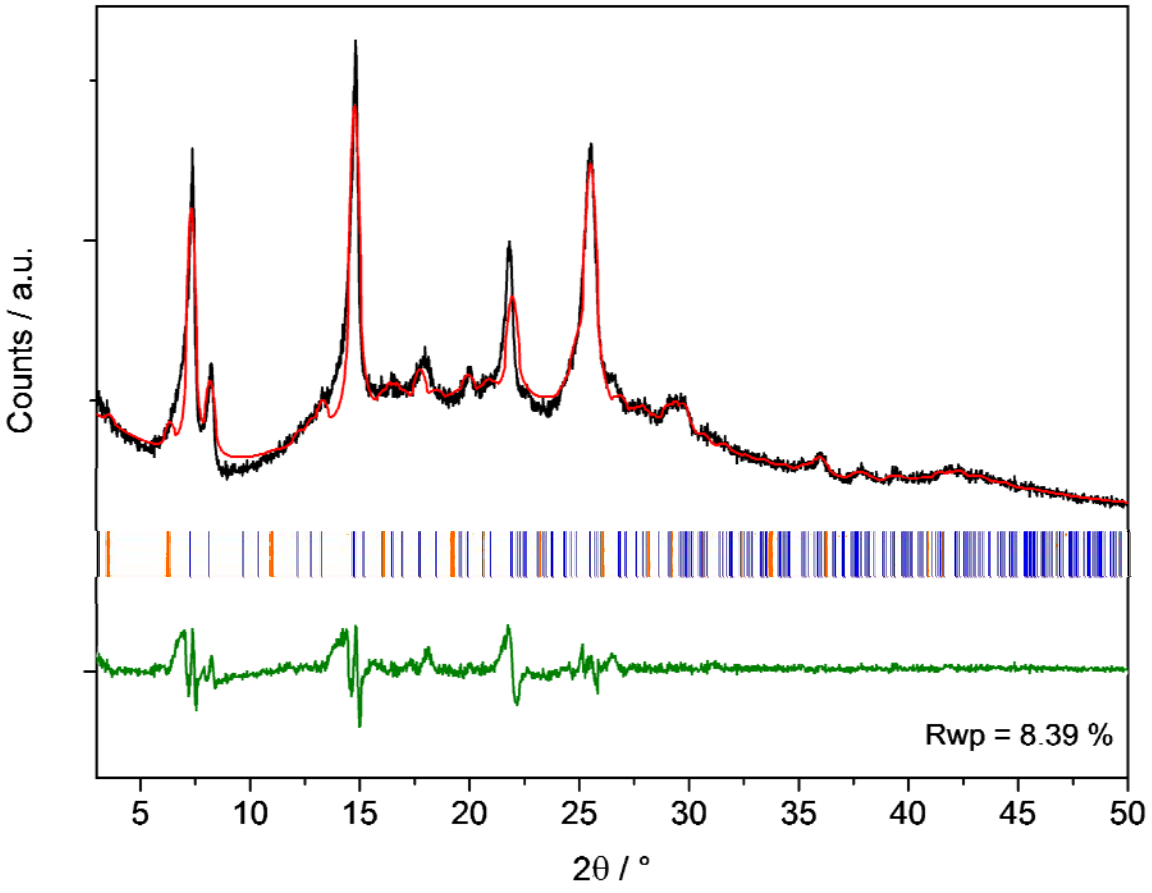

Figure 59. Physical characterisation of HBF-2 as obtained from the condensation of BiPhCNTz in the LiBr/KBr salt melt at 430 °C. structureless LeBail fit performed on the XRD pattern of HBF-2, the refined profile (red), the difference plot (green) with Bragg peak positions (blue) and systematic absences (orange).

The packing motif follows the trend seen in chapter 6.3 for HBF-1. The calculated and refined unit cell repeat along the *c*-axis of 11.835 Å suggests that three layers are

stacked within one unit cell each observing an interlayer spacing of 3.945 Å. With this in mind and in the light of the previous calculations, a space filling model for the HBF-2 unit cell is proposed in Figure 60. In analogy to the HBF-1 system the packing is of ABA' fashion wherein the heptazine units of two adjacent layers are superimposed and the biphenyl linkers fill up the cavities.

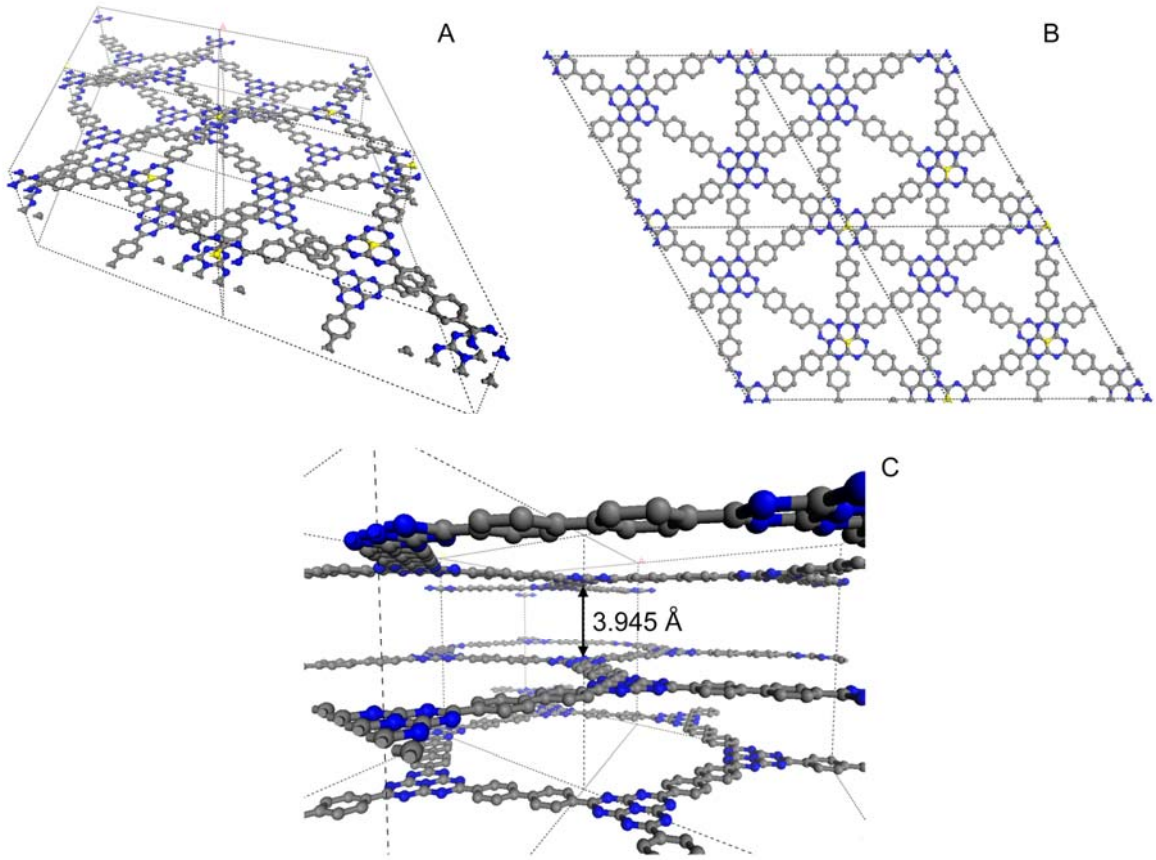

Figure 60. Proposed structure of HBF-2 as established by geometry optimisation using Accelrys' *Materials Studio Modelling*. Carbon and nitrogen atoms are represented as grey and blue spheres respectively. In (**A**) and (**B**) the central nitrogen atoms of neigbouring heptazine units were highlighted in yellow as a guide for the eye.

Why is that a reasonable assumption for a model? Firstly, it is known from biphenyl, and especially its ortho-substituted compounds that rotation about the single bond is sterically hindered. The linking biphenyl group in our system – should it not be engaged in overall π-electron delocalisation – will experience a similar sort of repulsion from the nitrogen lone pairs of the neighbouring heptazine units and between each other, and as a result most likely twist out of plane. In such a confirmation the aryl unit will obstruct packing

motifs which are dominated by π-π electron interactions for the aforementioned systems. A biphenyl group can be enveloped into a cylinder with a radius of approximately 5 Å when the van der Waals radii of all constituent elements are concerned, i.e. a phenyl linker which is oriented perpendicular to the plane of bonding has an increased space requirement of 1.6 Å when compared to a co-planar arrangement where it should not penetrate further than 1.7 Å into the interlayer gallery (1.7 Å is the van der Waals radius of a carbon atom). Secondly, it is noteworthy that the refinement procedure did not seem to indicate any other solution than that of a layered system. This should be somewhat surprising since it is quite likely that the polymeric precursors of HBF-2 will adopt a twisted confirmation during the condensation reaction in which two biphenyl-linked hepatzine units will in a orthogonal (or next to orthogonal) conformation with respect to one another (c.f. Figure 61). Such a confirmation would give rise to a 3D network rather than a 2D layered structure. However it seems that the propensity of heptazine units to stack on each other through favourable π-π interactions induces the graphitic stacking. The expanded gallery height and the discrepancy of 0.8 Å we have seen earlier for the unit-cell dimensions in *a*- and *b*-direction hints strongly towards corrugation of individual layers of HBF-2 as observed previously.

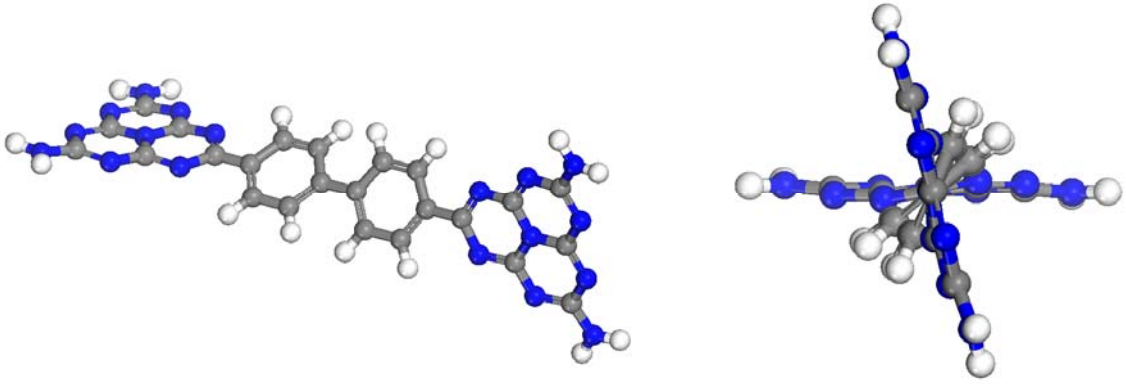

Figure 61. Geometry optimised biphenyl-bis-heptazine unit calculated using density functional theory (B3LYP) showing an out-of-plane twist of the constituents.

The phase morphology of HBF-2 was imaged using SEM and TEM, and representative pictures of the condensed phase are seen in Figure 62. Although some propensity to form layered, clay-like structure is seen in Figure 62, A, it is only on the scale of nanometers that we find homogenously shaped, crystalline domains (c.f. Figure 62, B). The morphological

behaviour of HBF-2 is quite analogous to HBF-1 in that respect that strained graphitic stacking inhibits the formation of well defined crystals on nanometer scale.

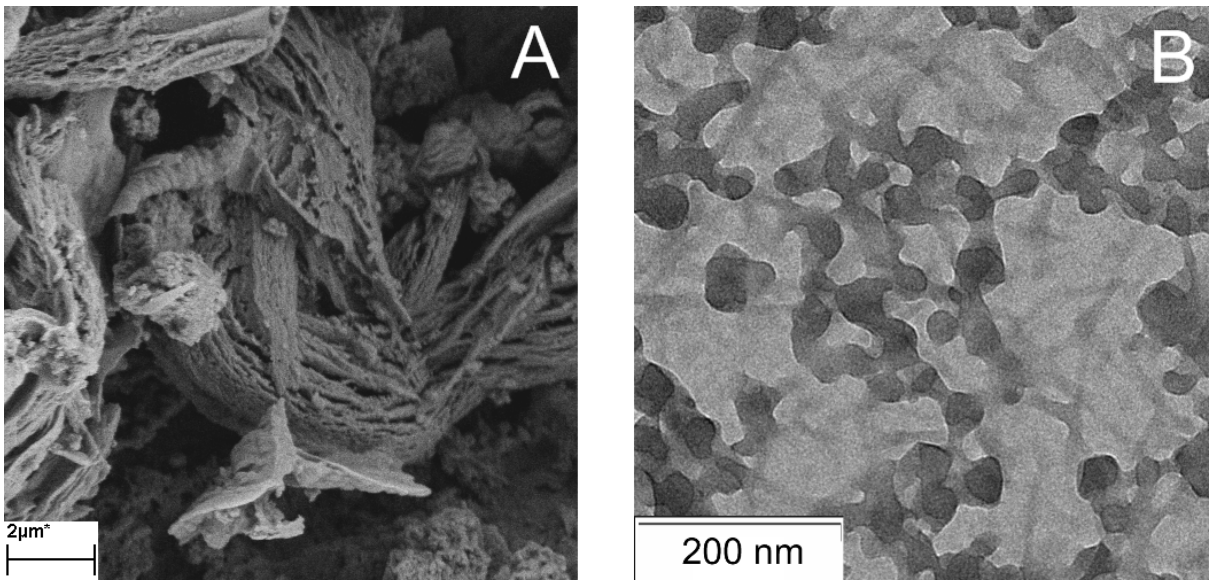

Figure 62. Representative SEM picture (**A**) and TEM picture (**B**) of HBF-2.

Nonetheless, the x-ray diffraction studies, the indexing and refinement, the results from vibrational spectroscopy and from elemental analyses make a strong case in favour of the formation of the heptazine based frameworks, HBF-1 and HBF-2. In both cases we are looking at 2D frameworks of heptazine-linked, aromatic bridging units rather than 0D or 1D molecular structures as known from organic and polymer chemistry. Both structures are intellectually appealing as organic zeolites, and they hold exiting prospects as lightweight materials optimized for gas storage, photonic and catalytic applications when a way is found to access their inherent microporosity.

7 Conclusion and outlook

The work at hand deals with the synthesis and characterisation of new allotropes and nanostructures of carbon nitrides and touches on some prospective applications. All extended, covalently linked carbon nitride frameworks presented above were synthesised from simple, molecular precursors in a process referred to as ionothermal synthesis – a high temperature treatment employing eutectic salt melts as unconventional solvents. The condensations follow a reaction mechanism of temperature induced deamination and formation of an extended aromatic unit, the tri-substituted heptazine.

The thesis follows four overarching themes starting with the introduction to carbon nitride systems and the quest for a material solely comprised of carbon and nitrogen which started as early as 1834 with Justus von Liebig's observations on "some nitrogen compounds".

The first section shows the successful synthesis of graphitic carbon nitride (*g*-C_3N_4), a species which is based on sheets of hexagonally arranged s-heptazine units that are held together by covalent bonds between C and N atoms which are stacked in a graphitic, staggered fashion.

The second section touches on the variety of salt melt systems suitable for ionothermal synthesis and demonstrates that a variation of the salt melt yields a different phase of graphitic carbon nitride – *g*-C_3N_4-mod2.

In the third section, intercalation chemistry known from graphite is performed on *g*-C_3N_4 to yield a potassium intercalation compound thereof ($K(C_6N_8)_3$). This compound can be readily exfoliated to give bundles of carbon nitride nanosheets analogous to the graphitic system and has interesting optical properties.

The fourth and final section deals with the introduction of aryl- and biphenyl-bridges into the carbon nitride materials via rational synthesis of the molecular precursors yielding heptazine based frameworks, HBF-1 and HBF-2 – two covalent, organic frameworks.

A graphical overview of the results of this work is given below:

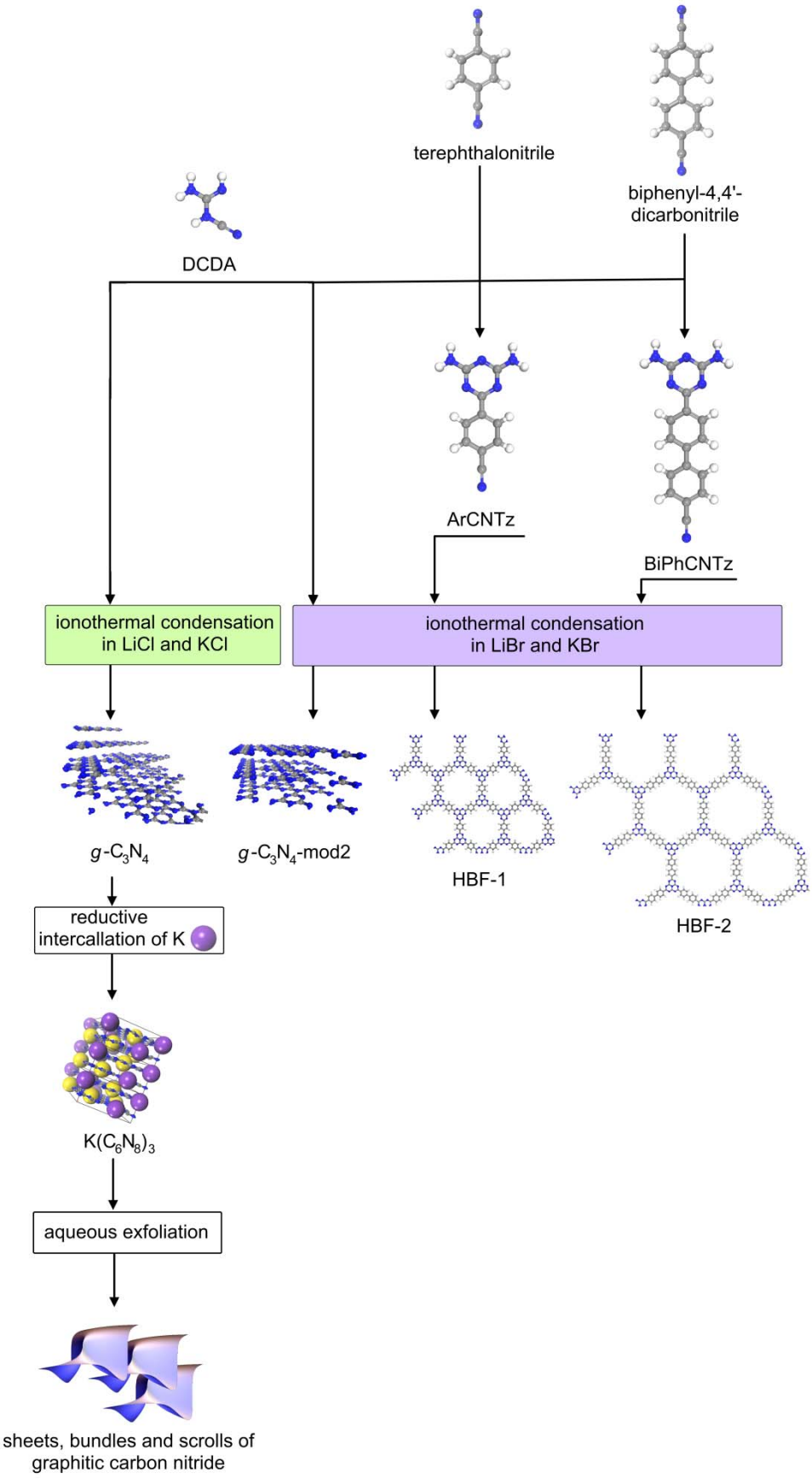

Figure 63. Graphical overview of the work on carbon nitride allotropes and nanostructures.

In the first section graphitic carbon nitride was for the first time synthesised using the high-temperature condensation of dicyandiamide – a simple molecular precursor – in a eutectic salt melt of lithium chloride and potassium chloride. The extent of condensation, namely next to complete conversion of all reactive end groups, was verified by elemental microanalysis and vibrational spectroscopy. TEM- and SEM-measurements gave detailed insight into the well-defined morphology of these organic crystals, which are not based on 0D or 1D constituents like known molecular or short-chain polymeric crystals but on the packing motif of extended 2D frameworks. The proposed crystal structure of this *g*-C_3N_4 species was derived in analogy to graphite by means of extensive powder XRD studies, indexing and refinement. It is based on sheets of hexagonally arranged s-heptazine (C_6N_7) units that are held together by covalent bonds between C and N atoms. These sheets stack in a graphitic, staggered fashion adopting an AB-motif, as corroborated by powder X-ray diffractometry and high-resolution transmission electron microscopy. This study was contrasted with one of many popular – yet unsuccessful – approaches in the last 30 years of scientific literature to perform the condensation of an extended carbon nitride species through synthesis in the bulk.

The second section expands the repertoire of available salt melts introducing the lithium bromide and potassium bromide eutectic as an excellent medium to obtain a new phase of graphitic carbon nitride. The combination of SEM, TEM, PXRD and electron diffraction reveals that the new graphitic carbon nitride phase stacks in an ABA' motif forming unprecedentedly large crystals. This section seizes the notion of the preceding chapter, that condensation in a eutectic salt melt is the key to obtain a high degree of conversion mainly through a solvatory effect. Although the resulting products both *g*-C_3N_4 and *g*-C_3N_4-mod2 were unambiguously characterised, the actual reason as to why their crystal structure and morphology changes as the solvent is altered remains a subject of educated guessing until the kinetic and thermodynamic behaviour of organic molecules in high-temperature salt melts is elucidated. Nonetheless, at the close of this chapter ionothermal synthesis is seen established as a powerful tool to overcome the inherent kinetic problems of solid state reactions such as incomplete polymerisation and condensation in the bulk. Myriads of eutectic salt compositions are waiting to take over where solvents known from classical chemistry fail. Among the sample cases for the promising adoption of salt melts is surely the chemistry with precursors such as melem and

melon, which simply cannot be solubilised in any classical solvent. Another case is when the temperature requirement of the reaction in question falls into the proverbial “no man’s land” of classical solvents, i.e. above 250 to 300 °C. It remains an interesting question what other pieces of long-forgotten polymer- and network-chemistry can be brought to fruition when ionothermal synthesis is employed.

The following section puts the claim to the test, that the crystalline carbon nitrides obtained from a salt melt are indeed graphitic. A typical property of graphite – namely the accessibility of its interplanar space for guest molecules such as light and heavier metals (Li, Na and K, Rb, Cs respectively), strong mineral acids (e.g. sulphuric or nitric acid) and halogens and halides – is transferred to the graphitic carbon nitride system. Metallic potassium and graphitic carbon nitride are converted to give the potassium intercalation compound, $K(C_6N_8)_3$ designated according to its stoichiometry and proposed crystal structure. Reaction of the intercalate with aqueous solvents triggers the exfoliation of the graphitic carbon nitride material and – for the first time – enables the access of singular (or multiple) carbon nitride sheets analogous to graphene as seen in the formation of sheets, bundles and scrolls of carbon nitride in TEM imaging. The thus exfoliated sheets form a stable, strongly fluorescent solution in aqueous media, which shows no sign in UV/Vis spectroscopy that the aromaticity of individual sheets was subject to degradation. This chapter only touches on the wide-range of known graphite chemistry, which is waiting for application on the new carbon nitride system. Further studies in this field will reveal whether intercalation compounds of graphitic carbon nitride behave in analogous fashion to the graphite systems with respect to their interesting electrical properties, also. Furthermore, since graphitic nanoscrolls are considered to be precursors of multiwalled carbon nanotubes, it remains to be seen whether graphitic carbon nitiride sheets can be converted likewise.

The final section expands on the mechanism underlying the formation of graphitic carbon nitride by literally expanding the distance between the covalently linked heptazine units which constitute these materials. A close examination of all proposed reaction mechanisms to-date in the light of exhaustive DSC/MS experiments highlights the possibility that the heptazine unit can be formed from smaller molecules, even if some of the designated leaving groups (such as ammonia) are substituted by an element, *R*, which later on remains linked to the nascent heptazine. Furthermore, it is suggested that the key

functional groups in the process are the triazine- (Tz) and the carbonitrile- (CN) group. On the basis of these assumptions, molecular precursors are tailored which encompass all necessary functional groups to form a central heptazine unit of threefold, planar symmetry and then still retain outward functionalities for self-propagated condensation in all three directions. Two model systems based on a para-aryl (ArCNTz) and para-biphenyl (BiPhCNTz) precursors are devised via a facile synthetic procedure and then condensed in an ionothermal process to yield the heptazine based frameworks, HBF-1 and HBF-2. Due to the structural motifs of their molecular precursors, individual sheets of HBF-1 and HBF-2 span cavities of 14.2 Å and 23.0 Å respectively which makes both materials attractive as potential organic zeolites. Crystallographic analysis confirms the formation of ABA' layered, graphitic systems, and the extent of condensation is confirmed as next-to-perfect by elemental analysis and vibrational spectroscopy. The sheer fact that these extended, crystalline entities form shows that the basic considerations on the mechanism of heptazine-formation are valid. The procedure to prepare the triazine- and carbonitrile-functionalised precursors is easily adapted to a multitude of fathomable molecules of 2D or 3D symmetry. This toolbox is limited by two requirements only; firstly, that (at least) two carbonitrile groups can be introduced into the molecule and secondly, that the molecule is thermally stable beyond the temperature of formation of the heptazine unit (approx. 380 °C). In the present state, the intrinsic microporosity of these systems cannot be accessed since the ABA' packing seals the pores for the most conventional adsorbents (i.e. nitrogen and water). As a consequence, the great potential prospects of these materials as true organic zeolites, as nanoreactors or generally as absorbers of high-surface area are open to speculation. A future challenge would be to synthesise a phase of HBF-1 and HBF-2, which observes either AB- or (ideally) A-type stacking of individual sheets. This could be achieved twofold; either by smart selection of crystallisation conditions (as seen before for *g*-C_3N_4 and *g*-C_3N_4-mod2) or by the introduction of a guest molecule which would in turn, either induce the desired stacking motif or inhibit the ABA' stacking propensity of the material.

In a recapitulatory view, the chemistry of carbon nitrides and of ionothermal synthesis should be clearly considered as a door-opener for many areas of inorganic-, physical-, polymer- and organic chemistry. This "new and old" class of materials, which does not fail to fascinate since 1834, holds suprising properties of which many are yet to be discovered.

8 Appendix

8.1 General methods and characterisation techniques

8.1.1 Wide angle x-ray scattering (WAXS)

Powder X-ray diffraction (PXRD) experiments were performed on a Bruker D8 Advance diffractometer in reflectance Bragg-Brentano geometry using Cu Kα1 radiation with a curved Germanium 111 primary monochromator operating at 40 kV accelerating voltage and 40 mA current. Typical data acquisition times were 30 min for a 4 – 60° 2θ scan using 0.02° steps. The samples were used 'as synthesised' and were not subject to grinding or sieving prior to X-ray analysis since the particle sizes were found to be sufficiently monodisperse by TEM and SEM. It should be noted however, that for some materials the crystallite sizes were found to be in the micron region and are most likely a source of peak broadening.

8.1.2 Thermogravimetric analysis (TGA)

Thermogravimetric analysis was carried out using a NETZSCH TG 209 F1. The samples were heated in crucibles of aluminium oxide at a heating rate of 20 K min^{-1} under oxygen.

8.1.3 Elemental microanalysis

Elemental microanalyses (C, H, N, S, O) were performed on a Elemental Analyzer EA 1110, Fa. CE Instruments (Fraunhofer Institute for Applied Polymer Research, Potsdam, Germany).

8.1.4 Infrared measurements

Fourier transform infrared (FT-IR) measurements were carried out on a Bio-Rad FTS-6000 system with an attenuated total reflection (ATR) setup. FT-IR spectra of bulk samples were recorded at ambient temperature in a range from 4000 to 400 cm^{-1}.

8.1.5 Electron microscopy

The particle morphology was visualised on a Gemini Scanning Electronic Microscope (SEM). Preliminary TEM pictures were recorded using an Omega 912 Transmission Electron Microscope (TEM) (Carl Zeiss, Oberkochen, Germany). Subsequently the microstructure of the graphitic carbon nitride particles was studied on a Philips TEM/STEM CM 200 FEG transmission electron microscope equipped with a field emission gun operating at 200 keV acceleration voltage.

8.1.6 Electron spectroscopy

Electronic structure measurements were performed using Electron Energy Loss Spectroscopy (EELS) on a GATAN Tridiem image filter. XPS, EDX.

8.2 Synthesis of graphitic carbon nitride – g-C_3N_4

Dicyandiamide (DCDA) (≥ 98.0%) was purchased from Fluka. Lithium chloride (≥ 99%) and potassium chloride (≥ 99.5 %) was purchased from Carl Roth GmbH + Co. KG.

8.2.1 Thermogravimetric Analysis.

Figure A1: TGA trace for a sample of *g*-C_3N_4 under O_2 atmosphere.

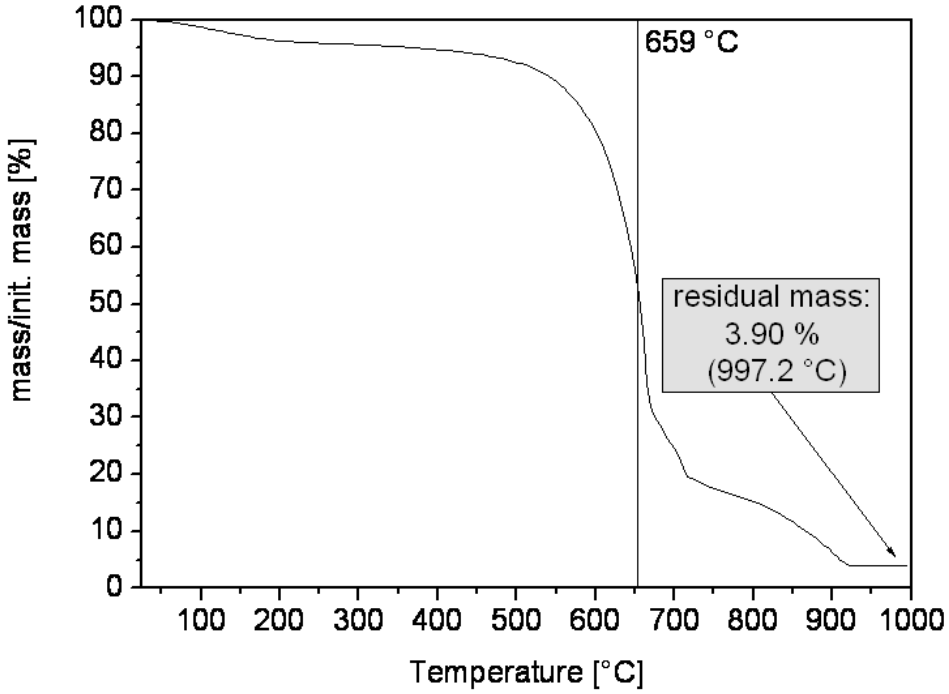

8.2.2 Results from structureless LeBail fit and unit cell refinement.

Found below is a table of the crystallographic parameters including the peak positions and corresponding *hkl*-values for *g*-C_3N_4. The XRD pattern of graphitic carbon nitride obtained from thermal condensation of dicyandiamide in a molten salt was fitted using a combination of *XFIT* [Cheary, R. W. & Coelho, A. A. (1996). Programs XFIT and FOURYA, deposited in CCP14 Powder Diffraction Library, Engineering and Physical Sciences Research Council, Daresbury Laboratory, Warrington, England. (http://www.ccp14.ac.uk/tutorial/xfit-95/)] and *CRYSFIRE* [R. Shirley, The CRYSFIRE System for Automatic Powder Indexing. (http://www.ccp14.ac.uk/tutorial/crys/)] powder indexing suits.

Table S1:

***g*-C_3N_4**				
Hexagonal $P6_{3cm}$ (No. 185) $a = b = 8.434$ Å, $c = 6.722$ Å				
hkl	2θ / °	*d* / Å	I / I_0	FWHM
100	12.108	7.3037	25.20	0.302
110	21.051	4.2168	24.97	0.321
200	24.354	3.6519	10.47	0.330
111	24.906	3.5722	64.80	0.337
002	26.497	3.3612	100.00	0.337
102	29.225	3.0534	65.98	0.346
210	32.405	2.7606	17.89	0.358
112	34.084	2.6284	1.48	0.364
211	35.113	2.5536	1.07	0.368
202	36.296	2.4731	2.21	0.373
300	36.890	2.4346	0.15	0.376
212	42.334	2.1333	1.10	0.401
220	42.857	2.1084	4.36	0.403
310	44.700	2.0257	4.40	0.412
221	45.026	2.0118	4.15	0.414
113	45.820	1.9787	1.70	0.418
302	45.993	1.9717	1.52	0.419
311	46.801	1.9396	2.91	0.423
400	49.904	1.8260	0.60	0.440
222	51.097	1.7861	6.43	0.447
213	52.560	1.7398	0.09	0.456

312	52.717	1.7350	0.09	0.456
004	54.562	1.6806	8.38	0.468
320	54.737	1.6756	0.34	0.469
104	56.112	1.6378	0.04	0.477
321	56.560	1.6259	0.19	0.480
402	57.383	1.6045	0.30	0.485
410	57.803	1.5938	0.55	0.488
114	59.131	1.5612	1.70	0.496
411	59.564	1.5508	1.51	0.499

Figure S2: Observed PXRD pattern of g-C3N4 (black), structureless LeBail fit (red), difference plot (green) and indexed peak positions.

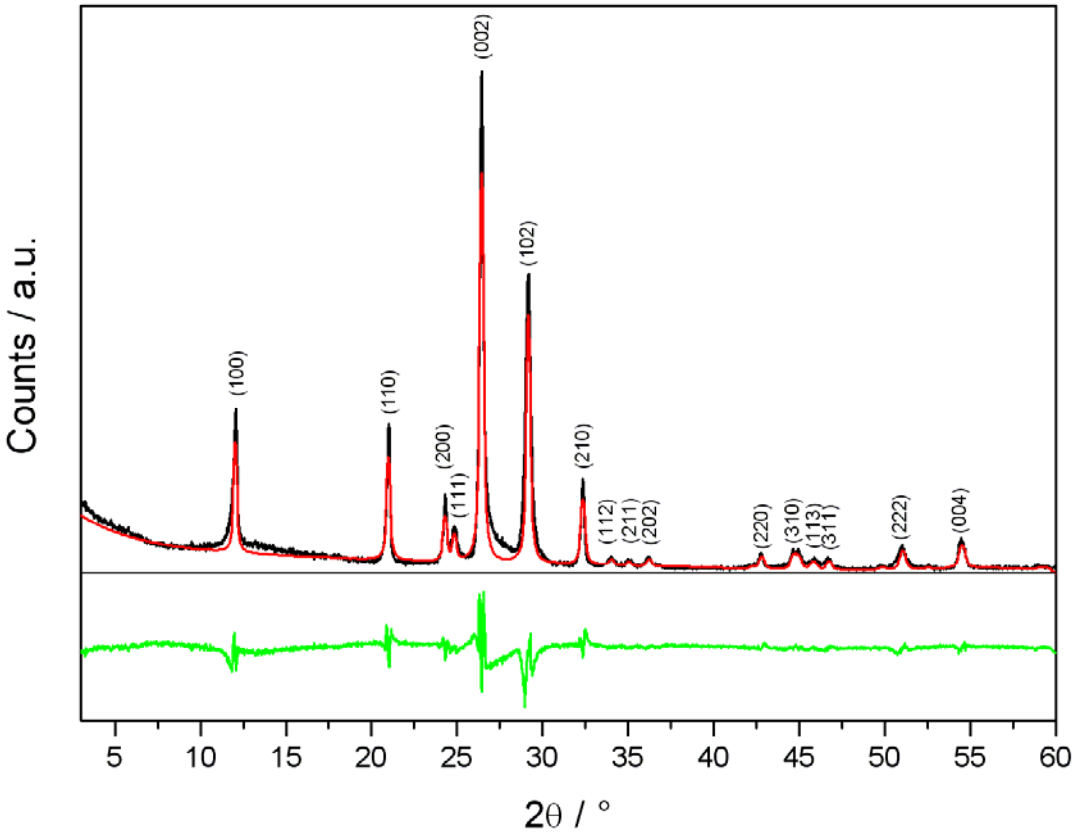

8.2.3 Scanning Electron Microscopy Imaging (SEM) of g-C3N4.

Figure S3: SEM image of *g*-C_3N_4 showing an array of hexagonal prisms.

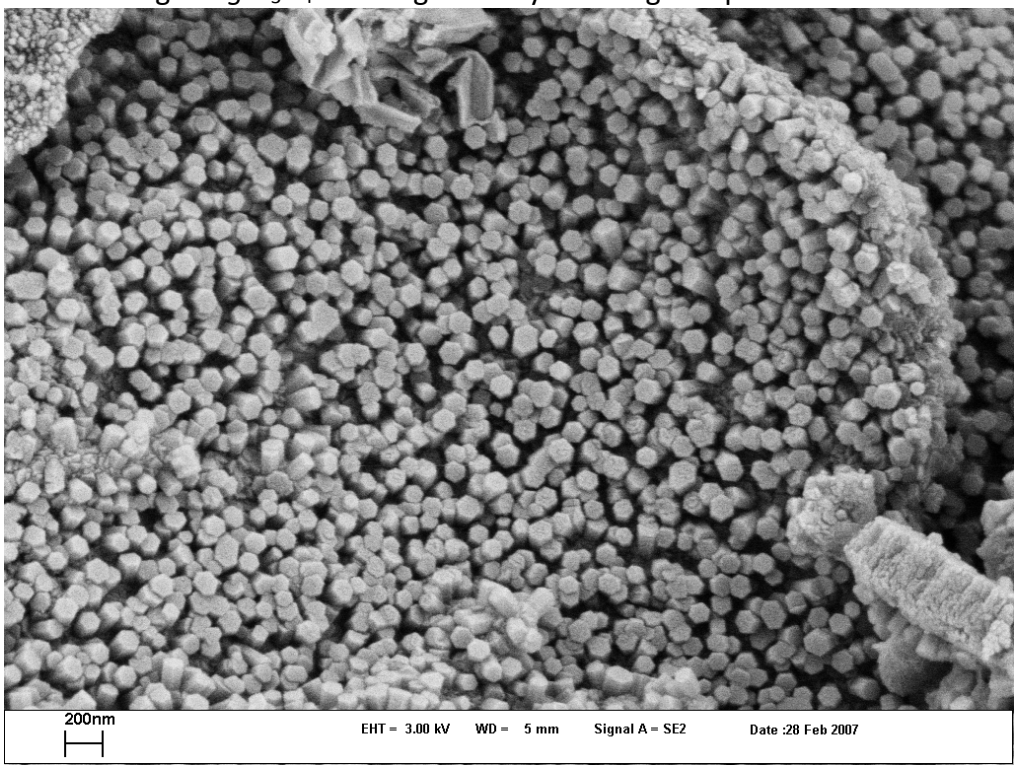

8.3 Synthesis of ArCNTz

1,4-Dicyanobenzene was purchased from Aldrich

CAS # 623-26-7

Product # D76722-25G

ArCNTz1,4-Dicyanobenzene (5.0g, 38.2mmol, 98% pure) and DCDA (3.25g, 38.2mmol, 99% pure) in Isopropanol (140cm3) were heated to 105°C. KOH (0.36g, 6.4mmol) was dissolved in Isopropanol (10cm3) and added dropwise to the reaction mixture which was then refluxed at 105°C for 1 hour. The solution was poured into cold water and the white ppte collected and washed with cold water until neutral. The product (7.50g, 92.4% yield) was dried in vacuo.

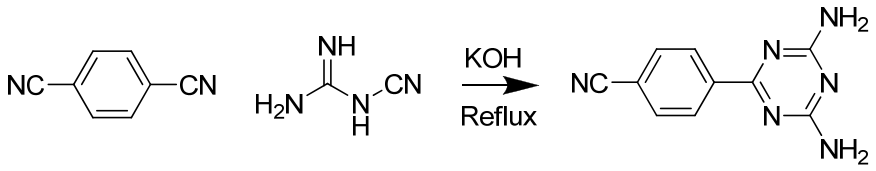

ArCNTz

Elemental Analysis C10.0H8.0N5.6O0.4 (Theory: C10.0H8.0N6.0O0.0)

IR 808.1cm-1 (Tz); 1390.6 - 1558.4 cm-1 (Ph); 2160.2 cm-1 (CN)

NMR

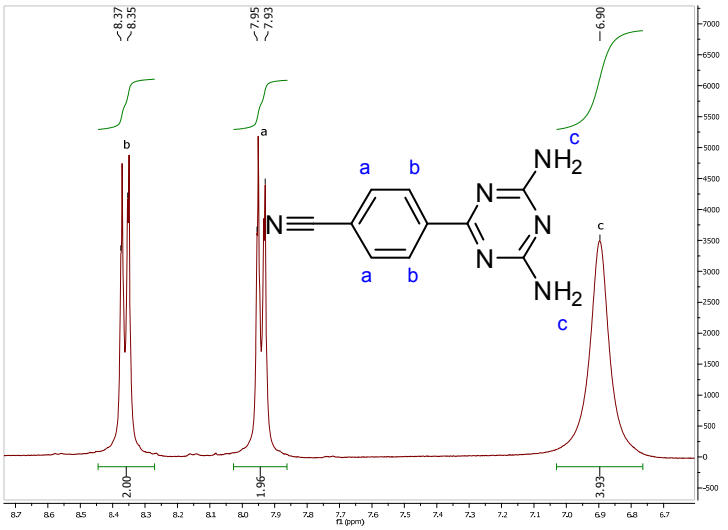

1H NMR (400 MHz, DMSO) δ = 8.40, 8.35(d, 2Hb), 7.95, 7.89(d, 2Ha), 6.90 (s, 4Hc), 3.33(s, H2O), 2.50(s, DMSO-d6)

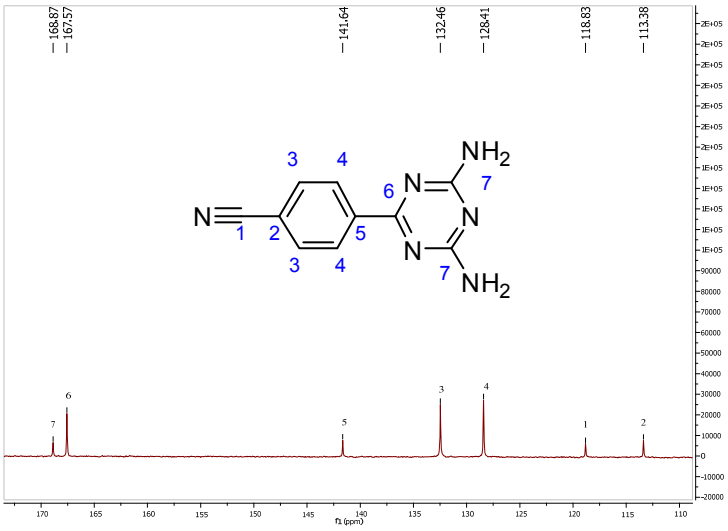

13C NMR (101 MHz, DMSO) δ 168.87, 167.57, 141.64, 132.46, 128.41, 118.83, 113.3

8.4 Synthesis of BiPhCNTz

4,4'-Biphenyldicarbonitrile was purchased from Aldrich

CAS #	1591-30-6
Product #	544450-5G

BiPhCNTz 4,4'-Biphenyldicarbonitrile (3.0g, 14.25mmol, 97% pure) and DCDA (1.21g, 14.24mmol, 99% pure) in Isopropanol (100cm3) were heated to 110°C. KOH (0.13g, 2.32mmol) was dissolved in Isopropanol (10cm3) and added dropwise to the reaction mixture which was then refluxed at 110°C for 18h. The solution was poured into cold water and the yellow ppte collected and washed with cold water until neutral. The product (3.86g, 94.0% yield) was dried in vacuo.

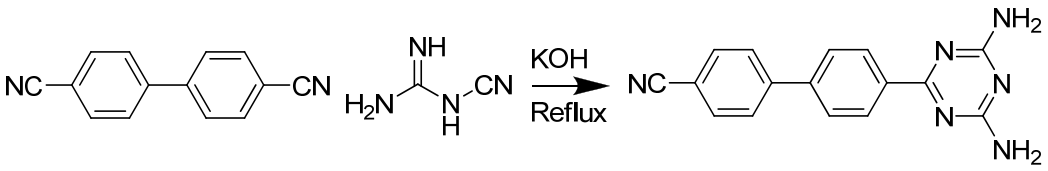

BiPhCNTz5

Elemental Analysis C16.0H12.4N5.5O0.7 (Theory: C16.0H12.0N6.0O0.0)

IR 806.2cm-1 (Tz); 1394.5 - 1533.4 cm-1 (Ph); 2227.7 cm-1 (CN)

NMR

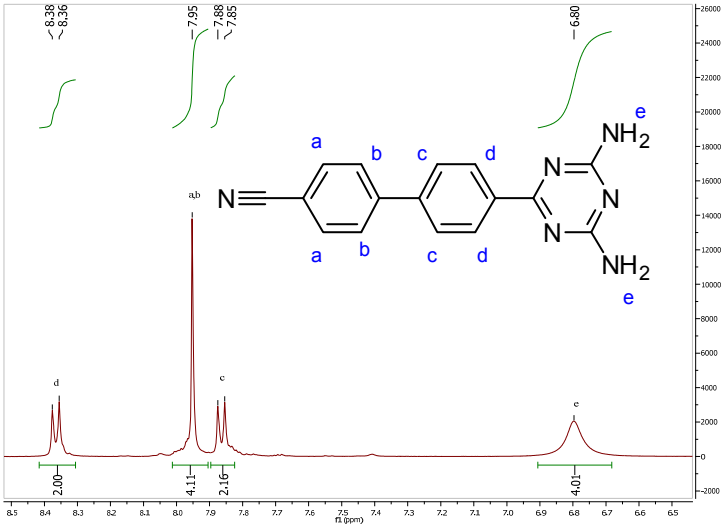

1H NMR (400 MHz, DMSO) δ = 8.38, 8.36(d, 2Hd), 7.95(s,4Ha,b), 7.88, 7.85(d, 2Hc), 6.80(s, 4He)

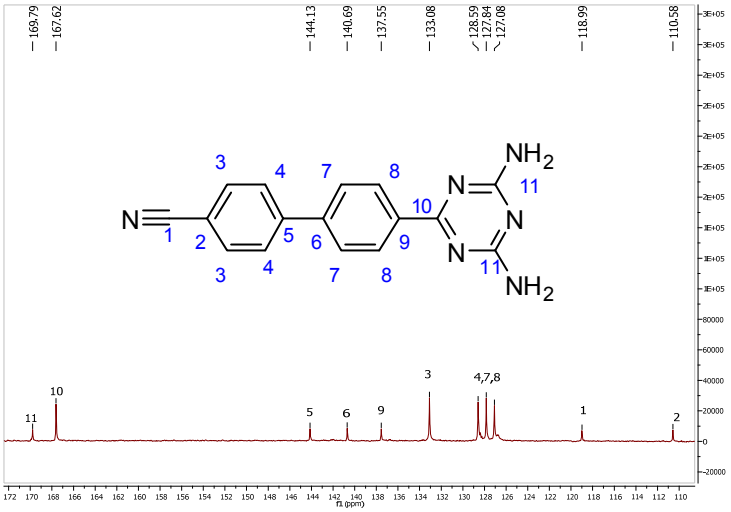

13C NMR (101 MHz, DMSO) δ = 169.79, 167.62, 144.13, 140.69, 137.55, 133.08, 128.59, 127.84, 127.08, 118.99, 110.5

8.5 Synthesis of NaphthaCNTz

2,6-Dicyanonaphthalene was synthesized from a 2,6-Dibromonaphthalene precursor which was purchased from Alfa Aesar.

CAS #	13720-06-4
Product #	L16134

2,6-Dibromonaphthalene (1.0 g, 3.5 mmol) and CuCN (1.25g, 14mmol) were stirred at 110 °C for 118h in dry, degassed DMF (20cm3). The reaction was monitored by TLC until all the starting compound was consumed.

The green/brown solution was cooled and poured into CH2Cl2 until the organic nitrile was dissolved. An aqueous solution of TMEDA was added to form a blue complex with Cu(I). The organic phase was extracted. As much CH2Cl2 as possible was removed and the leftover concentrated solution run through a silica 60 column using CH2Cl2 as the eluent (Rf value of product ~ 2.2). The solvent was removed and the resulting off-white ppte dried in vacuo.

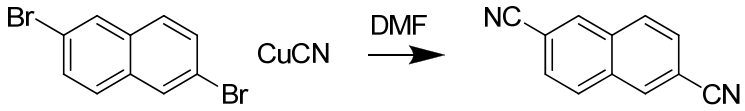

NaphthaCNTz 2,6-Dicyanonaphthalene (0.28g, 1.6mmol) and DCDA (0.14g, 1.7mmol) in Isopropanol (50cm3) were heated to 115°C. KOH (0.02g, 0.36mmol) was dissolved in Isopropanol (10cm3) and added dropwise to the reaction mixture which was then refluxed at 115°C for 22h. The solution was poured into cold water and the white ppte collected and washed with cold water until neutral. The product (0.36g, 85.6% yield) was dried in vacuo.

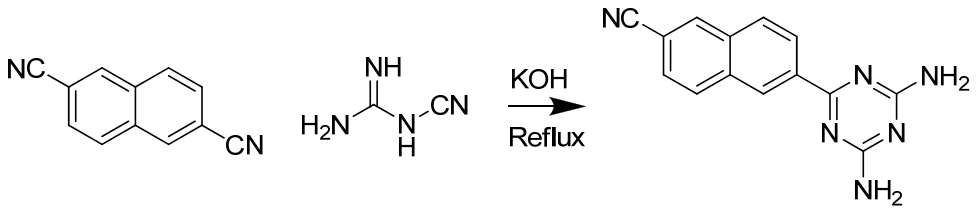

NaphthaCNTz2

Elemental Analysis C14.0H10.8N5.8O0.6 (Theory: C14.0H10.0N6.0O0.0)

IR 810.1cm-1 (Tz); 1398.3 - 1539.1 cm-1 (Ph); 2223.9 cm-1 (CN)

NMR

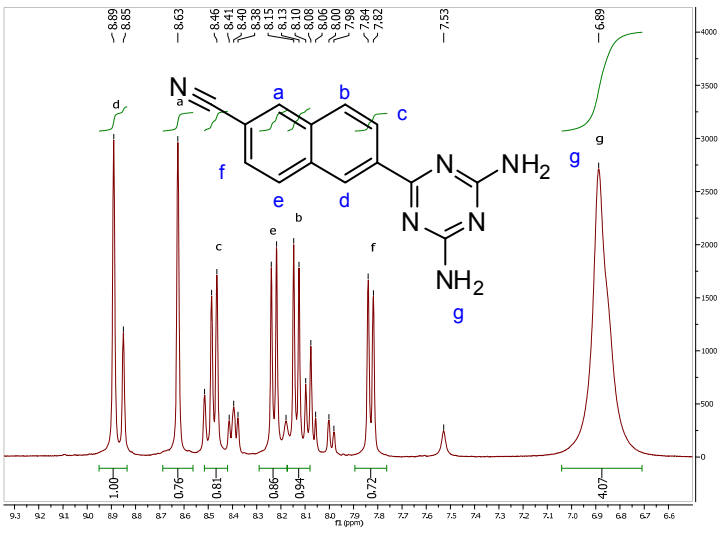

1H NMR (400 MHz, DMSO) δ = 8.89(s, Hd), 8.63(s, Ha), 8.49, 8.46(d, Hc), 8.24, 8.22(d, He), 8.18, 8.15, 8.13, 7.84, 7.82, 6.89

Note that the additional peaks at δ = 8.85, 8.52, 8.41, 8.40, 8.10, 8.08, 8.06, 8.00, 7.98, 8.38, 7.53 are due to the presence of the hydrolyzed product. A reference spectrum of a reaction carried out with a 1 : 1 molar ratio of monomer : KOH thus yielding ammelide product only, is shown below.

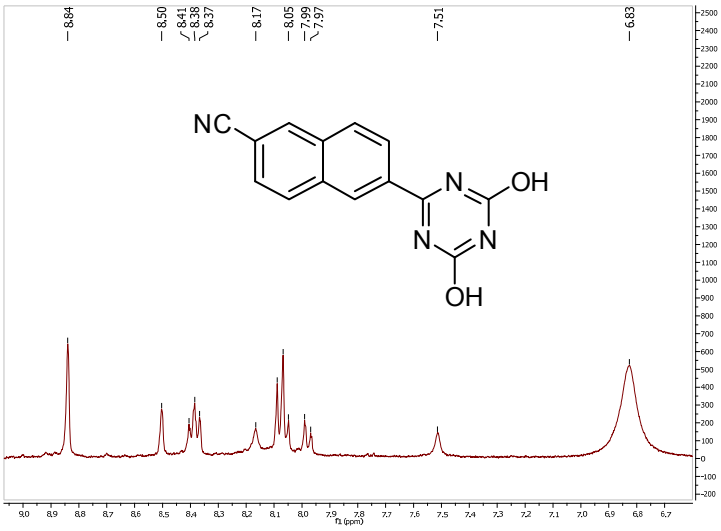

1H NMR (400 MHz, DMSO) δ = 8.84, 8.50, 8.41, 8.38, 8.37, 8.17, 8.09, 8.07, 8.05, 7.99, 7.97, 7.51, 6.83

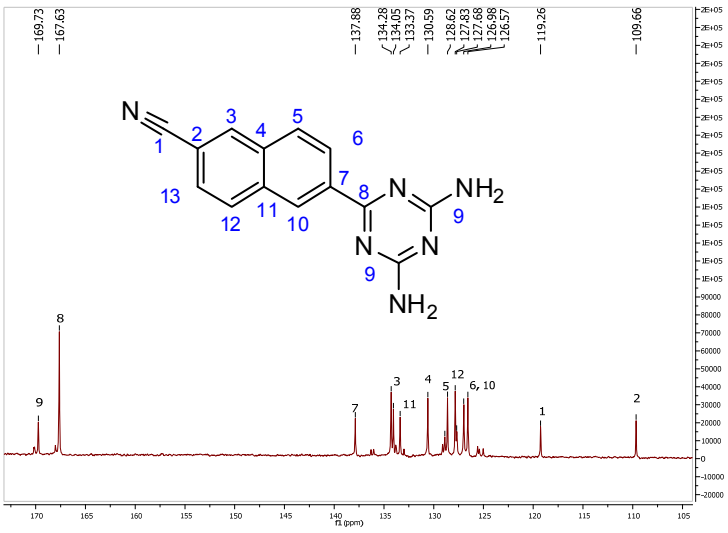

13C NMR (101 MHz, DMSO) δ = 169.73, 167.63, 137.88, 134.28, 134.05, 133.37, 130.59, 128.88, 128.62, 127.83, 127.68, 126.98, 126.57, 119.26, 109.66,

Again, the additional peaks in the spectrum are probably due to the presence of a small amount of ammelide-derived product. Hydrolysis occurs when all the 2,6-dicyano naphthalene has reacted with DCDA. If the mixture of NaphthaCNTz and ~17 mol % KOH is left to react further, hydrolysis will occur.

The reaction used in this project was left to reflux for 22h. Unfortunately not enough monomer was available to carry out further experiments and optimize reaction times.

8.6 Synthetic challenges

8.6.1 Bisubstition

It is important to use only one mole equivalent of DCDA to avoid bisubstitution, thus rendering the final product unsuitable for self-condensation.

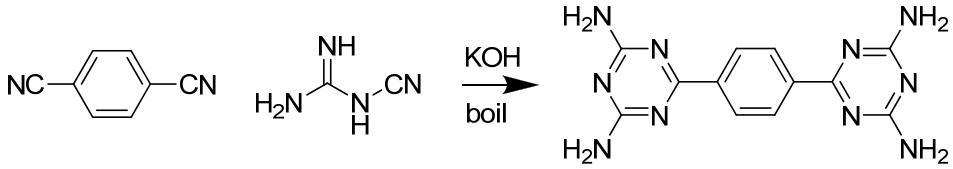

8.6.2 Hydrolysis of the nitrile group

Inert conditions (dry, N2 atmosphere) are required

Alkaline hydrolysis of the triazine functional group in product

On heating or long standing hydrolysis of the amino triazine to ammelide can occur[76]

The base must be used in catalytic amounts (~ 17 mol%) and added slowly to the reaction mixture

Reaction times must be optimized to avoid hydrolysis of the product once the reaction has completed

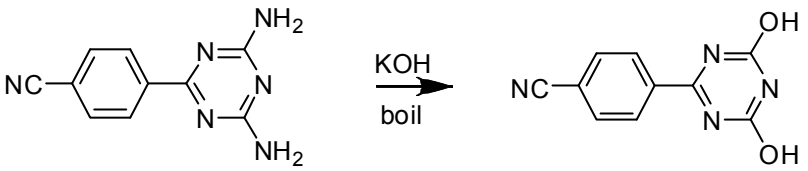

8.7 Atomic coordinates of HBF-1 in cif-fileformat

HBF-1				
	Space group name	C2		
	Int. tables number	5		
	Cell setting	monoclinic		
Unit cell parameters		**Symmetry equiv. pos.**		
a = 18.2480		x, y, z		
b = 31.6065		-x, y, -z		
c = 11.9394		x+1/2, y+1/2, z		
$\alpha = \beta = \gamma = 90.0$		-x+1/2, y+1/2, -z		
		fractional coordinates in terms of		
atom #	**element**	***a***	***b***	***c***
N1	N	-0.25000	-0.04997	0.21523
N2	N	-0.18750	-0.11247	0.21523
N3	N	-0.31250	-0.11247	0.21523
N4	N	-0.37500	-0.04997	0.21523
N5	N	0.18750	-0.48747	0.21523
N6	N	-1.12500	-0.04997	0.21523
C7	C	-0.25000	-0.17497	0.21523
C8	C	-0.18750	-0.23747	0.21523
C9	C	0.00000	-0.42497	0.21523
C10	C	0.06250	-0.48747	0.21523

C11	C	-0.31250	-0.23747	0.21523
C12	C	-0.25000	-0.29997	0.21523
C13	C	-0.18750	-0.36247	0.21523
C14	C	-0.12500	-0.42497	0.21523
C15	C	-0.06250	-0.48747	0.21523
C16	C	-0.31250	-0.36247	0.21523
C17	C	-0.25000	-0.42497	0.21523
C18	C	-0.37500	-0.42497	0.21523
C19	C	-0.50000	-0.42497	0.21523
C20	C	-0.43750	-0.48747	0.21523
C21	C	-0.56250	-0.48747	0.21523
N22	N	-0.68750	-0.48747	0.21523
C23	C	-0.31250	-0.07080	0.21523
C24	C	-0.25000	-0.13330	0.21523
C25	C	-0.18750	-0.19580	0.21523
C26	C	0.06250	-0.44580	0.21523
C27	C	0.12500	-0.50830	0.21523
C28	C	-0.31250	-0.19580	0.21523
C29	C	-0.25000	-0.25830	0.21523
N30	N	-0.18750	-0.32080	0.21523
N31	N	-0.12500	-0.38330	0.21523
C32	C	-0.06250	-0.44580	0.21523
C33	C	0.00000	-0.50830	0.21523
N34	N	-0.31250	-0.32080	0.21523
N35	N	-0.25000	-0.38330	0.21523
N36	N	-0.18750	-0.44580	0.21523
N37	N	-0.37500	-0.38330	0.21523
N38	N	-0.31250	-0.44580	0.21523
C39	C	-0.43750	-0.44580	0.21523
C40	C	-0.56250	-0.44580	0.21523
C41	C	-0.50000	-0.50830	0.21523
C42	C	-0.62500	-0.50830	0.21523
C43	C	-0.75000	-0.50830	0.21523
C44	C	-1.18750	-0.07080	0.21523
H45	H	-0.13340	-0.25550	0.21523
H46	H	0.00000	-0.38890	0.21523
H47	H	-0.36660	-0.25550	0.21523
H48	H	-0.11660	-0.50550	0.21523
H49	H	-0.50000	-0.38890	0.21523
H50	H	-0.38340	-0.50550	0.21523
H51	H	-0.13340	-0.17777	0.21523
H52	H	0.11660	-0.42777	0.21523
H53	H	-0.36660	-0.17777	0.21523
H54	H	0.00000	-0.54437	0.21523
H55	H	-0.61660	-0.42777	0.21523
H56	H	-0.50000	-0.54437	0.21523

N57	N	-0.56250	-0.40397	0.50000
N58	N	-0.37500	-0.46647	0.50000
N59	N	-0.43750	-0.52897	0.50000
C60	C	-0.56250	-0.27897	0.50000
C61	C	-0.75000	-0.09147	0.50000
C62	C	-0.31250	-0.52897	0.50000
C63	C	-0.56250	-0.15397	0.50000
C64	C	-0.62500	-0.09147	0.50000
C65	C	-0.18750	-0.52897	0.50000
C66	C	-0.43750	-0.44563	0.50000
C67	C	-0.56250	-0.32063	0.50000
C68	C	-0.81250	-0.07063	0.50000
C69	C	-0.37500	-0.50813	0.50000
N70	N	-0.56250	-0.19563	0.50000
N71	N	-0.62500	-0.13313	0.50000
C72	C	-0.68750	-0.07063	0.50000
C73	C	-0.25000	-0.50813	0.50000
N74	N	-0.56250	-0.07063	0.50000
H75	H	-0.61660	-0.26093	0.50000
H76	H	-0.75000	-0.12754	0.50000
H77	H	-0.13340	-0.51093	0.50000
H78	H	-0.61660	-0.33867	0.50000
H79	H	-0.86660	-0.08867	0.50000
H80	H	-0.25000	-0.47206	0.50000
N81	N	-0.50000	-0.46647	0.50000
C82	C	-0.50000	-0.34147	0.50000
C83	C	-0.50000	-0.21647	0.50000
C84	C	-0.50000	-0.09147	0.50000
C85	C	-0.50000	-0.38313	0.50000
C86	C	-0.50000	-0.25813	0.50000
N87	N	-0.50000	-0.13313	0.50000
C88	C	-0.50000	-0.50813	0.50000

8.8 Indexed and refined unit cell parameters of HBF-2

Table 2

HBF-2		
Hexagonal P6 (No. 5) $a = b = 27.410$ Å, $c = 11.835$ Å		
(*h k l*)	2θ / °	*d* / Å
(0 2 0), (0 0 1)	7.31	12.072

(0 1 1)	8.23	10.758
(0 4 0)	14.80	5.992
(1 1 2)	16.39	5.409
(1 2 2)	17.98	4.930
(2 2 2)	19.94	4.454
(3 3 1)	20.92	4.242
(1 5 1)	21.83	4.070
(0 0 3)	22.66	3.925
(0 3 3)	25.53	3.489
(0 7 0)	26.51	3.364
(3 4 2)	27.41	3.251
(2 5 2)	27.88	3.200
(0 5 3)	29.24	3.056
(5 6 0)	36.03	2.491
(0 10 0)	37.85	2.378
(6 6 0)	39.43	2.284
(0 11 0)	41.85	2.158
(5 8 0)	43.29	2.090

9 Acknowledgments

"Your PhD-defence is the very last moment in your academic career that someone will take genuine interest in your results."

- S. M. Clarke, Cambridge, UK

I considered it generally unfair that the people who were present at the beginning when the work started or accompanied the process as it developed should be named as the very last. However in the best tradition of *confirmatio*, also in this thesis the strongest point is coming last.

I would like to thank the following people whose manifold contributions to this work were valuable:

My doctoral advisor, **Prof. Dr. Markus Antonietti**, for the opportunity to earn a doctorate with the distinguished Max Planck Society, his advice and ideas, and a challenging and visionary research topic. Special thanks go to his multiple contributions to a general feeling of high spirits at the institute.

My supervisor, **Dr. Arne Thomas**, for the numerous discussions, useful suggestions, continuous support and excellent atmosphere in the group. Steadfast in the face of any challenge or challenger, I am certain he will be extraordinarily successful as professor at the TU Berlin.

Dr. Pierre Kuhn, **MSci (Cantab) Stephanie Wohlgemuth**, Mrs. **Regina Rothe** and Mrs. **Rona Pitschke** for their valuable contributions in form of discussions, synthetic expertise and measurements.

Dr. Jens-Oliver Müller is acknowledged for his cooperation in this work and his exhaustive fidelity.

Special thanks go to the Max Planck's own Thorstens, Jörg Menche and Silke Stöckle, for all the things in which drinking might play a decisive role. Further thanks go to all my jolly fellow scientists Dr. Magda, Dr. Vasana, Dr. Börner, Ide, Fix, Raffa, the French, Micro-Jens, Meso-Jens, Macro-Jens, Jo-Jo, den Wikinger, die Verrückte, all of the "Ana"s for greatly

contributing to my Berlin- and Golm-experience. Furthermore, I would like to thank all those who make the Max Planck Institute in Golm a great place to work in.

I extend my eternal thanks to my parents for their patience and their support.

Finally I would like to thank my partner, friend and love Elodie Soussan for being the treasure she is.

10 List of Publications

M. J. Bojdys, J.-O. Müller, M. Antonietti, A. Thomas, “Ionothermal Synthesis of Crystalline, Condensed, Graphitic Carbon Nitride”, *Chemistry – A European Journal*, **2008**, *14*, 8177-8182.

M. J. Bojdys, S. M. Clarke, L. D. Harper, C. Sun, M. A. Castro, S Medina, “Bulk and Adsorbed Monolayer Phase Behaviour of Binary Mixtures of Undecanoic Acid and Undecylamine: Catanionic Monolayers”, *Langmuir*, **2009**, *Revisions Received by Editorial Office*.

M. J. Bojdys, M. Antonietti, A. Thomas “Rational design of heptazine based frameworks”, *manuscript in preparation*.

M. J. Bojdys, M. Antonietti, A. Thomas “Carbon nitride intercalation compounds”, *manuscript in preparation*.

11 References

1. Marshall, P., *"The Philosopher's Stone: A Quest for the Secrets of Alchemy*. Macmillan: London, 2001.
2. Curl, R. F., PRE-1990 EVIDENCE FOR THE FULLERENE PROPOSAL. *Carbon* **1992,** 30, (8), 1149-1155.
3. Haufler, R. E.; Wang, L. S.; Chibante, L. P. F.; Jin, C. M.; Conceicao, J.; Chai, Y.; Smalley, R. E., FULLERENE TRIPLET-STATE PRODUCTION AND DECAY - R2PI PROBES OF C60 AND C70 IN A SUPERSONIC BEAM. *Chemical Physics Letters* **1991,** 179, (5-6), 449-454.
4. Kroto, H. W. In *FULLERENE CAGE CLUSTERS - THE KEY TO THE STRUCTURE OF SOLID CARBON*, Symp on Large Gas-Phase Clusters, Coventry, England, Dec 12-14, 1989; Royal Soc Chemistry: Coventry, England, 1989; pp 2465-2468.
5. Kratschmer, W.; Lamb, L. D.; Fostiropoulos, K.; Huffman, D. R., SOLID C-60 - A NEW FORM OF CARBON. *Nature* **1990,** 347, (6291), 354-358.
6. Liebig, J. v., Ueber einige Stickstoff-Verbindungen. *Annalen der Pharmacie* **1834,** 10.
7. Roesky, H. W.; Hofmann, H., *Chemiker Zeitung* **1984,** 108, 231.
8. Sung, C. M.; Sung, M., Carbon nitride and other speculative superhard materials. *Materials Chemistry and Physics* **1996,** 43, (1), 1-18.
9. Guo, Y. J.; Goddard, W. A., IS CARBON NITRIDE HARDER THAN DIAMOND - NO, BUT ITS GIRTH INCREASES WHEN STRETCHED (NEGATIVE POISSON RATIO). *Chemical Physics Letters* **1995,** 237, (1-2), 72-76.
10. Riedel, R.; Kroke, E.; Greiner, A.; Gabriel, A. O.; Ruwisch, L.; Nicolich, J., Inorganic solid-state chemistry with main group element carbodiimides. *Chemistry of Materials* **1998,** 10, (10), 2964-2979.
11. Kroll, P.; Hoffmann, R., Theoretical tracing of a novel route from molecular precursors through polymers to dense, hard C3N4 solids. *Journal of the American Chemical Society* **1999,** 121, (19), 4696-4703.
12. Kroke, E.; Schwarz, M., Novel group 14 nitrides. *Coordination Chemistry Reviews* **2004,** 248, (5-6), 493-532.
13. Kroke, E.; Schwarz, M.; Horath-Bordon, E.; Kroll, P.; Noll, B.; Norman, A. D., Tri-s-triazine derivatives. Part I. From trichloro-tri-s-triazine to graphitic C3N4 structures. *New Journal of Chemistry* **2002,** 26, (5), 508-512.
14. Anthony K. Cheetham, G. F. T. L., Open-Framework Inorganic Materials. *Angewandte Chemie International Edition* **1999,** 38, (22), 3268-3292.
15. Gmelin, L., Ueber einige Verbindungen des Melon's. *Annalen der Pharmacie* **1835,** 15, (3).
16. Franklin, E. C., The ammono carbonic acids. *Journal of the American Chemical Society* **1922,** 44, 486-509.
17. Cohen, M. L., Calculation of bulk moduli of diamond and zinc-blende solids. *Physical Review B (Condensed Matter)* **1985,** 32, (12), 7988-7991.
18. Teter, D. M., Computational alchemy: The search for new superhard materials. *Mrs Bulletin* **1998,** 23, (1), 22-27.
19. Malkow, T., Critical observations in the research of carbon nitride (vol 292, pg 112, 2000). *Materials Science and Engineering a-Structural Materials Properties Microstructure and Processing* **2001,** 302, (2), 309-+.
20. Matsumoto, S.; Xie, E. Q.; Izumi, F., On the validity of the formation of crystalline carbon nitrides, C3N4. *Diamond and Related Materials* **1999,** 8, (7), 1175-1182.
21. Fang, P. H., ON THE BETA-C3N4 SEARCH. *Journal of Materials Science Letters* **1995,** 14, (8), 536-538.
22. DeVries, R. C., Inventory on innovative research: the case of C3N4. *Materials Research Innovations* **1997,** 1, (3), 161-162.
23. Malkow, T., Critical observations in the research of carbon nitride. *Materials Science and Engineering a-Structural Materials Properties Microstructure and Processing* **2000,** 292, (1), 112-124.
24. Kawaguchi, M.; Nozaki, K., SYNTHESIS, STRUCTURE, AND CHARACTERISTICS OF THE NEW HOST MATERIAL [(C3N3)(2)(NH)(3)](N). *Chemistry of Materials* **1995,** 7, (2), 257-264.
25. McMurran, J.; Kouvetakis, J.; Nesting, D. C., Synthesis of molecular precursors to carbon-nitrogen-phosphorus polymeric systems. *Chemistry of Materials* **1998,** 10, (2), 590-593.
26. Montigaud, H.; Tanguy, B.; Demazeau, G.; Courjault, S.; Birot, M.; Dunogues, J., Graphitic form of C3N4 through the solvothermal route. *Comptes Rendus De L Academie Des Sciences Serie Ii Fascicule B-Mecanique Physique Chimie Astronomie* **1997,** 325, (4), 229-234.
27. Komatsu, T., Attempted chemical synthesis of graphite-like carbon nitride. *Journal of Materials Chemistry* **2001,** 11, (3), 799-801.

28. Komatsu, T., The first synthesis and characterization of cyameluric high polymers. *Macromolecular Chemistry and Physics* **2001,** 202, (1), 19-25.
29. Shtrempler, G. I.; Murzubraimov, B.; Rysmendeev, K., THERMAL-STABILITY OF COMPLEX-COMPOUNDS BASED ON THIOSEMICARBAZIDE. *Zhurnal Neorganicheskoi Khimii* **1982,** 27, (3), 789-792.
30. Pauling, L.; Sturdivant, J. H., The structure of cyameluric acid, hydromelonic a cid, and related substances. *Proceedings of the National Academy of Sciences of the United States of America* **1937,** 23, 615-620.
31. Gillan, E. G., Synthesis of nitrogen-rich carbon nitride networks from an energetic molecular azide precursor. *Chemistry of Materials* **2000,** 12, (12), 3906-3912.
32. Kroke, E.; Schwarz, M.; Buschmann, V.; Miehe, G.; Fuess, H.; Riedel, R., Nanotubes formed by detonation of C/N precursors. *Advanced Materials* **1999,** 11, (2), 158-161.
33. Horvath-Bordon, E.; Riedel, R.; McMillan, P. F.; Kroll, P.; Miehe, G.; van Aken, P. A.; Zerr, A.; Hoppe, P.; Shebanova, O.; McLaren, I.; Lauterbach, S.; Kroke, E.; Boehler, R., High-pressure synthesis of crystalline carbon nitride imide, C2N2(NH). *Angewandte Chemie-International Edition* **2007,** 46, (9), 1476-1480.
34. Horvath-Bordon, E.; Kroke, E.; Svoboda, I.; Fuess, H.; Riedel, R., Tri-s-triazine derivatives, part III. Potassium melonate, K-3[C6N7(NCN)(3)]center dot 5H(2)O, and its potential use for the synthesis of graphite-like C3N4 materials. *New Journal of Chemistry* **2005,** 29, (5), 693-699.
35. Bundy, F. P.; Hall, H. T.; Strong, H. M.; Wentorf, R. H., MAN-MADE DIAMONDS. *Nature* **1955,** 176, (4471), 51-55.
36. Goettmann, F.; Fischer, A.; Antonietti, M.; Thomas, A., Chemical synthesis of mesoporous carbon nitrides using hard templates and their use as a metal-free catalyst for friedel-crafts reaction of benzene. *Angewandte Chemie-International Edition* **2006,** 45, (27), 4467-4471.
37. Goettmann, F.; Fischer, A.; Antonietti, M.; Thomas, A., Metal-free catalysis of sustainable Friedel-Crafts reactions: direct activation of benzene by carbon nitrides to avoid the use of metal chlorides and halogenated compounds. *Chemical Communications* **2006**, (43), 4530-4532.
38. Goettmann, F.; Thomas, A.; Antonietti, M., Metal-free activation CO2 by mesoporous graphitic carbon nitride. *Angewandte Chemie-International Edition* **2007,** 46, (15), 2717-2720.
39. Bai, X. D.; Zhong, D. Y.; Zhang, G. Y.; Ma, X. C.; Liu, S.; Wang, E. G.; Chen, Y.; Shaw, D. T., Hydrogen storage in carbon nitride nanobells. *Applied Physics Letters* **2001,** 79, (10), 1552-1554.
40. Wang, X.; Maeda, K.; Thomas, A.; Takanabe, K.; Xin, G.; Carlsson, J. M.; Domen, K.; Antonietti, M., A metal-free polymeric photocatalyst for hydrogen production from water under visible light. *Nat Mater* **2008,** advanced online publication.
41. Jurgens, B.; Irran, E.; Schneider, J.; Schnick, W., Trimerization of NaC2N3 to Na3C6N9 in the solid: Ab initio crystal structure determination of two polymorphs of NaC2N3 and of Na3C6N9 from X-ray powder diffractometry. *Inorganic Chemistry* **2000,** 39, (4), 665-670.
42. Lotsch, B. V.; Doblinger, M.; Sehnert, J.; Seyfarth, L.; Senker, J.; Oeckler, O.; Schnick, W., Unmasking melon by a complementary approach employing electron diffraction, solid-state NMR spectroscopy, and theoretical calculations-structural characterization of a carbon nitride polymer. *Chemistry-a European Journal* **2007,** 13, (17), 4969-4980.
43. Kanatzidis, M. G.; Park, Y., MOLTEN-SALT SYNTHESIS OF LOW-DIMENSIONAL TERNARY CHALCOGENIDES - NOVEL STRUCTURE TYPES IN THE K/HG/S, K/HG/SE SYSTEM. *Chemistry of Materials* **1990,** 2, (2), 99-101.
44. Solomons, C.; Goodkin, J.; Gardner, H. J.; Janz, G. J., HEAT OF FUSION, ENTROPY OF FUSION AND CRYOSCOPIC CONSTANT OF THE LICL-KCL EUTECTIC MIXTURE. *Journal of Physical Chemistry* **1958,** 62, (2), 248-250.
45. Laitinen, H. A.; Tischer, R. P.; Roe, D. K., EXCHANGE CURRENT MEASUREMENTS IN KCL-LICL EUTECTIC MELT. *Journal of the Electrochemical Society* **1960,** 107, (6), 546-555.
46. Cassayre, L.; Serp, J.; Soucek, P.; Malmbeck, R.; Rebizant, J.; Glatz, J. P., Electrochemistry of thorium in LiCl-KCl eutectic melts. *Electrochimica Acta* **2007,** 52, (26), 7432-7437.
47. Sundermeyer, W., Salzschmelzen und ihre Verwendung als Reaktionsmedien. *Angewandte Chemie* **1965,** 77, (6), 241-258.
48. Sundermeyer, W., Chemische Reaktionen in geschmolzenen Salzen. *Chemie in unserer Zeit* **1967,** 1, (5), 150-157.
49. Verbeek, W.; Sundermeyer, W., Darstellung von Carbonyl- und Fluorcarbonyl-pseudohalogeniden in der Salzschmelze. *Angewandte Chemie* **1967,** 79, (19), 860-861.
50. Sundermeyer, W., Hexamethyldisilan. *Zeitschrift für anorganische und allgemeine Chemie* **1961,** 310, (1-2), 50-52.

51. Lotsch, B. V.; Schnick, W., New light on an old story: Formation of melam during thermal condensation of melamine. *Chemistry-a European Journal* **2007,** 13, (17), 4956-4968.
52. Hosmane, R. S.; Rossman, M. A.; Leonard, N. J., SYNTHESIS AND STRUCTURE OF TRI-S-TRIAZINE. *Journal of the American Chemical Society* **1982,** 104, (20), 5497-5499.
53. May, H., Pyrolysis of melamine. *Journal of Applied Chemistry* **1959,** 9, (6), 340-344.
54. Ruland, W.; Smarsly, B., X-ray scattering of non-graphitic carbon: an improved method of evaluation. *Journal of Applied Crystallography* **2002,** 35, 624-633.
55. Sehnert, J.; Baerwinkel, K.; Senker, J., Ab initio calculation of solid-state NMR spectra for different triazine and heptazine based structure proposals of g-C3N4. *Journal of Physical Chemistry B* **2007,** 111, (36), 10671-10680.
56. George J., J., *Molten Salts Handbook*. Academic Press: London, 1967.
57. Kuhn, P.; Forget, A.; Su, D. S.; Thomas, A.; Antonietti, M., From Microporous Regular Frameworks to Mesoporous Materials with Ultrahigh surface Area: Dynamic Reorganization of Porous Polymer Networks. *Journal of the American Chemical Society* **2008,** 130, (40), 13331-13337.
58. Thomas, A.; Fischer, A.; Goettmann, F.; Antonietti, M.; Muller, J. O.; Schlogl, R.; Carlsson, J. M., Graphitic carbon nitride materials: variation of structure and morphology and their use as metal-free catalysts. *Journal of Materials Chemistry* **2008,** 18, (41), 4893-4908.
59. Bacon, G. E., A NOTE ON THE RHOMBOHEDRAL MODIFICATION OF GRAPHITE. *Acta Crystallographica* **1950,** 3, (4), 320-320.
60. Jagodzinski, H., EINDIMENSIONALE FEHLORDNUNG IN KRISTALLEN UND IHR EINFLUSS AUF DIE RONTGENINTERFERENZEN .1. BERECHNUNG DES FEHLORDNUNGSGRADES AUS DEN RONTGENINTENSITATEN. *Acta Crystallographica* **1949,** 2, (4), 201-207.
61. Fredenhagen, K.; Cadenbach, G., The formation of kalium through carbon. *Zeitschrift für anorganische und allgemeine Chemie* **1926,** 158, (3/4), 249-265.
62. Delhaes, P.; Rouillon, J. C.; Manceau, J. P.; Guerard, D.; Herold, A., PARAMAGNETISM AND SPECIFIC-HEAT OF GRAPHITE LAMELLAR COMPOUND C-6LI. *Journal De Physique Lettres* **1976,** 37, (5), L127-L129.
63. Rudorff, W.; Schulze, E., UBER ALKALIGRAPHITVERBINDUNGEN. *Zeitschrift für anorganische und allgemeine Chemie* **1954,** 277, (3-4), 156-171.
64. Heald, S. M.; Stern, E. A., EXTENDED-X-RAY-ABSORPTION-FINE-STRUCTURE STUDY OF BR2-GRAPHITE SYSTEM. *Physical Review B* **1978,** 17, (10), 4069-4081.
65. Ubbelohde, A. R., NEW INTEREST IN CARBON LAMELLAR COMPOUNDS. *Nature* **1977,** 268, (5615), 16-17.
66. Ebert, L. B., *Annual Review of Materials Science* **1976,** 6, 182.
67. Novikov, Y. N.; Volpin, M. E., Lamellar Compounds of Graphite with Alkali Metals. *Russian Chemical Reviews* **1971,** 40, (9), 733-746.
68. Amelinckx, S.; Bernaerts, D.; Zhang, X. B.; Van Tendeloo, G.; Van Landuyt, J., A Structure Model and Growth Mechanism for Multishell Carbon Nanotubes. *Science* **1995,** 267, (5202), 1334-1338.
69. Zhou, O.; Fleming, R. M.; Murphy, D. W.; Chen, C. H.; Haddon, R. C.; Ramirez, A. P.; Glarum, S. H., Defects in Carbon Nanostructures. *Science* **1994,** 263, (5154), 1744-1747.
70. Viculis, L. M.; Mack, J. J.; Kaner, R. B., A Chemical Route to Carbon Nanoscrolls. *Science* **2003,** 299, (5611), 1361-.
71. Viculis, L. M.; Mack, J. J.; Kaner, R. B., A chemical route to carbon nanoscrolls. *Science* **2003,** 299, (5611), 1361-1361.
72. Bojdys, M. J.; Muller, J. O.; Antonietti, M.; Thomas, A., Ionothermal Synthesis of Crystalline, Condensed, Graphitic Carbon Nitride. *Chemistry-a European Journal* **2008,** 14, (27), 8177-8182.
73. Cote, A. P.; Benin, A. I.; Ockwig, N. W.; O'Keeffe, M.; Matzger, A. J.; Yaghi, O. M., Porous, crystalline, covalent organic frameworks. *Science* **2005,** 310, (5751), 1166-1170.
74. El-Kaderi, H. M.; Hunt, J. R.; Mendoza-Cortes, J. L.; Cote, A. P.; Taylor, R. E.; O'Keeffe, M.; Yaghi, O. M., Designed synthesis of 3D covalent organic frameworks. *Science* **2007,** 316, (5822), 268-272.
75. Rouquerol, F.; Rouquerol, J.; Sing, K., *Adsorption by Powders and Porous Solids*. Academic Press: London, 2002.
76. Smolin, E. M.; Rapoport, L., *s-Triazines and Derivatives*. Interscience Publishers LTD.: London, 1959.